Molecular line emission in asymmetric envelopes of evolved stars

Dissertation
zur
Erlangung des Doktorgrades (Dr. rer. nat.)
der
Mathematisch-Naturwissenschaftlichen Fakultät
der
Rheinischen Friedrich-Wilhelms-Universität Bonn

von
Andrés Felipe Pérez Sánchez
aus
Medellín, Colombia.

Bonn, 2014

Dieser Forschungsbericht wurde als Dissertation von der Mathematisch-Naturwissenschaftlichen Fakultät der Universität Bonn angenommen und ist auf dem Hochschulschriftenserver der ULB Bonn `http://hss.ulb.uni-bonn.de/diss_online` elektronisch publiziert.

1. Gutachter:	Prof. Dr. Wouter Vlemmings
2. Gutachter:	Prof. Dr. Frank Bertoldi

Tag der Promotion:	23.06.2014
Erscheinungsjahr:	2014

Abstract

Stars with initial masses of $0.8 < M_\star < 9\mathrm{M}_\odot$ eject most of their mass when evolving along the asymptotic giant branch (AGB) phase. The ejected material eventually cools down, which leads it to condensate and to form dust grains and molecular gas around the star, creating an extended circumstellar envelope (CSE). The mechanism responsible for the expansion of the dusty and dense CSEs is not completely understood. It is suggested that stellar radiation pressure on the dust particles can accelerate them outwards. Then, by collisional exchange of momentum, the dust particles drag along the molecular gas. However, this scenario cannot explain the onset of asymmetries in the CSEs observed towards more evolved sources such as post-AGB sources and Planetary nebulae.

Part of the research in this thesis is focused on the study of the role that the stellar magnetic field plays on the formation of the collimated high-velocity outflows observed towards post-AGB sources. Polarized maser emission towards (post-)AGB stars has become an useful tool to determine the properties of the stellar magnetic fields permeating their CSEs. However, the polarization fraction detected can be affected by non-Zeeman effects. Here I present the results of our analysis of the polarization properties of SiO, H_2O and HCN maser emission in the (sub-)millimetre wavelength range. The goal of this analysis is to determine whether polarized maser emission of these molecular species can be used as reliable tracer of the magnetic field from observations at (sub-)millimetre wavelengths.

I also present the results of radio interferometric observations of both continuum and polarized maser emission towards post-AGB stars. The sources observed are characterized by H_2O maser emission arising from their collimated, high-velocity outflows. The observations have been carried out with the Australian Telescope Compact Array aiming to detect both polarized maser emission and non-thermal radio continuum emission.

Part of the research on this thesis is dedicated to radiative transfer modelling of CO emission towards asymmetric AGB sources. Radio observations of CO emission are commonly used to probe the mass-loss rates and the kinematics of the CSEs. However, in most cases the observed sources are assumed spherically symmetric. Here I present the results of simulated observations towards oblate CSEs. The aim of this study is to identify the effects induced by the asymmetries on the observed spectral features, and consequently, on the physical parameters of the CSEs derived assuming the sources spherically symmetric.

Contents

1 Introduction **1**
1.1 Post-Main sequence evolution . . . 3
1.2 Stellar evolution along the Asymptotic giant branch . . . 5
1.2.1 The circumstellar envelope . . . 7
1.2.2 Circumstellar maser emission: Overview . . . 10
1.3 Beyond the AGB: Post-AGB Stars . . . 12
1.3.1 Water fountains . . . 15
1.4 Radiative transfer . . . 16
1.5 Aims of this thesis . . . 18

2 Maser emission **21**
2.1 Polarization: Overview . . . 25
2.1.1 Stokes parameters . . . 26

3 Radio observations of circumstellar envelopes of AGB stars **29**
3.1 Observing the molecular gas towards CSEs . . . 29
3.2 Radio interferometry: Overview . . . 33

4 Maser Polarization **39**
4.1 Maser polarization theory . . . 41
4.2 Maser emission in the ALMA frequency range . . . 42
4.2.1 SiO . . . 42
4.2.2 H_2O . . . 43
4.2.3 HCN . . . 43
4.3 Model results . . . 44
4.4 Analysis . . . 48
4.4.1 SiO maser . . . 48
4.4.2 H_2O maser . . . 51
4.4.3 HCN maser . . . 51

4.5 Observing maser polarization with ALMA 52
4.6 Conclusions 54

5 Water maser polarization of the water fountains IRAS 15445−5449 and IRAS 18043−2116 57
5.1 Observation and data reduction 58
5.2 Results 61
5.3 Discussion 62
5.3.1 d46 (*IRAS 15445−5449, OH326.530−00.419*) 62
5.3.2 b292 (*IRAS 18043−2116, OH009.1−0.4*) 64
5.4 Conclusions 65

6 First resolved image of a synchrotron jet towards a post-AGB star. 69
6.1 Observations and results 71
6.1.1 Recent and archive observations 71
6.1.2 Maps and spectral energy distribution 72
6.2 Analysis 72
6.2.1 Model 72
6.2.2 Fermi acceleration and magnetic field 73
6.2.3 Variability and lifetime 74
6.2.4 Implications for post-AGB outflows 76
6.3 Discussion 76

7 CO line emission from asymmetrical AGB sources 81
7.1 The model 82
7.2 Results 86
7.2.1 Line profiles 86
7.3 Analysis 96
7.4 Conclusions 101

8 Summary 103
8.1 Outlook 104

Bibliography 107

List of Figures 117

List of Tables 119

Acknowledgements 121

CHAPTER 1

Introduction

Stars are spread through the Hertzsprung-Russell (HR) diagram (Fig. 1.1) according to their mass, luminosity and surface temperature. Their position on the HR diagram is also an indicative of their evolutionary status, where each phase is the base for the different research areas that stellar astrophysics comprises. One of those phases is known as the Asymptotic giant branch (AGB) phase, where low- and intermediate-mass stars begin the end of their evolution.

Back in 1966, Sandage and Walker for the first time used the term *asymptotic* to refer to those stars observed towards the globular cluster M92, whose position in both the two-color ($U - B, B - V$) and the color-magnitude diagram (particular cases of the HR diagram) is slightly shifted from the position of the red giant and subgiant stars (Fig. 1.1). According to Sandage and Walker (1966): "*Differences in chemical composition along a given branch seems unreasonable in light of our present knowledge, and we have no explanation for the effect at this time. Nevertheless, it is interesting to speculate that, if branch B stars are normal and if only a simple discontinuity had existed between branches B and C, each satisfying the gravity line, this result might have arisen from an enrichment in the metal content of the group C stars. This enrichment might be brought about if these objects represent stars which have passed through the extreme red-giant phase (…)*". Nowadays we know that such enrichment is one of the consequences of the thermal instabilities that the interior of the star undergoes throughout its evolution beyond the Main Sequence (MS) phase.

In the next sections I give a general description of the evolution of stars from the MS to the AGB, which is based on Habing and Olofsson (2003). I also give an overview of the main subject of the observational studies aimed to unveil the late stages of stellar evolution of low- and intermediate-mass stars: The dusty, cold, and dense circumstellar envelopes (CSEs) of AGB and post-AGB stars. References different to Habing and Olofsson (2003) will be mentioned explicitly throughout the text.

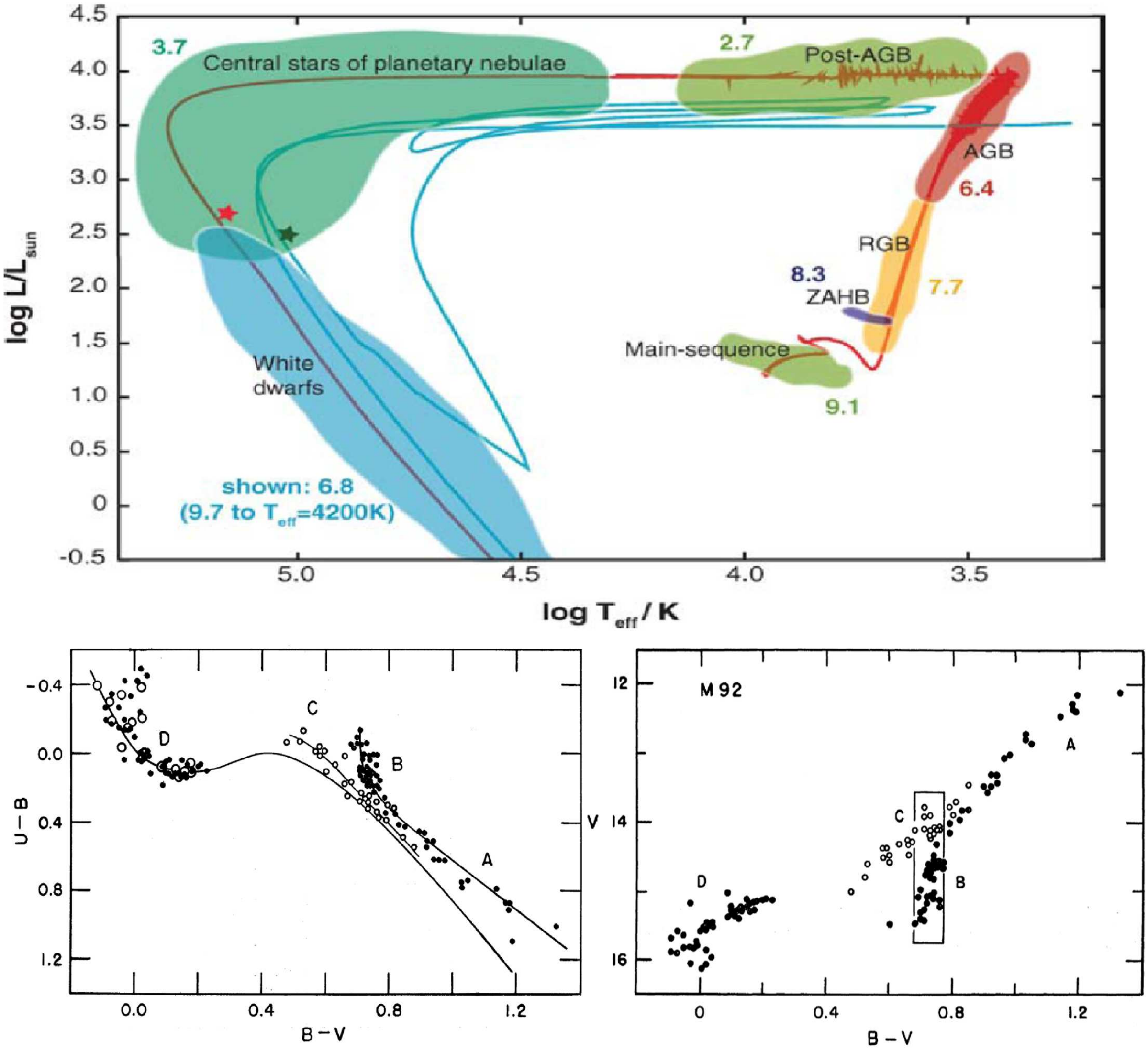

Figure 1.1: *Top* Schematic view of the Hertzsprung-Russell diagram and the computed evolution track from the main sequence to the white dwarfs phase for a 2 $M_{\odot}$ star with solar metallicity. Numbers next to the track are the log of the time spend by a 2 $M_{\odot}$ star duration of each evolutionary phase. Adopted from Herwig (2005). *Bottom* Color-color (left) and color-magnitude diagram of the globular cluster M92 observed by Sandage and Walker. Adopted from Sandage and Walker (1966).

1.1 Post-Main sequence evolution

The evolution of stars depends on their mass during the MS phase. Low- and intermediate-mass stars are those whose main-sequence-mass is between 0.8 and 8-9 times the solar mass (hereafter $M_{\odot}$). After spending most of their life burning Hydrogen (H) at the stellar core, low- and intermediate-initial-mass stars leave the MS once the nucleosynthesis of H starts taking place in a thick shell formed around the inert Helium (He) core. Because the temperature of the stellar core is not high enough to start the nucleosynthesis of the He, the energy that guarantees both the hydrostatic and thermal equilibrium of the stellar envelope is supplied by the H-burning shell, where the main nuclear processes are the proton−proton (p−p) chain, which supplies most of the energy, and the Carbon-Nitrogen-Oxygen (CNO) cycle (figure 1.2). The stellar core gradually contracts whereas the stellar atmosphere expands and becomes convective. The gravitational energy released due to the contraction of the core, together with the energy produced at the H-burning shell, lead to a global expansion of the stellar envelope. The increase of both the stellar radius and the energy flux of the emerging radiation field are observed as an increase of the luminosity of the star. This places the star along the Red Giant Branch (RGB) at the HR diagram. Because the readjustment of the internal structure of the star, the base of the convective envelope can penetrate deep into the region where the nucleosynthesis of H takes place. Hence, products from the nucleosynthesis of H at the center of the star such as ^{4}He, ^{14}N and ^{13}C, are brought to the outer layers of the stellar envelope by the convection. Such enrichment of the stellar envelope is due to the so called first dredge-up, which takes place in the stellar envelope of those stars which pass through the RGB. During the RGB phase, the structure of the stellar core of stars with $M_{\star} < 2.0$ $M_{\odot}$ is sustained due to the increasing degeneracy pressure.

The increase of the temperature in the core leads to a thermal runaway, the so called helium core flash. It removes the degeneracy of the He-core and ignites the He nucleosynthesis via the triple-α reaction (figure 1.2). In higher-mass stars ($2.0 < M_{\star} \leq 9$ $M_{\odot}$), the beginning of the He-burning phase in the stellar core occurs in a non-degenerate scenario, once its temperature is high enough (of the order of 10^{8} K) to ignite the nuclear fusion of He. Once the He-burning phase starts, the interior of the star suffers a new adjustment. The stellar core expands, while its envelope contracts. This, combined with nucleosynthesis processes at the H-burning shell, lead to an increase of the temperature in the stellar envelope. The subsequent diminution of its radius is observed as a decrease of the stellar luminosity. In the HR diagram, the star is now placed at the Horizontal Branch (HB), and depending on its metallicity, it will be observed either in the red clump (those with solar metallicity) or towards the blue region of the horizontal branch (those with low metallicity). At this point, the star begins a relative long evolution phase, where the energy produced in both the He-core and the H-burning shell keep the hydrostatic equilibrium of the stellar envelope.

The mass fraction of Carbon (C) and Oxygen (O) increase due to the nucleosynthesis of He at the stellar core, where the electron degeneracy starts playing an important role in the stability of its structure.

Once the He is exhausted in the stellar core, the star undergoes a new readjustment of its internal struc-

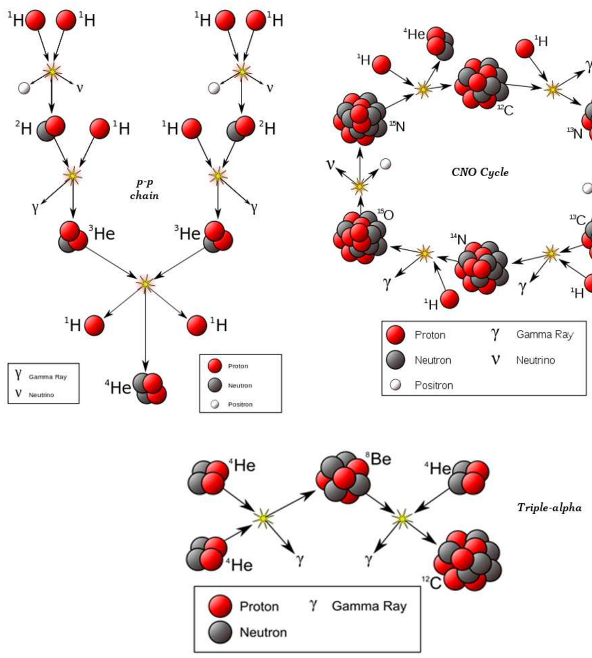

Figure 1.2: Schematic overview of the three main nuclear burning processes dominating the energy production at the core of low- and intermediate-initial-mass stars: (*top left*) p-p chain (*top right*) CNO cycle (*bottom*) Triple alpha reaction. (Adopted from http//:en.wikipedia.org/wiki/).

ture. The inert C−O core begins to contract again, releasing gravitational energy that contributes to the energy flux of the emerging radiation field, whereas the stellar envelope expands. These effects combined lead to the increase of the stellar luminosity. The further contraction of the stellar core results in the formation of a He-burning shell between the C−O core and the H-burning shell. The high degeneracy pressure of the stellar core prevents it from the collapse. But in addition, its high degeneracy leads to neutrino emission that drains energy from the stellar core. Hence, the stellar core of low- and intermediate-mass stars will not reach the necessary temperature for any further nuclear fusion of C or O. In the case of stars with $M_\star \sim 1\ \mathrm{M}_\odot$, the energy output that ensure the equilibrium of the stellar envelope is provided by the two burning shells. For more massive stars ($M_\star \sim 5\ \mathrm{M}_\odot$), the ignition of the He-burning shell results in a strong expansion of the region above the inactive C−O core. Such expansion drives the H-burning shell towards regions where the temperature and density are lower and then extinguishes. Depending on the composition, stars with $M_\star > 4\ \mathrm{M}_\odot$ undergo a second dredge-up. For those stars, the convective envelope is able to penetrate deep into the inactive H-burning shell, taking material already processed such as ^{4}He, ^{14}N and ^{13}C up to the outer layers of the stellar atmosphere. This can be observed, for instance, with the increase of the abundance of ^{14}N, and the lowering of the ratio ^{12}C/^{13}C at the stellar surface.

After the second dredge-up, the H-burning shell is reignited, and the star begins its evolution along the Asymptotic giant branch.

1.2 Stellar evolution along the Asymptotic giant branch

Regardless its mass, the internal structure of stars at the beginning of the AGB phase is similar. The degenerate C−O core is surrounded by the He-burning shell, which is situated between the stellar core and the more external H-burning shell. On top of the H-shell is the very extended stellar envelope.
During the early AGB phase, the major contribution to the total luminosity of the star comes from the He-burning shell, i.e. assuming that $L_\star \approx L_{He} + L_H$, then $L_{He} > L_H$.
The energy is produced via the triple−α reaction in the He-shell, which is a nuclear energy source very sensitive to the temperature. The balance between the energy production rate and the energy loss due to flux divergences is determined by the thickness of the He-burning shell. Because the thickness of the shell decreases as the He is burnt, the energy production rate eventually overcomes the energy loss from the shell, which is basically an increase of temperature in the He-shell. This leads to a thermal runaway, the so called helium shell flash. Depending on the core mass, the He-shell flash luminosity can reach values of the order of $L_{He} = 10^8$ L$_\odot$. After the He-shell developes the first shell flash, the star becomes a thermally pulsing (TP-)AGB star.
During one thermal pulse, the excess of energy produced by the He-shell flash results in an expansion of the zone surrounding the He-shell that push outwards the layers above it. Thus, the H-burning shell is again driven towards regions where it nearly extinguishes. Since the large amount of energy produced by the He-shell flash cannot be transported by radiation alone, the intershell zone becomes highly convective. The intershell convective zone (ISCZ) extends from the interphase between the He-shell and the C−O core up to the dormant H-shell, and contains the products of the nucleosynthesis in both burning shells. The most abundant elements in the ISCZ are ^{4}He (70-75%) and ^{12}CO (20-25%). It also contains small percentage of ^{16}O and ^{14}N. Further nuclear reactions involving α particles within the ISCZ result in the increase of the abundance of ^{22}Ne and ^{13}C which, after further nuclear reactions with α particles, produce a small density of neutrons that eventually increase the abundance of neutron-rich isotopes in the ISCZ via the so called s-process. Once the high energy production start to decline at the He-shell, the ISCZ contracts. This leads to reignition of the H-burning shell. During this new readjustment, the bottom of the convective stellar atmosphere penetrates deep into the former intershell zone. How deep the convective envelope reaches depend on the core mass and on the strength of the ongoing thermal pulse. Hence, the surface abundance of ^{12}C and neutron-rich isotopes such as Ba and Zr is changed. This is referred as the third dredge-up.

Due to the third dredge-up, the number of thermal pulses that an AGB developes has a strong impact on the surface abundance of the star, and in particular, on the surface abundance ratio C/O. At the beginning of the AGB phase the surface abundance of C and O is such that C/O$\sim$ 0.3, but due to the dredge-up of ^{12}C after each thermal pulse, the abundance of carbon in the stellar envelope could balance the surface abundance of oxygen C/O$\approx$ 1, or even surpass it, which results in C/O$>$ 1. Although the third dredge-up is necessary to increase the surface abundance of C, if the temperature at the bottom of the stellar envelope is high enough to trigger the CNO cycle, then the ^{12}C dredged from the center of the

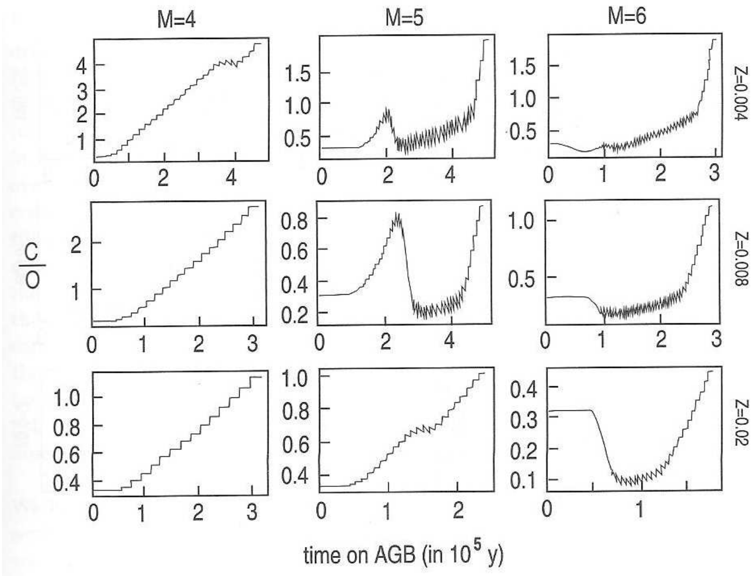

Figure 1.3: Evolution of the C/O ratio for nine stellar models during the AGB phase. The columns give three different modelled masses (4, 5 and 6 $M_\odot$) for each metallicity (rows). Adopted from Habing and Olofsson (2003).

star could be burned before being mix in the outer layers of the stellar envelope. The efficiency of the nucleosynthesis at the bottom of the envelope, the Hot bottom burning (HBB), eventually determines the elements abundance in the stellar atmosphere. The efficiency of the HBB depends on both the mass and the metallicity of the star. The HBB is more efficient for higher mass AGB stars with solar metallicity, while for low metallicity stars, the third dredge up is efficient enough to invert the value of the C/O ratio at the stellar surface (Fig. 1.3). According to the surface C/O ratio, the stars evolving along the AGB are classified as either M-type (O-rich, C/O$<$ 1), C-type (C-rich, C/O$>$ 1) or S-type (C/O$\approx$ 1) AGB stars.

Once the contribution of the H-shell to the total luminosity, L_H, surpass L_{He}, the star begins the so called interpulses phase. This phase is characterized by a temporary stability of the innermost layers of the star, as well as by its constant luminosity, which is a result of the steady energy production rate in the H-burning shell. Depending on the stellar mass, the interpulses phase can be of the order of 10^4 yr for the more massive stars ($M_\star$ = 5 $M_\odot$), and 10^5 yr for stars with $M_\star$ = 1 $M_\odot$ (Wagenhuber and Groenewegen 1998). At the end of the interpulses, the conditions for a new thermal instability in the He-shell are set again. As the star evolves along the AGB phase, the time scale between two consecutive pulses decreases, whereas the strength of the thermal pulses increases.

The luminosity variations induced by the thermal pulses imply variations of the stellar radius. Moreover, the large amount of energy released by the thermal instabilities at the center of the star produces shock waves that propagate outwards following the density gradient of the stellar atmosphere. As the outer layers of the stellar atmosphere expands, the density drops, and the shock waves eventually reach supersonic speed, leading to pressure-driven ejection of atomic gas from the outermost layers of the

stellar atmosphere. If this material reach regions where the temperature and the density conditions are such that it condensates and forms solid grains, then its interaction with the emerging radiation field can generate a radiation-driven wind. Otherwise, the ejected material eventually falls back onto the stellar atmosphere. This is the most accepted scenario describing the mass-loss process, however, the details of the mass-loss mechanism, which involves for instance its dependence on time, stellar mass and metallicity, are yet rather unknown.
The mass-loss rate together with the driven mechanism(s) determine the formation of the a extended circumstellar envelope. The time scale of the AGB phase for a particular source is determined by its mass-loss rate. In fact, the end of the AGB phase is determined by the ejection of its stellar atmosphere, i.e., once the mass of the stellar envelope is $< 10^{-3} M_{\odot}$, the system composed by both the extended CSE and what remains of the star (the former stellar C-O core surrounded by a small mass envelope) begins its evolution throughout the post-AGB phase (section 1.3).

1.2.1 The circumstellar envelope

As discussed above, a consequence of the thermal instabilities during the evolution of stars along the AGB phase is the ejection of mass from the most external layers of the stellar atmosphere. Observational studies suggest that at the beginning of the AGB phase the mass-loss rate is of the order of $\dot{M} = 10^{-8}$ $M_{\odot}$ yr^{-1}, and can reach values of the order of $\dot{M} = 10^{-4}$ $M_{\odot}$ yr^{-1} near to the end of the AGB phase[1]. The mass-loss rate, one of the most important parameters within the study of AGB stars, determines the time scale of the evolution along the AGB phase. The ejected material is slowly driven outwards by the stellar wind, with typical velocities between 5-15 km s^{-1}. This process leads to the formation of a dusty and molecular-rich CSE. In general, it is thought that the formation of the stellar wind is a consequence of the formation of solid particles which efficiently exchange momentum with the stellar radiation field gaining acceleration in the radial direction. Thus, the dust particles drag the gas outwards by collisional exchange of momentum (Lamers and Cassinelli 1999). But in particular, this scenario does not suit the formation of the stellar wind for M-type AGB stars without requiring specific dust grain properties. Consequently, the driving mechanism and the formation of the CSEs of AGB star is yet poorly understood.

Nevertheless, it is acknowledged that the formation of CSE is determined by the mass-loss rate, and the formation of molecules and dust particles must be a key factor for the formation of the CSEs. At a certain distance from the stellar atmosphere, the shocks induced by the stellar pulsations set the proper density and temperature conditions for chemical reactions to produce di- and polyatomic molecules such as Carbon monoxide (CO), Silicon monoxide (SiO), Water (H_2O), Silicon carbide (SiC), Hydrogen cyanine (HCN), among others. Further out in the CSE, the conditions are favorable for the condensation and subsequent nucleation of solid material; dust grains of micrometer size. Although the amount

[1] In contrast, the mass-loss rate of the Sun is of the order of $\dot{M} = 10^{-14}$ $M_{\odot}$ yr^{-1}, and the velocity of the solar wind is ~ 500 km s^{-1}.

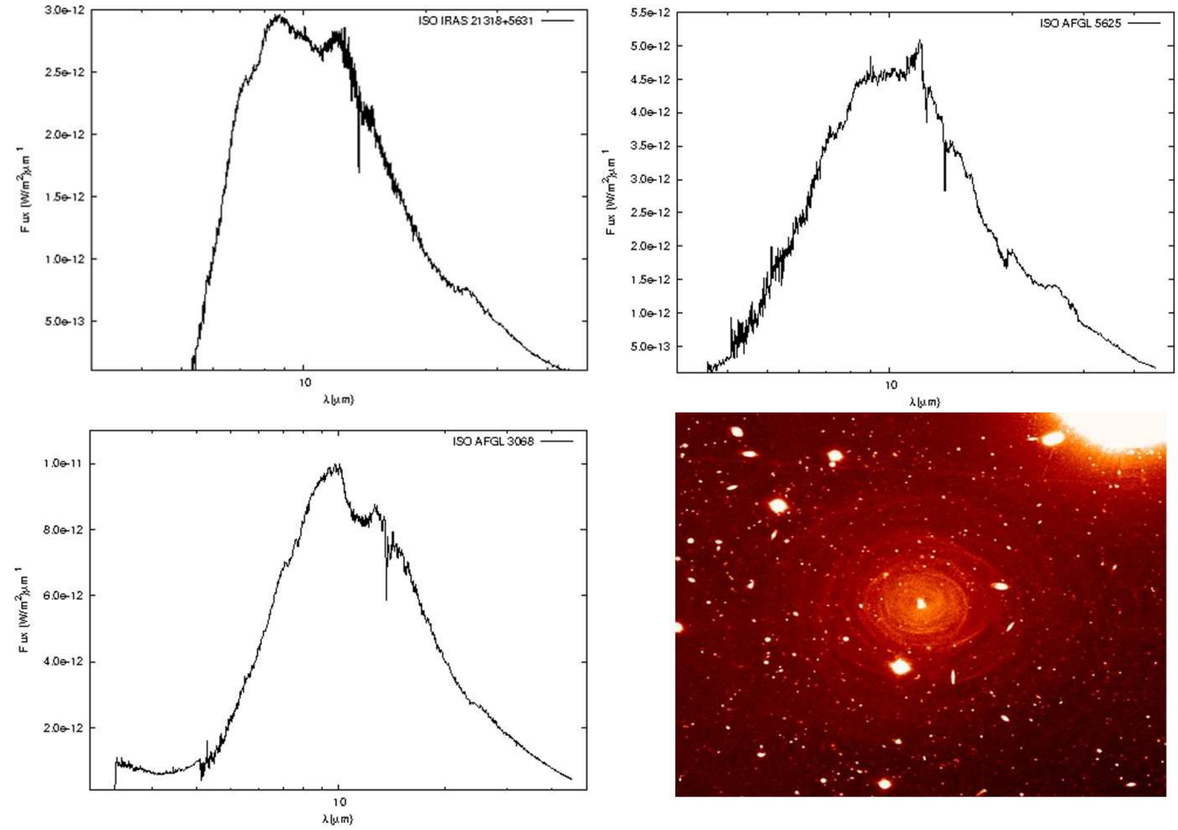

Figure 1.4: SWS ISO spectra of three carbon rich AGB stars, and the infrared image of IRC+10216 (bottom right). The emission at the infrared is dominated by thermal dust emission of the CSEs. The most evident features are observed at $\lambda \sim 11\mu\ m$ and $\sim 26\mu\ m$. The former is associated to SiC grains (Lorenz-Martins and Lefevre 1994), whereas the latest is associated to MgS grains (e.g Hony, Waters and Tielens 2002). IRC+10216 image credits: Izan Leao (Universidade Federal do Rio Grande do Norte, Brazil).

of dust grains represent only one percent or less of the mass of the gas ejected, the high efficiency of absorption of the stellar radiation field at short wavelengths (optical and near infrared wavelength range) make them play a very important role in the dynamics of the CSE. The dust formation leads to an increase of the opacity of the CSE, which reaches its peak value at the end of the AGB phase. Due to the high absorption efficiency of the dust grains, the radiation produced by the central star at shorter wavelengths (typically at 1μm) is absorbed and eventually reemitted as thermal dust radiation at mid- and far-IR wavelengths. In fact, the central star is obscure at the optical and near-IR wavelength range. But in turn, AGB stars, in particular those at the end of the AGB phase, are among the brighter Galactic sources at the IR. Therefore, the spectral energy distribution at the IR is dominated by the dust emission (Fig. 1.4), with typical peak values between 10 and 20 μm.

The temperature distribution throughout the CSE is determined by the interplay between the dust grains and the different radiation fields permeating it, but in particular, with the radiation field from the central star. The dust and molecular species formed in the CSE are determined by the relative abundance of C and O of the stellar atmosphere at the time when the material was ejected. Observations at the IR combined with laboratory measurements and the results of radiative transfer models, have lead to the identification of the most abundant dust grain species formed within the CSEs. For instance, either amorphous carbon or silicate grains are thought to produce the dust continuum emission observed at the IR of C-type AGB or M-type AGB stars, respectively. The emission from other grain species are observed as emission or absorption features on top of the continuum emission.

The formation of the molecular gas takes place at regions with temperatures below T = 3000 K, within the extended stellar atmosphere and throughout the CSEs. The time scale for a particular chemical process must be shorter than the time scale of the dynamics within a particular region where a molecular species is formed. Close to the star, where temperature and density are higher, the molecular species which can be form are defined by local thermodynamic equilibrium (LTE), although non-LTE processes (shocks) also have strong influence on the formation of different molecular species. Within the LTE frame, the most abundant molecules formed are those with high dissociation energy such as H_2 and CO. Because CO is formed in high abundance, it locks up most of the available O and C. Then, depending on the value of the C/O ratio, the chemistry of the CSE will be characterized by either O-bearing (C/O< 1) or C-bearing (C/O> 1) molecules. Observations have shown that, after H_2 and CO, among the most abundant molecules in O-rich CSEs are SiO, H_2O, OH (hydroxyl), CO_2 (carbon dioxide), whereas towards C-rich CSEs they are SiC, HCN, and CN (cyano radical). In total, about 80 different molecular species have been identified towards the CSE of the AGB star prototype IRC+10216, although this number will increase due to ongoing surveys which include a number of C-type and M-type sources.
The abundance of a particular molecular species depends on the mass-loss rate of the star, the expansion velocity of the CSE, and both its formation and the photodissociation radii. The latest refers to the region where the abundance of a particular molecular species decreases by a factor of two from its initial value due to UV photons from the interstellar radiation field. Because the photodissociation radius depends on the dissociation energy of the molecule, the abundance of H_2 declines further out than the abundance of other molecules. Assuming a steady expanding CSE in the radial direction, and constant mass-loss rate during the AGB phase, the number density distribution of H_2 is parametrized as

$$n_{\mathrm{H}_2} \approx 10^6 \left(\frac{\dot{M}}{10^{-6}} \right) \left(\frac{15 \mathrm{~km~s}^{-1}}{\upsilon_\infty} \right) \left(\frac{10^{15} \mathrm{~cm}}{r} \right)^2 \mathrm{cm}^{-3}, \tag{1.1}$$

where $\dot{M}$ is measured in $\mathrm{M}_\odot \mathrm{~yr}^{-1}$, υ_∞ in km s^{-1} and r in cm. Thus, based on the number density distribution of H_2, the fractional abundance of other molecular species X in the CSE is given by

$$f_{\mathrm{X}}(r) = \frac{n_{\mathrm{X}}(r)}{n_{\mathrm{H}_2}(r)}. \tag{1.2}$$

For instance, average values measured are $f_{\mathrm{CO}} \sim 10^{-3}$, $f_{\mathrm{H_2O}} \sim 10^{-5}$, $f_{\mathrm{SiO}} \sim 10^{-6}$.
Most of the molecular gas species in the CSEs are form from the products of the different nucleosynthesis processes that take place in the interior of the star during their evolution. The subsequent expansion

of the CSEs eventually lead to the replenishment the interstellar medium, fact that makes AGB stars play an important role on the chemical evolution of their host galaxies.

By the study of the properties of the molecular in the CSEs, it is possible to have a rough idea about the mass-loss history of the AGB star. Observationally, the molecular gas content in the CSE is studied at near-IR using absorption lines, and from the mid-IR to radio wavelengths using both thermal and non-thermal line emission. Most of the observations at radio wavelengths are focussed on the detection of molecular emission lines. In particular, the millimeter and sub-millimeter wavelength range represent an unique spectral window for observations of a number of rotational transitions of molecules such as CO, SiO, H_2O, HCN, SiS, NaCl, among many others, which allow the study of different spatial scales within the CSEs. About 80% of the molecules in the CSEs have been detected at radio wavelengths. The excitation conditions of the rotational levels of different molecular species and their abundance throughout the CSEs of AGB stars is such that line emission from different molecular species highlights different regions within the CSEs. A general description of radio observations of the molecular component of CSEs of AGB stars is presented in section 3.1 .

1.2.2 Circumstellar maser emission: Overview

Microwave amplification by stimulated emission of radiation (Maser) is also generated naturally in the CSEs of AGB stars. In particular, a number of rotational transitions which belongs to different vibrational levels of SiO, and to the ground vibrational levels of HCN, H_2O, SiS and OH have been detected producing maser emission throughout the CSEs of AGB and post-AGB sources. Astronomical masers are bright and intense spots towards dense enviroments, ideal for interferometric observations. Maser emission of SiO, H_2O and OH have been detected towards O-rich CSEs of AGB stars. Because the density and temperature conditions required for the pumping mechanism to operate for each molecular species is different, the emitting regions are also differenciated within the CSE (Fig. 1.5).
Although it is still unclear which is the main pumping mechanism of the SiO maser transitions, it is well known that the emitting region is located between the stellar photosphere and the dust-forming radius; in the so-called extended atmosphere. Interferometric obervations have revealed that the SiO maser emitting regions form ring-like structures centred on the star at distances ranging between $\sim$ 2-6 $R_\star$ (see Diamond et al. 1994; Boboltz and Diamond 2005). Because the SiO abundance is affected by the formation of silicate grains, SiO maser emission is not expected to trace regions beyond the dust-formation radius. The high variability of the SiO maser spectra shows the complex dynamics of the SiO maser region. In addition, the fact that rotational transitions in vibrational excited levels up $v = 4$ are detected with similar distribution indicates that the pumping mechanism of SiO is not yet completely understood.

Further out in the CSE, at intermediate distance from the star (typically a few tens to hundred of AU), the H_2O maser region is found. It is thought that the main pumping mechanism are collisions with neutral molecules. Therefore, the maser emission region is bound by the collision rates. H_2O is among

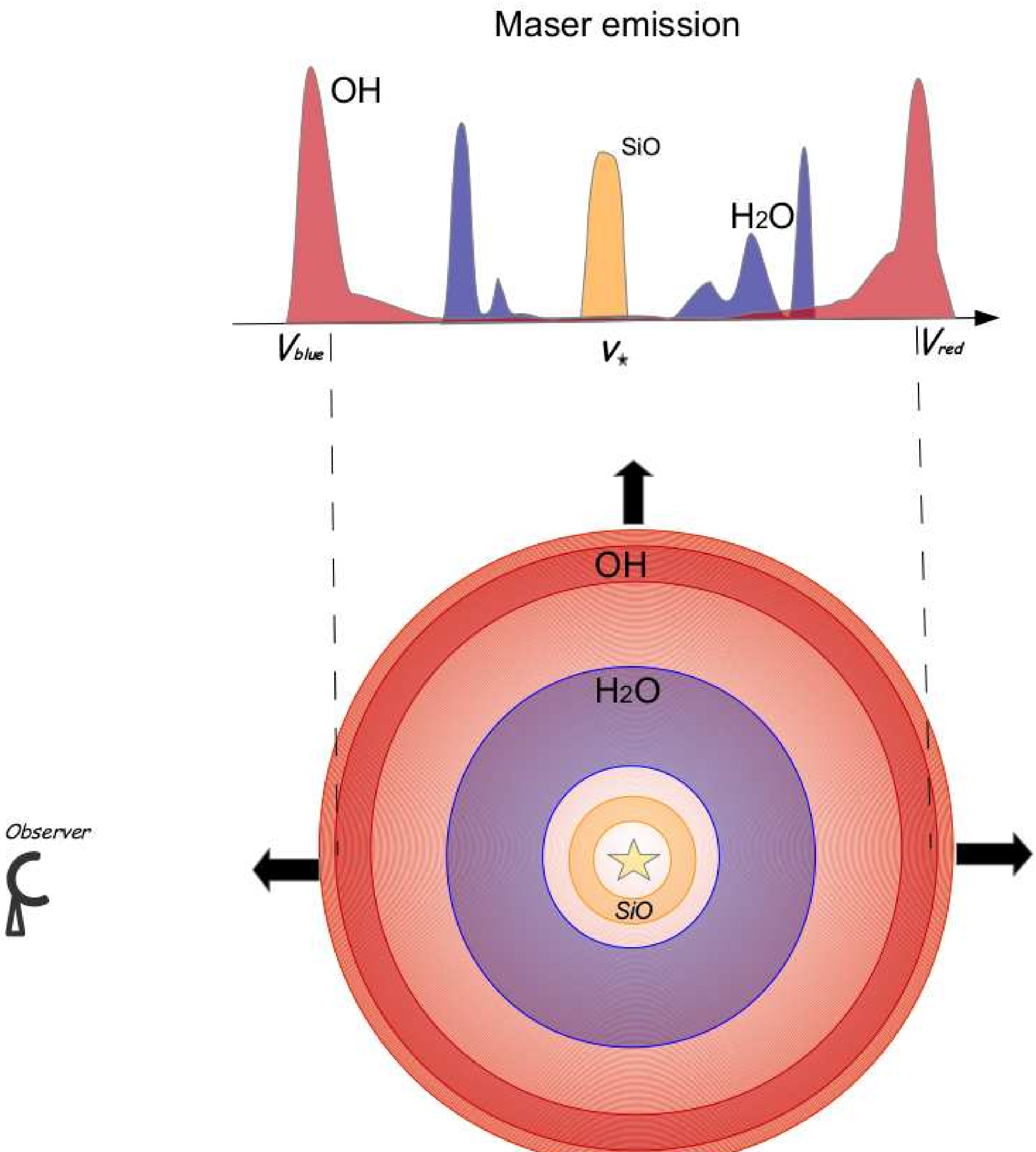

Figure 1.5: Schematic representation of the regions where the SiO, H_2O and OH are generated in the CSEs of AGB stars, and their spectra. The OH maser emission traces the outermost region of the CSEs, therefore the peaks of the emission appear at the most blue- and red-shifted velocities with respect to the systemic velocity ($v_\star$). SiO maser emission arise from regions close to the star, interior to the dust formation ratio. The velocity of the SiO spectral features is close to and centered on the systemic velocity. The H_2O maser emission arise from an intermediate region of the CSE, and its spectral features are spread over the velocity range defined by the OH spectral features. The sketch is not scaled.

the most abundant molecules the CSEs of late-type stars (e.g. Maercker et al. 2008; Menten, Melnick and Phillips 1990). The most studied H_2O maser emission is the low-frequency 6_{16}-5_{23} transition at 22.2 GHz. Since this transition is not affected by the atmospheric precipitable water vapor (PWV), it has become a reference in the study of water maser emission from astrophysical sources. It has been detected towards the expanding CSEs of late-type stars, tracing regions that are still undergoing acceleration, and high-velocity outflows generated in the envelope of post-AGB stars. This variety of scenarios gives us an idea of the broad excitation conditions of the 22.2 GHz maser (high-density regions $n_{H_2} > 10^8$ cm^{-3} and temperatures 2000 K > T > 200 K, Neufeld and Melnick (1991); Humphreys (2007)).

The photodissociation of H_2O lead to the formation of OH at the outermost regions of the CSEs of AGB stars. OH maser emission from the ground vibrational level at 1612 MHz (satellite line) and at 1665 and 1667 MHz (main lines) are observed tracing the steady expanding regions of the CSEs of O-rich CSEs. OH was the first molecular species found producing maser emission towards late-type stars (Cohen 1989). Indeed, the OH/IR sources are bright infrared M-type AGB stars with strong 1612 MHz OH maser emission. Because these are bright sources at the IR, the pumping mechanism of the 1612 MHz line is though to be radiative through OH IR lines at 35 μm and 53 μm, while the pumping mechanism for the main-line transition is not well determined yet. In particular, the double-peak spectral feature observed at 1612 MHz towards steady-expanding, spherical CSEs is thought to define the expansion velocity of the CSE, tracing regions at distances of the order of 10^{16}cm from the central star. In fact, the velocity separation between the blue- and red-shifted peaks is centered at the systemic velocity of the central star (figure 1.5).

Finally, HCN and SiS maser emission have been detected towards the C-rich CSEs, arising from regions similar to those traced by SiO in the O-rich CSEs. The pumping of the HCN maser transitions observed ($J = 1 - 0$ and $J = 2 - 1$) is more likely caused by the absorption of infrared photons rather than by collisions, though a combination of both processes cannot be ruled out (Goldsmith et al. 1988).

Therefore, observations of maser emission arising from different regions towards AGB stars can probe the kinematics of the molecular gas throughout the CSEs. Furthermore, polarized maser emission is usually detected towards the most bright and compact spots. Hence, the intensity of the magnetic field permeating the emitting region can be measured, and consequently, its large-scale morphology can be traced by detecting polarized maser emission from different molecular species.
The description of the generation and propagation of maser radiation is given in chapter 2.

1.3 Beyond the AGB: Post-AGB Stars

Post-AGB stars are thought to represent the group of stars that recently left the asymptotic giant branch phase and will develop into a planetary nebula (van Winckel 2003). The post-AGB is a very short time scale phase compared to the standard time scale of stellar evolution. It can be as short as 100 yr for the higher mass sources. Once the hydrogen-rich stellar atmosphere has been ejected, the mass-loss rate decreases to its minimum value and the central star evolves to higher temperatures while its luminosity remains roughly constant. At the same time, the CSE slowly detaches from the central star and cools. The spectral energy distribution (SED) at the infrared (IR) of post-AGB stars are characterized by the contribution of the stellar radiation at the near-IR and the thermal dust emission at mid- and far-IR. As the CSE expands, the distribution of temperature which characterizes the dust emission during the AGB phase changes. The SED at the mid-IR begins to display stronger emission features over the continuum emission that dominates the SED during the AGB phase. The effective temperature of the central star increases, reaching temperatures $> 1.5 \times 10^4$ K. At the end of the post-AGB phase, the energy of the radiation field produced by the central star increases. This results in the production of high energy photons able to photoionize the inner shells of the CSE, leading to the formation of outstanding sources with a wide variety of morphologies known as Planetary Nebulae (PNe, Fig. 1.6).

It is generally assumed that the mass-loss process along the evolution in the AGB is spherically symmetric. However, a high percentage of PNe have been observed displaying aspherical symmetries that include elliptical, bipolar or multipolar shapes. It is still unclear at what point in the evolution toward a PNe the departure from the spherical symmetry starts and even more importantly, what the physical processes involved to form the complex shapes observed are. The evolution of the CSEs beyond the AGB phase often involves the interaction between a fast collimated wind, which could be created during the very last thermal pulses of the central star; and the steadily expanding CSE formed during the AGB. Therefore, the post-AGB is a key phase for the understanding of the evolution of the CSE, where the mechanism(s) responsible for shaping asymmetric PNe must become more important than the mechanism responsible for the mass-loss.

Observational surveys focused on post-AGB stars have revealed that their CSEs display clear signatures of aspherical morphologies such as axisymmetric outflows or equatorial density enhancements (e.g. Bujarrabal et al. 2001). This fact indicates that the departure from the spherical symmetric scenario assumed for the mass-loss along the AGB phase takes place before the CSEs becomes photoionized. In particular, post-AGB sources displaying bipolar or multipolar outflows have became an unique case for the study of the mechanism shaping the CSEs. Bujarrabal et al. (2001) measured the linear momentum of the bipolar outflows observed towards a set of sources in transition between the AGB and the PN phase. Their results prove that the momentum measured towards those fast outflows exceeds the maximum momentum provided by radiation pressure alone, in some cases by a factor of 1000. Therefore, a different energy source is needed in order to trigger the ejection of such collimated high-velocity outflows. Another evidence of the propagation of collimated high-velocity outflows generating strong shocks within the CSE is the detection of post-AGB sources with water maser emission spread over unusually large velocity ranges ($\geq$ 100 km s^{-1}, Likkel and Morris 1988) the so called water fountains (Section 1.3.1). The effects of accretion of circumstellar mass on stellar or substellar companions; and large scale magnetic fields are strong candidates to be the source of that missing energy. However, the lauching mechanism of the high-velocity outflows, as well as the origin of the collimating magnetic field, are still under debate. The short time scale of the post-AGB phase represent a observational challenge, and multiwavelength observations of a large group of late AGB and post-AGB are required to

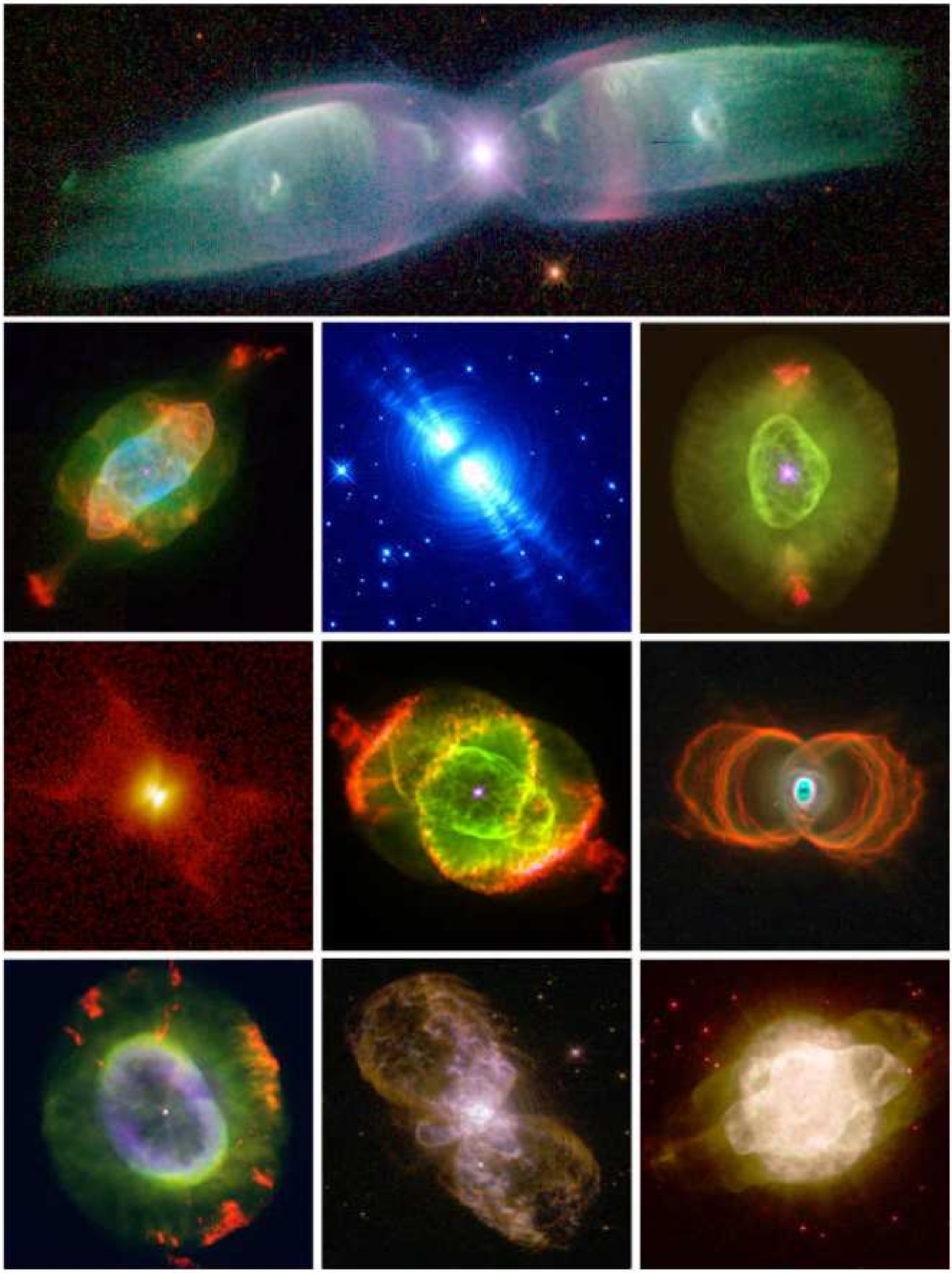

Figure 1.6: A sample of the wide variety of morphologies observed at the planetary nebula phase. Credits: Bruce Balick, Howard Bond, R Sahai, their collaborators, and NASA.

constrain, in particular, the physics behind the shaping of their CSE.

1.3.1 Water fountains

As mentioned in section 1.2.2, a number of rotational transitions of SiO, H_2O, OH, HCN and SiS have been observed producing maser emission from different regions in the CSEs of AGB stars. The OH maser emission is detected arising from the outermost regions of the CSEs, producing a characteristic double-peak spectrum. Typically, for spherically symmetric CSEs, the two peaks observed in the OH maser spectra defines the most blue- and red-shifted velocities of the CSEs in the line-of-sight with respect to the stellar velocity. In addition, the velocity range of the H_2O maser spectra is narrower than the velocity range of the OH, because the region in the CSE where the H_2O masers are generated is closer to the central star and is still being accelerated. Hence, all the spectral features from H_2O and the other molecular species producing maser emission are expected to appear within the velocity range defined by the the OH spectra for a specific source (figure 1.5). The same result has been found in most of the cases towards post-AGB sources. However, a class of post-AGB stars, the so called "Water Fountains", is characterized by the detection of H_2O maser emission over an unusually large velocity range broader than the velocity range defined by the OH maser emission. Sources with H_2O maser velocity spread over ranges from 100 to 500 km s^{-1} have been detected (e.g. Likkel and Morris 1988; Deacon et al. 2007, Walsh et al. 2009, Gómez et al. 2011). Those H_2O masers have been observed tracing regions where the interaction between the axisymmetric high-velocity outflow and the slow AGB wind seems to be active. Thus, the H_2O masers are probably excited along the outflow, in a region where the density is affected by the propagation of the shock-front of the high-velocity outflow. Recent infrared imaging of water fountains have revealed bipolar and multipolar morphologies (Lagadec et al. 2011). Despite the small number of post-AGB sources confirmed up to date displaying high-velocity H_2O maser emission (14 sources), it seems that this kind of sources have only recently passed along the evolutionary stage where the onset of high-velocity outflows occurs, i.e. water fountais may represent those post-AGB sources with kinematic ages of a few tens of years. Therefore, water fountains provide an unique scenario to test the different hypotheses addressed in the literature to explain the formation of the different morphologies observed at the PN stage, or at least of those displaying bipolar or multipolar lobes. In this context, it is necessary to constrain the physical conditions of the gas where the H_2O maser emission is generated. Single dish observations give important information about the intensity of the maser emission, whereas interferometric observations seems to be the most suitable technique to study their spatial distribution in the high-velocity outflows, as well as the polarized emission from different maser spots. For instance, Vlemmings, Diamond and Imai (2006) have detected circular and linear polarization in the H_2O maser features along the jet of W43A, the archetypal water fountain. They found that the jets of W43A are magnetically collimated. Therefore, the detection of polarized maser emission from water fountains is useful to determine the role of the magnetic fields on the onset of wind asymmetries during the evolution from AGB stars to aspherical PNe.

A general description of interferometric observations of maser emission is given in section 3.2. The results of our interferometric observations of polarized H_2O maser emission carried out towards two water fountains are presented in chapter 5.

1.4 Radiative transfer

The observational study of the CSE of AGB stars is complemented with numerical models aimed to reproduce the observed spectral energy distribution of the dust at the infrared, as well as to fit the molecular line emission observed at (sub-)millimeter wavelengths for a particular molecular species. The measured intensity towards an AGB source is the result of the propagation of the stellar radiation field through the dense CSEs. In order to obtain a detailed description of the interaction between radiation field and both the gas and dust content in the CSEs of AGB stars, it is necessary to solve the equation of radiative transfer.

In the general context, the radiative transfer equation describes the variation of the specific intensity of radiation within a certain frequency range as a function of the length travelled within a medium. It is given by

$$\frac{dI_\nu}{ds} = -\kappa_\nu\, I_0 + \epsilon_\nu, \tag{1.3}$$

where κ_ν and ϵ_ν are respectively the absorption and the emission coefficients of the medium. Defining the optical depth of the medium as $\tau_\nu = \kappa_\nu\, ds$, the equation 1.3 can be written as

$$\frac{dI_\nu}{d\tau_\nu} = -I_0 + S_\nu, \tag{1.4}$$

where $S_\nu = \epsilon_\nu/\kappa_\nu$ is the source function. In the case of molecular line emission, ϵ_ν and κ_ν are function of the level population of the upper and lower energy states of a particular transition

$$\epsilon_\nu = \tfrac{h\nu_{ul}}{4\pi} A_{ul}\phi_{u,\nu} N_u, \tag{1.5}$$

$$\kappa_\nu = \tfrac{h\nu_{ul}}{4\pi}(N_l B_{lu}\phi_{l,\nu} - N_u B_{ul}\phi_{u,\nu}), \tag{1.6}$$

where N_u and N_l are the number density of molecules in the upper and lower energy states of the transition; A_{ul}, B_{ul} and B_{lu} are the Einstein coefficients, and $\phi_{i,\nu}$ is the frequency profile given by the velocity distribution of either energy state. At the radio frequencies, a Maxwellian distribution with the same temperature can describe the velocity distribution of all energy states, then it can be assumed that $\phi_{u,\nu} = \phi_{l,\nu} = \phi_\nu$. The Einsten coefficients satisfy the relations $A_{ul}/B_{ul} = 2h\nu_{ul}^3/c^2$ and $B_{lu}/B_{ul} = g_u/g_l$, where g_i is the statistical weight of the different levels, and the number density per sub-level is $n_i = N_i/g_i$. Thus, from these relations and using equations 1.5 and 1.6, the source function S_ν becomes

$$S_\nu = \frac{2h\nu_{ul}^3}{c^2}\left(\frac{n_l}{n_u} - 1\right)^{-1}. \tag{1.7}$$

Therefore, the level population of the molecular gas needs to be known in order to solve the equation of radiative transfer. In the case of the molecular gas in the CSEs of AGB stars, the solution of the radiative transfer equation depends on the distribution of the level population of all the radiative transitions of a particular molecular species, whereas for the dust it depends on the optical properties (absorption, emission and scattering) of the grains considered for a particular model. Within the LTE frame, the distribution of level population of the molecular species is determined by the kinetic temperature of the gas, and the solution of the radiative transfer equation is straightforward. Nevertheless, most detailed radiative transfer models including the effects of cooling (e.g. adiabatic expansion, diffuse emission) and heating (e.g. momentum exchange between gas and dust) processes, which certainly affects the intensity of the emergent radiation field, are needed in order to constrain physical parameters such as temperature and density distribution in the CSEs.

The most reliable numerical solutions of the equation of radiative transfer are those which includes the Monte-Carlo method. It is widely used in mathematics and physics in order to solve complex systems which include large set of parameters. It is characterized by the random variation of one or more input parameters which are iterated until their convergence. For the CSEs of AGB stars, the Monte-Carlo method is implemented to calculate the temperature distribution of the dust as well as the level population of a particular molecular species, for a given temperature of the central star and a density distribution of the CSE. In the most general case the central star is assumed to radiate as a black body with a given temperature (although there are codes that include more exact stellar spectra). Then, the energy of the model photons per unit frequency range is defined according to the energy distribution of the radiation field produce by a source at such temperature. The model photons, which are basically energy packages per unit frequency range, are simulated to propagate throughout the CSE. The density distribution of the gas and dust in the CSEs is an input of the model, and it can be defined as a function of one, two or the three spatial variables (1-D, 2-D and 3-D models). In the general case, the propagation of the model photons is tracked throughout the CSE. The interaction points are randomly chosen according to a probability function, and at each interaction point the energy of the model photons is changed due to absorption or stimulated emission accordingly to the Monte-Carlo method. In addition, the new direction of propagation is randomly chosen at each interaction point. In general, the local emission is assume to be isotropic, and the propagation of the model photon can be in any direction from a interaction point. In the case of dust, detailed models use a probability function which depends on the scattering properties of the dust species under study to calculate the new propagation direction of the model photon after each interaction. The propagation of the model photons is tracked until either it leaves the CSE or all its energy is diluted by multiple interactions with the CSE material. Then, the propagation of the next model photon is simulated. After each model photon, the level population of the gas is obtained. After a number of photons simulated, if the level population is essentially unchanged from one model photon to the next, the process ends and the radiative transfer equation is solved for the obtained level population. In the case of dust, is the thermal equilibrium between the stellar radiation field and the temperature of the grains what determines the convergence.

In this thesis, a full-3D radiative transfer code was used to simulate the CO molecular line emission towards the CSEs of AGB stars. The code, Line modelling engine (LIME; Brinch and Hogerheijde 2010), designed for the prediction of line and continuum emission from astrophysical sources such as dense cores in star forming regions, and molecular envelopes, is a reliable tool to model the molecular emission towards CSEs without restriction on the adopted geometry. The results of the models are presented in Chapter 7.

1.5 Aims of this thesis

Within the general scenario of the study of the evolution of low- and intermediate-initial-mass stars, the search for an explanation that suits mass-loss process and the kinematics of the ejected mass from fundamental principles has became the main goal of observational, theoretical and computational efforts. Observational studies of thermal CO line emission are considered one useful method to constrain the mass-loss history and the density distribution of the molecular gas formed from the material ejected during the AGB phase. However, a number of assumptions have to be done in order to draw conclusions from the observed spectral features within a yet large uncertainty range. In this specific context, one of the questions addressed in this thesis is: What is the maximum degree of asymmetry of the CSEs that can be properly modelled assuming a spherically symmetric source?
In Chapter 7 I present the results of LIME modelling of CO line emission assuming different morphologies for the CSEs, from the typical spherical symmetric to oblate ellipsoids.

On the other hand, a high percentage of sources evolving along the PN phase display non-spherical symmetric CSEs. Among the wide range of observed shapes, sources displaying axisymmetric morphologies have been detected, not only along the PN phase, but also along the post-AGB phase. Since the energy necessary to develope collimated outflows exceeds the energy provided by radiation pressure of the stellar radiation field on the ejected material, a number of mechanism have been proposed in order to explain the formation of such morphologies. However, there is no general agreement up to date. In this context, part of the research in this thesis is focussed on the study of the role of the stellar magnetic field on the formation of collimated high-velocity outflows. This study was carried out using interferometric observations of water fountain sources. The results of the observations are presented in Chapters 5 and 6.

One of the methods used for the study of the magnetic field towards the CSEs of AGB and post-AGB stars relies on the detection of polarized maser emission. Since there are non-Zemman effects which can mimic or enhance the polarization state of the maser radiation, part of the research in this thesis is focussed on the study of the polarization properties of SiO, H_2O and HCN maser emission. The question addressed in this particular study is: What is the maximum fractional linear polarization that can be detected at the ALMA frequency range, which can be truly related to the presence of magnetic field in region where the maser emission is generated? The results of this study are presented in Chapter 4.

CHAPTER 2

Maser emission

In order to generate maser emission from a particular rotational transition, it is necessary to produce an inversion of population of the energy levels involved in the radiative transitions. Then the maser is generated by stimulated emission which amplifies the intensity of the incoming radiation field. Such inversion of population requires a pumping mechanism, which basically creates an unstable distribution of energy where the population of the upper level exceeds the population of the lower level of a given transition. The main pumping mechanism depend on the molecule, and its efficiency depends on the density of the region where the maser emission is produced. It can be radiative or collisional (or a combination), and the energy levels involved in the rotational transition are just a small part of a complex cycle which includes a number of different rotational and vibrational transitions within the scheme of energy levels of a particular molecular species (Elitzur 1992; Cohen 1989). Besides the pumping mechanism, maser emission requires velocity coherence within the emitting gas. That is, the velocity gradient along the amplification path cannot be larger than the Doppler shifting defining the maser emission linewidth. In the most general frame, maser emission is generated by stimulated emission between two energy levels. Within the basic two-levels maser emission frame the equation of transfer that describes the variation of the intensity (I_ν) is

$$\frac{dI_\nu}{ds} = -\kappa_\nu I_\nu + \epsilon_\nu, \tag{2.1}$$

where the absorption (κ_ν) and the emission (ϵ_ν) terms are function of the number density of molecules in the lower (N_l) and upper (N_u) energy state, the linewidth function ($\Delta\phi$), and the Einstein coefficients for spontaneous emission and both absorption and stimulated emission ($A_{ul},\ B_{lu},\ B_{ul}$)

$$\kappa_\nu = \frac{h\nu}{4\pi}\phi(\nu)(N_l B_{lu} - N_u B_{ul}), \tag{2.2}$$

$$\epsilon_\nu = \frac{h\nu}{4\pi}\phi(\nu) N_u A_{ul}. \tag{2.3}$$

The Einstein coefficients satisfy the relations

$$A_{ul} = \frac{2h\nu^3}{c^2} B_{ul}, \qquad g_l B_{lu} = g_u B_{ul}. \tag{2.4}$$

where g_l and g_u are the statistical weights of the lower and upper states, respectively. Replacing κ_ν and ϵ_ν in Eq. 2.1 and assuming that the two levels of the transition have the same statistical weight, i.e. $g_u = g_l$, then the radiative transfer equation becomes

$$\frac{dI_\nu}{ds} = \frac{h\nu}{4\pi}\phi(\nu)\Big[(N_u - N_l)B_{ul} I_\nu + N_u A_{ul}\Big]. \tag{2.5}$$

Therefore, if for any reason the population of the upper level exceeds the population of the lower state, the medium acts like an amplifier rather than an absorber. As mentioned before, the maser transition is one among a complex cycle of radiative emission and absorptions throughout different rotational and vibrational levels of a particular molecular specie. Therefore, the description of the radiative transfer of maser emission must be generalized including gains and losses due to population exchange with other radiative levels which do not interact directly with the maser radiation. Thus, by including the pumping rates $\mathcal{R}_{i\nu}$ and the decay rate Γ_i we can describe the interaction of the maser levels with all the other transitions. The line shape function $\phi(\nu)$ describes the line shape of the emission, and because the particle motions, the frequency of a given transition is shifted into the interval $[\nu, \nu + d\nu]$ due to the Doppler effect. The population of the levels that are not involved in the maser are unaffected by the maser transitions, then their corresponding frequency distributions can be expected to follow the Doppler profile. This assumption allow us to write the pump rates into the interval $[\nu, \nu + d\nu]$ as $\mathcal{R}_{i\nu} = \mathcal{R}_i\phi(\nu)$. The rate equations for the level population of the states generating the maser are given by

$$\frac{\partial N_{u\nu}}{\partial t} = -(N_{u\nu} - N_{l\nu})B_{ul}J_\nu - N_{u\nu}A_{ul} + \mathcal{R}_{u\nu} - \Gamma_u N_{u\nu} - (N_{u\nu}C_{ul} - N_{l\nu}C_{lu}), \tag{2.6}$$

$$\frac{\partial N_{l\nu}}{\partial t} = (N_{u\nu} - N_{l\nu})B_{ul}J_\nu + N_{u\nu}A_{ul} + \mathcal{R}_{l\nu} - \Gamma_l N_{l\nu} - (N_{l\nu}C_{lu} - N_{u\nu}C_{ul}), \tag{2.7}$$

where J_ν is the angle-averaged intensity given by $J_\nu = \frac{\Delta\Omega}{4\pi} I_\nu$; C_{ul} and C_{lu} are the collision rates for excitation and de-excitations that parametrize the collision rate with different molecular species than the molecule producing the maser. In addition, the decay rate (Γ_i) is defined as the inverse lifetime of the masers states. In the steady-state case, both Eq. 2.6 and Eq.2.7 are zero. Defining the population per sub-level as $n_{i\nu} = N_{i\nu}/g_i$, and adding Eq. 2.6 and Eq. 2.7 lead to define the overall level population of the maser system as a function of both the pump rate per sub-level ($\mathcal{P}_i = \mathcal{R}_i/g_i$) and the decay rate

$$n_\nu \equiv n_{u\nu} + n_{l\nu} = \frac{(\mathcal{P}_u + \mathcal{P}_l)\phi(\nu)}{\Gamma} = n\phi(\nu), \tag{2.8}$$

where we have assumed that $\Gamma_u = \Gamma_l \equiv \Gamma$ and that the degeneracy of both levels are the same, i.e. $g_u = g_l \equiv g$. Neglecting the effects of the collisions exchanges and diffuse radiation caused by spontaneous emission, it is possible to derive the level population difference (Δn_ν) from Eq. 2.6 and Eq. 2.7 as a function of both the pump and decay rates

$$\begin{aligned}\Delta n_\nu &= \frac{(\mathcal{P}_u - \mathcal{P}_l)\Gamma^{-1}}{1 + 2B_{ul}J_\nu/\Gamma}\phi(\nu) \\ &= \frac{(\mathcal{P}_u - \mathcal{P}_l)\Gamma^{-1}}{1 + J_v/J_s}\phi(\nu), \\ &= \frac{\Delta n_0}{1 + J_\nu/J_s}\phi(\nu),\end{aligned} \tag{2.9}$$

where J_s has been defined as the ratio between the decay rate and the stimulated emission coefficient, i.e. $J_s \equiv \frac{\Gamma}{2B_{ul}}$, and $\Delta n_0 = (\mathcal{P}_u - \mathcal{P}_l)\,\Gamma^{-1}$.
If spontaneous emission is considered, then a factor of (A_{21}/Γ) will appear in Eq. 2.9, and because the spontaneous emission rate is far to small compared to the decay rate for astronomical masers, $A_{21} \ll \Gamma$, the effects on the population level of diffuse radiation can be neglected. On the other hand, considering the collision rates, a factor (C_{21}/Γ) will also appear in Eq. 2.9. In this case, when the collision rate are larger than the decay rate, the inversion of population is expected to be destroyed, and the maser cannot operate. Then, in order to have an efficient pump mechanism to create the inversion of the level population, it is necessary to have collision rates such that $\Gamma > C_{21}$. Moreover, because the term J_ν/J_s in Eq. 2.9, the level population difference depends also on the intensity of the maser radiation.
The efficiency of the pumping mechanism can be parametrized using equations 2.8 and 2.9

$$\eta = \frac{\mathcal{P}_u - \mathcal{P}_l}{\mathcal{P}_u + \mathcal{P}_l} = \frac{\Delta n_0}{n}. \tag{2.10}$$

Thermal lines requires that $\mathcal{P}_l > \mathcal{P}_u$, while for maser emission $\mathcal{P}_u > \mathcal{P}_l$ is necessary.
From the expression for the population difference (Eq. 2.9) and the Eq. 2.2, it is possible to write κ_ν, which no longer describes absorption but amplification, as

$$\kappa_\nu = \frac{\kappa_{0\nu}}{1 + J_\nu/J_s}, \tag{2.11}$$

where

$$\kappa_{0\nu} = \frac{h\nu}{4\pi}\Delta n_0 g_u B_{ul}\phi(\nu). \tag{2.12}$$

The dependence on the intensity is retained in Eq. 2.11 with the parameter J_ν. Moreover, the dependence of the amplification on the intensity of the maser is scaled by J_s. In the limit case $J_\nu \ll J_s$, both the population difference Δn_ν and the gain κ_ν are independent of the intensity of the maser radiation (Eq. 2.9 and Eq. 2.11). This is the so called unsaturated maser regime. Therefore, the solution of the radiative transfer equation in the frame of unsaturated maser emission ($J_\nu \ll J_s$) can be written as

$$I_\nu(s') = \left(I_\nu(0) + \frac{\epsilon_\nu}{\kappa_{0\nu}}\right)e^{\kappa_{0\nu}\ s'} - \frac{\epsilon_\nu}{\kappa_{0\nu}}. \tag{2.13}$$

where it is clear that the intensity of the maser increases exponentially with distance traveled within the maser region. In the unsaturated frame regime, $\kappa_\nu \propto \Delta n_0 = n\eta$, which indicates that the gain of unsaturated masers depends on the efficiency pumping mechanism. Then, a small change on the parameter η implies strong variability of the outcoming intensity of the maser radiation.
For sufficiently long paths, the beam-average intensity J_ν eventually exceeds J_s, which naturally prevents infinite energy flux. In this case, the maser radiation is saturated, and both the gain and the population difference are affected by the intensity of the maser radiation. Therefore, in the limit case $J_\nu \gg J_s$, the gain is given by $\kappa_\nu = \kappa_{0\nu}\frac{J_s}{J_\nu}$, and with $J_\nu = \frac{\Delta\Omega}{4\pi}\ I_\nu$, the transfer equation becomes

$$\frac{dI_\nu}{ds} = \kappa_{0\nu} J_s \frac{4\pi}{\Delta\Omega} + \epsilon_\nu. \tag{2.14}$$

Then, since the beaming angle $\Delta\Omega \approx \frac{\pi\ s^2}{r^2}$, integrating Eq. 2.14 between s' and s''

$$I_\nu(s'') = I_\nu(s') + \frac{4}{3}\kappa_{0\nu} J_s \frac{(s''^{\ 3} - s'^{\ 3})}{r^2} + \epsilon_\nu(s'' - s'). \tag{2.15}$$

Therefore, once the beamed-averaged intensity becomes important, the intensity of the maser increases linearly with the path length, and the maser radiation is said to be saturated.

Maser spectra are characterized by very intense emission features with narrow line widths, high variability and polarization. The line profile is determined by the gain along the amplification path and whether the emission is unsaturated or saturated. Assuming that the line profile function $\phi(\nu)$ is Gaussian, then in the unsaturated regime the exponential gain towards the center of the line is higher than the amplification of the radiation towards the wings of the line. Therefore, the spectral features of unsaturated masers are more narrow than the typical thermal line profile of the same molecular transition. If the amplification path is long enough, the gain becomes linear as the emission saturates. Then, the emission towards the center of the line profile is not longer favored, and the line is then re-broadened. The upper limit for the re-broadened is the thermal linewidth of the studied transition.

2.1 Polarization: Overview

The polarization state of an electromagnetic wave is given by the oscillation of the electric field vector $\vec{E}$ in a plane perpendicular to the direction of propagation ($\vec{k}$) of the electromagnetic field. If the wave propagates along the direction of the z-axis, then the electric vector $\vec{E} = (E_x, E_y)$ is given by

$$E_x = \mathcal{E}_x cos(\omega t - \delta_x), \tag{2.16}$$

$$E_y = \mathcal{E}_y sin(\omega t - \delta_y), \tag{2.17}$$

where $\mathcal{E}_{x,y}$ and $\delta_{x,y}$ are the amplitude and phase of each component. In general the electric field vector traces out an ellipse in the x-y plane. Therefore the general polarization state of electromagnetic waves is elliptical. Two special cases of polarization are generated when the amplitudes of each component are the same and the phase difference are either $\pm\pi/2$ or zero. In the former case, when the phase difference $\Delta\delta = \delta_x - \delta_y$ are $\pm\pi/2$, the electric vector traces a circle in the x-y plane while the electromagnetic wave propagates. This is the case of circular polarization, where the electric field vector rotates in the clockwise ($\Delta\delta = -\pi/2$) or in the counter-clockwise ($\Delta\delta = \pi/2$) direction around the z-axis, defining the rotation direction from the point of view of the source. On the other hand, when the phase difference is zero, the electric field moves along one direction in the x-y plane, which is the case of linear polarization. In general, an emitting gas generate random polarized states such that, when averaged, results in an unpolarized radiation field. If for any reason the emission of radiation with a specific polarization state is enhanced, then the radiation field, after averaging, displays a fraction of its total flux being polarized. Circumstellar maser radiation is often found to be polarized. The detection of polarized maser emission is linked via the Zeeman effect to the presence of a magnetic field in the region where the maser radiation is generated (Cohen 1989). Polarization depends on the response to the presence of a magnetic field of the molecular species producing the maser radiation. In absence of magnetic fields, all the magnetic sublevels of a given energy state with angular momentum J have the same frequency. The energy degeneracy of the magnetic sublevels is lifted when a magnetic field is applied; this is the Zeeman effect. The number of magnetic sublevels of quantum number m of an energy level is $2J + 1$, and the allowed transitions have $\Delta m = m_u - m_l = 0, \pm 1$. Depending on the transitions between the sublevels, the polarization state detected is either circular or linear. Transitions with $\Delta m = 0$ produce linear polarized emission (π-component), while $\Delta m = \pm 1$ (σ-components) generate circular polarization. The σ-components of the line corresponds to clockwise (right-handed) or counter-clockwise (left-handed) circular polarization.

The Zeeman frequency ($g\Omega$), which is the frequency shift between the magnetic sublevels caused by a magnetic field, depends on the electronic structure of the studied molecular species. For open electronic shells molecules (radicals) such as OH, the Zeeman frequency is expected to be of the order of, or even larger than the intrinsic linewidth of the emission line $\Delta\omega$ (linewidth without Zeeman splitting). In the particular case of OH, a magnetic field of a few mG can shift the frequency of the magnetic sublevels such that the Zeeman frequency is larger than the intrinsic linewith of the maser line. Therefore, strong circular polarization is usually measured in the spectral features of OH maser emission.

The case of closed shell molecules such as SiO and H_2O is rather complicated. These are molecules with no net electronic angular momenta, and the response to a magnetic field is far too weak compared to the OH, for instance. The Zeeman frequency $g\Omega$ is expected to be smaller than the intrinsic linewidth, thus circular polarization is rarely detected. On the other hand, spectral features with fractional linear polarization are usually measured, although its interpretation needs to be carefully drawn. The case of SiO and H_2O polarized maser emission is addressed in chapter 4, where I present the results of the calculations of the fractional linear polarization observable in the (sub-)millimeter wavelength range.

2.1.1 Stokes parameters

The polarization properties of astronomical sources depends on the amplitude and phase of the components of the electric field vector, but non of them are measurable quantities. On the other hand, the polarization is in general a fraction of the total flux detected. Therefore, it is necessary to link the polarization properties of an observed signal, i.e. intensity, linear and circular polarization degree, and polarization angle; with values that can be extracted from the observations (Thompson, Moran and Swenson 2001). In observational astronomy, such link is done by the Stokes parameters. The Stokes parameters describe the polarization properties of a partially polarized electromagnetic field. If the components of the electric field vector are given by the equations 2.16 and 2.17, with the amplitudes and phases as a function of time, i.e., $\mathcal{E}_{x,y}(t)$ and $\delta_{x,y}(t)$, then

$$\begin{aligned}
I &=< \mathcal{E}_x^2(t) > + < \mathcal{E}_y^2(t) >, \\
Q &=< \mathcal{E}_x^2(t) > - < \mathcal{E}_y^2(t) >, \\
U &= 2 < \mathcal{E}_x^2(t)\, \mathcal{E}_y^2(t) \cos(\delta_x(t) - \delta_y(t)) >, \\
V &= 2 < \mathcal{E}_x^2(t)\, \mathcal{E}_y^2(t) \sin(\delta_x(t) - \delta_y(t)) >,
\end{aligned} \tag{2.18}$$

where the angular brackets denotes average on time. The four parameters are the measure of total intensity (I), linear polarized components along the x and y axis (Q, U), and the circular polarized component (V) of the detected radiation field. These parameters have units of flux density (or intensity) and their magnitudes can be used to know the polarization state of the detected radiation field. The linear and circular polarized fraction, as well as the angle of polarization are function of the stokes parameters

$$
\begin{aligned}
p_l &= \frac{\sqrt{Q^2 + U^2}}{I}, \\
p_c &= \frac{V}{I}, \\
p_t &= \frac{\sqrt{Q^2 + U^2 + V^2}}{I}, \\
\Theta &= \frac{1}{2}\tan^{-1}\left(\frac{U}{Q}\right),
\end{aligned} \tag{2.19}
$$

where p_l and p_c are the fraction of linear and circular polarization respectively, p_t is the total polarized emission and Θ is the angle of polarization of the linear polarized component. In the particular case of circumstellar maser emission, and generally in astronomy, $p_t \leq 1$.

The Stokes parameters lead to an accurate understanding of the polarization properties of the studied radiation field. In the context of circumstellar maser emission, the detection of fractional polarization is related to the presence of a magnetic field permeating the region in the CSEs where the maser emission is generated. Then, the fractional polarization detected can be used to determine the polarization state of the maser radiation in order to constrain the magnetic field morphology and strength. The morphology of the magnetic field can be constrained measuring the fractional linear polarization of the maser radiation p_l and its polarization angle Θ, which is related to the projection of the magnetic field lines on the plane of the sky. The strength of the magnetic field can be calculated using the fractional circular polarization of the maser emission. Thus, the spatial distribution of the magnetic field energy can be determined from observations of maser emission arising from different locations in the CSEs. Therefore, the energy of the magnetic field can be constrained and compared with the kinetic energy of the gas and dust components of the CSEs, and then, determine if the magnetic pressure is large enough to dominate the shaping of the CSEs of (post-)AGB sources.

CHAPTER 3

Radio observations of circumstellar envelopes of AGB stars

3.1 Observing the molecular gas towards CSEs

The wavelength range for the study of molecular gas in the CSEs of AGB and post-AGB stars covers from the far-infrared ($\lambda > 100\ \mu$m), where the high energy rotational transitions are detected, up to the centimeter wavelengths where the ground-state OH maser emission is observed. The atmospheric opacity (Fig. 3.1) is not a critical factor for observations at the centimeter wavelengths. In contrast, the high amount of precipitable water vapor (PWV) that the Earth atmosphere contains severely affects observations at (sub)millimeter wavelengths.
At the radio frequencies, the CSEs are detected through emission lines. At millimeter and submillimeter wavelengths, observations are possible only in few wavelengths bands where the absorption of the incoming signal is relatively low. In order to minimize the atmospheric effects on the incoming signal, telescopes operating at the submillimeter are typically located at very dry places, in deserts or at the summit of mountains at altitudes > 2500 m above the sea level. The Atacama Pathfinder EXperiment (APEX) telescope located in Chile, at 5100 m above the sea level, the James Clerk Maxwell Telescope (JCMT) at ~ 4100 m in Hawaii, and the IRAM-30 m telescope in Spain, are powerful single-dish telescopes available for observations of line emission towards CSEs of late-type star at submillimeter wavelengths.

The extended and dense CSEs of AGB and post-AGB stars are characterized by low temperatures, typically below 1000 K. As discussed above, the molecular gas content of the CSEs of AGB stars is dominated by H_2, but because of its lack of electric dipole moment, it is not excited throughout the cold CSEs. In contrast, CO is easily excited at the typical temperatures of CSEs within a wide range of densities. The different rotational transitions of CO are excited throughout almost the entire

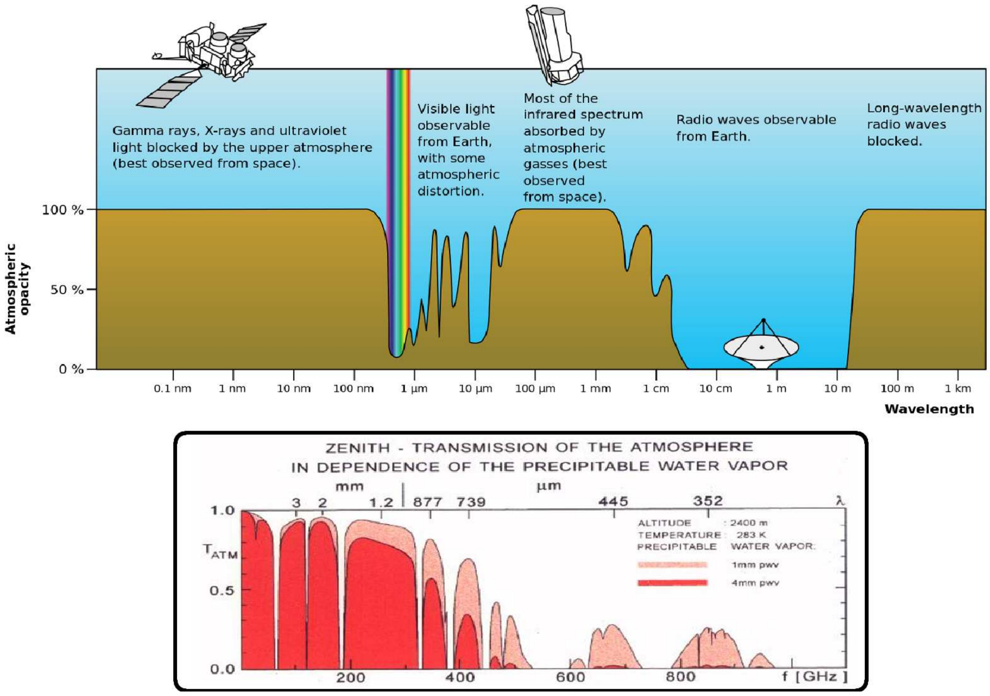

Figure 3.1: *Top* Atmospheric opacity for the entire electromagnetic spectrum. *Bottom* Atmospheric transmision at submillimeter wavelengths for two different values of the PWV for a place located at 2400 m above the sea level. Images adopted from NASA and Arizona Radio Observatory.

CSEs, up to distances where the H_2 shielding and CO self-shielding are not longer efficient. The CO rotational transitions are excited by collisions with H_2 molecules. High energy CO rotational transitions trace regions close to the central star, while the low energy CO rotational transition ($J = 1-0$, $J = 2-1$) trace large-scale regions. In principle, it is possible to trace the column density (number of molecules in a column of a given surface area) of the molecular gas and its kinetic temperature using radio observations of CO line emission. The brightness distribution of different rotational transitions of CO gives information about the gas expansion velocity, mass-loss rate of the central source, and large-scale distribution of the molecular gas. In fact, it has been shown that combining observations of different CO rotational transitions with radiative transfer models of the detected line is one of the most reliable methods to constrain the mass-loss rate of a particular source (e.g Ramstedt et al. 2008). Observations of the brightness temperature distribution are limited by the angular resolution provided by single-dish radio telescopes. The beam width of radio telescopes is given by

$$\theta_b = 50'' \left[\frac{100\ \mathrm{GHz}}{\nu}\right]\left[\frac{15\ \mathrm{m}}{d}\right], \tag{3.1}$$

where d is the diameter of the telescope. Typically, the CSEs of AGB stars are extended sources, but in most of the cases the angular resolution provided by telescopes like JCMT and APEX, for instance, is not enough to resolve the CSEs.

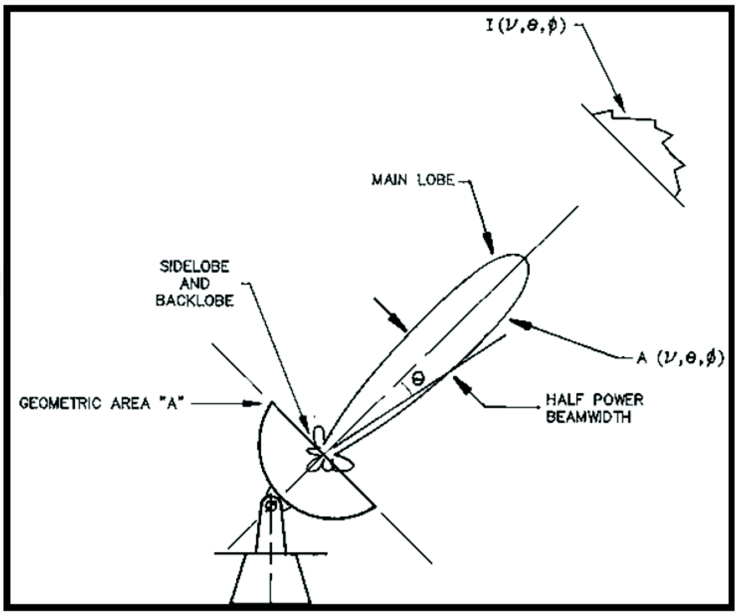

Figure 3.2: Schematic overview of the beam pattern of a radio telescope.

By observing and resolving molecular line emission, for instance CO emission throughout an extended object such as the CSEs of AGB stars, some physical properties of the observed source can be constrained. However, the determination of such properties are restricted by the observation itself, and whether the observed emission is uniform through the telescope beam (extended source) or not (point-like source). The observed flux density is a function of the sensitivity of the telescope and its variation over the telescope beam. If an antenna with normalized response pattern $P_n(\theta, \phi)$ is pointed towards a source with brightness distribution given by $B_\nu(\theta, \phi)$, then the incoming power per unit frequency interval detected by the antenna is given by

$$P_\nu = \frac{A_{eff}}{2} \int_{4\pi} B_\nu(\theta, \phi)\, P_n(\theta, \phi)\, d\Omega, \tag{3.2}$$

where A_{eff} is the effective area of the antenna. The spectral distribution of a source emitting as a black body is given by

$$B_\nu(T) = \frac{2h\nu^3}{c^2} \frac{1}{exp(h\nu/kT) - 1}, \tag{3.3}$$

that in the Rayleigh-Jeans limit ($h\nu \ll kT$) becomes

$$B_\nu(\nu, T) = \frac{2\nu^2}{c^2} kT. \tag{3.4}$$

Therefore, in the radio frequency range the brightness of a source which is considered in thermodynamic equilibrium, is proportional to its thermodynamic temperature, the so called brightness temperature T_B

$$T_B = \frac{c^2}{2\,k\nu^2} B_\nu = \frac{\lambda^2}{2k} B_\nu. \tag{3.5}$$

In radio telescopes, the detected power per unit of frequency interval is compared with the power generated by thermal noise produce by the electronics of the detector. The temperature required to generate a signal with power per unit frequency equal to that of the incoming signal is called antenna temperature. It is relevant to estimate signal-to-noise ratios, but in general, it does not have a physical meaning related to the source. However, in the Rayleigh-Jeans limit the antenna temperature can be written as $P_\nu = kT_A$. Thus, replacing this in Eq. 3.2

$$T_a = \frac{A_{eff}}{2k} \int_{4\pi} B_\nu(\theta, \phi)\, P_n(\theta, \phi)\, d\Omega. \tag{3.6}$$

Then, by combining Eq. 3.5 and Eq. 3.6, and given that the effective area of the antenna is $A_{eff} = \lambda^2/\Delta\Omega_a$, it is possible to write

$$T_a(\theta_0, \phi_0) = \frac{1}{\Delta\Omega_a} \int_{4\pi} T_B(\theta, \phi)\, P_n(\theta - \theta_0, \phi - \phi_0)\, d\Omega, \tag{3.7}$$

where the integral is calculated over the solid angle subtended by the source. Eq. 3.7 can be solved only if the response pattern of the telescope $P_n(\theta, \phi)$ is well known for all the directions covered by the telescope beam. On the other hand, the equation of transfer as a function of the temperature in the Rayleigh-Jeans limit is

$$\frac{dT_B(s)}{d\tau_\nu} = T_{bk}(0) - T(s), \tag{3.8}$$

where $T(s)$ is the temperature of the medium interacting with the radiation of a given background source with temperature T_{bk}. The solution of Eq. 3.8 is

$$T_B = T_{bk}(0)\, e^{-\tau_\nu(s)} + T(1 - e^{-\tau_\nu(s)}). \tag{3.9}$$

Hence, the brightness temperature distribution is a function of the optical depth of the source, and T_B corresponds to its thermodynamic temperature only in the limit of large optical depth, i.e, for optically thick sources. Therefore, in the case of an extended source ($\Delta\Omega_s \gg \Delta\Omega_a$) whose brightness distribution is uniform through the telescope beam, the antenna temperature can be related to the thermodynamic temperature of the source at a location where $\tau \approx 1$ by solving Eq. 3.7, but only if the emission detected is optically thick. As mentioned above, in the case of the CSEs of AGB stars with high mass-loss rates (e.g. $\dot{M} > 10^{-7}$ M$_\odot$ yr^{-1}), the excitation of the CO rotational transitions observable at millimeter and submillimeter wavelengths is mainly due to collisions with H_2. Thus if the velocity distribution of the of the gas is determined by its temperature, the level population of CO can be described by a Boltzmann distribution at the kinetic temperature of the gas if all the molecular levels are thermalized.

A particular rotational transition is thermalized if the number of collisions exciting the upper level is in equilibrium with the radiative transition de-exciting it. In that case, the excitation temperature T_{ex}, defined as the temperature that describes the population ratio between the upper and the lower levels of a particular transition, can be expected to be the kinetic temperature of the gas. However, to constrain the density and temperature distribution from radio observations towards the CSEs of AGB stars is more complicated. The spectral lines observed, whose shapes are in general used as a first diagnostic of the density and temperature distribution of the observed source, are the result of a complex interplay between the stellar radiation field and all the different molecular species and dust particles that the CSEs comprise. Effects such as cooling by line emission, heating by collisions, adiabatic expansion, shocks, clumps, collimated outflows, photodisociation, etc., increase the size of the parameter space needed to solve consistently the equation of transfer, which in turns increase the degeneracy of the results. In Chapter 7 we present the results of simulated radio observations towards synthetic AGB sources. This study is our first approach to the problem of molecular line emission towards asymmetric CSEs of AGB stars whose oblate morphologies can be the result of the onset of collimated outflows.

3.2 Radio interferometry: Overview

Observation of the CSEs of AGB and post-AGB stars aims to unveil the spatial distribution of density and temperature of the gas and dust within large and small spatial scales. For instance, observations of maser emission require high-spatial resolution, lower than tenths of seconds-of-arc accuracy, in order to truly identify the different maser spots and their relative location throughout the CSEs. Such outstanding resolution is provided by radio interferometers; ensemble of pairs of antennae spread around distances from a few tens of meters up to kilometers distances.

The distance between a pair of antennae is called the baseline, and the angular resolution observable by a pair of antennae follow the relation 3.1, but instead of the dish diameter D, it depends of the baseline length B. For an antennae array, the primary beam (the beam width of a single antenna of the array) defines the observable field-of-view. The longest baseline defines the highest angular resolution that the array can discern, while the shortest baseline defines the large scales that the array is able to resolve. The observational technique used by interferometers such as the Australia Telescope Compact Array (ATCA) (Fig. 3.3), the Jansky Very Large Array (JVLA), the Submillimeter Array (SMA), and the Atacama Large (sub-)Millimeter Array (ALMA) is known as Aperture synthesis. For a single-dish radio telescope, its response to the incoming signal is given by the product of the Fourier functions describing the source brightness distribution and the aperture shape, or beam of the antenna. The same principle applies for radio interferometers, but the response to the incoming signal is a function of the separation between each pair of telescopes of the array. In addition, due to the rotation of the Earth, the response of the interferometer is also function of time. This is because baseline length as seen from the point of view of the source changes as the Earth rotates. In the particular case of a two antennae array located in the East-West direction, when a source rises or sets, the separation of the two telescopes

Figure 3.3: Interferometers: The Australia telescope compact array (ATCA) (top left), The JVLA (top right) and ALMA (bottom). Credits: ATNF, NRAO, ALMA(ESO,NAOJ,NRAO), O. Dessibourg.

seen from the source is small, whereas when the source is at its highest position on the sky, the baseline seen from the source is larger. The aperture synthesis technique consist on the cross correlation of the brightness distribution of a source on the plane of the sky $I(x, y)$, and the response of the array as a function of the separation of the antennae measured in a coordinate system with orthogonal axis (u,v), the so called uv-plane. The response of each pair of antennae is a complex function called Visibility, which is related to the sky brightness distribution by the Fourier transform

$$V(u, v) = \iint I(x, y) e^{-2\pi\ i\ (ux+vy)} dxdy. \tag{3.10}$$

The visibility provided for a pair of antennae is then a point on the uv-plane. Due to the Earth rotation, and depending on the period of time tracking the source, the visibility of each pair of antennae corresponds to a set of discrete points forming arcs in the uv-plane. Therefore, a key factor of the aperture synthesis technique is the coverage of the uv-plane. The ideal case is to have an uniform coverage. In such case, the response of the interferometer when all the visibilities measured are synthesized will correspond the response of a single telescope with an aperture size given by the longest baseline. However in practice, the uv-plane is never entirely filled.
The Fourier transform of a single visibility function is a fringe pattern where the distance between two consecutive maxima is determined by the distance between the two antennae. Each pair of antennae of the array provides a visibility function, which is characterized by an amplitude and phase equal to the amplitude and phase of the fringe pattern. Large baselines produce high spatial frequency fringe pattern, while short baselines produce low spatial frequency patterns. In the case of a point-like source, which is basically a source with angular size smaller than the synthesized beam, the fringe pattern observed is essentially the same despite the baseline length. But in the case of sources with angular size larger than the synthesized beam (extended sources) the maxima in the fringe pattern are not longer coincident for different baseline lengths. In other words, a pair of antennas linked by a baseline of length B will be sensitive only to a particular spatial frequency. High spatial frequencies corresponds to small angular scales, and large angular scales correspond to low spatial frequencies. Hence, the inverse Fourier transform of the synthesis of the visibilities for well sampled uv-plane, enables us to retrieve most of the brightness distribution of the observed source, with the consequent improvement on the spatial resolution.

Besides the outstanding spatial resolution that interferometric observations provide, the sensitivity level is also enhanced. The signals detected by a pair of antennae is translate into voltages V_1 and V_2. In the context of the so-called phase-switching technique, the phase of the signal of one of the antennae is periodically reversed. Then, after combining the signals from both antennae, the output signal alternates between $(V_1 + V_2)^2$ and $(V_1 - V_2)^2$. A synchronized device takes the difference between the two outputs, which is $4(V_1 \cdot V_2)$. Hence, the intensity of the measured signal is proportional to the multiplication (correlation) of the original signals averaged over a given time; that is, the total power detected is proportional to the cross-correlation of the two signals, which makes interferometers to be much more sensitive than the single-dish telescopes that comprise it.

Interferometric observations of circumstellar maser emission provide unique data for the study of the spatial distribution of individual maser spots as well as of their spectral features, when individual maser spots are resolved, of course. The sensitivity that can be achieved by interferometric observations leads to the detection of maser spectral features with outstanding spectral resolution, which enable us to determine the polarization state of the spectral features detected with exceptional signal-to-noise ratios. However, a number of effects which are originated either by the propagation of the polarized signal through dense regions between the source and the receiver, or by the instrumentation of the detector itself, can modify the original polarized signal. For sources with angular size comparable with the synthesized beam, the magnitude and position angle of the vector of polarization vary for different spatial scales. Therefore, the synthesized beam might smooth the polarization of the source, which is known as beam depolarization.
As the polarized emission propagates through dense regions permeated by magnetic fields located between the source and the receiver, the position angle of the vector of polarization rotates. This phenomena is known as Faraday rotation. Faraday rotation throughout the CSEs, the interstellar medium and the Earth ionosphere depolarize the detected signal. The Faraday depolarization reduces the intrinsic polarization of the observed source though its effects decreases towards higher frequencies. Those effects related to the instrumentation and the atmosphere are eventually corrected in the calibration stage, before the detected polarized signal is used for science.
Observations of polarized emission are generally performed using either linear or circular polarized feeds on each antenna of the array. These feeds are sensitive to orthogonal linear or circular polarization. In the case of linear polarized feeds, the receivers are named as X and Y, with the X feed aligned along the elevation axis of the telescope beam, and the feed Y rotated 90 degrees. Thus, interferometric observations with full polarization are carried out correlating all the four combinations XX, YY, XY and YX for all baselines of the array.
The response of the receivers of an antenna of the array can be represented by the product of different effects related to the receiver system. Each of such effects are expressed in terms of the Jones matrices. Using the Jones formalism, the response of the antenna i with linear polarized feeds is

$$J_i = G_i D_i P_i, \tag{3.11}$$

where G_i, D_i and P_i are the Jones matrices for the gain, leakage and the parallactic angle, which have the form

$$G_i = \begin{pmatrix} g_{iX} & 0 \\ 0 & g_{iY} \end{pmatrix}, \tag{3.12}$$

$$D_i = \begin{pmatrix} 1 & d_{iX} \\ d_{iY} & 1 \end{pmatrix}, \tag{3.13}$$

$$P_i = \begin{pmatrix} \cos\chi & -\sin\chi \\ \sin\chi & \cos\chi \end{pmatrix}, \tag{3.14}$$

where χ is the measure of the rotation of the feeds seen from the point of view of the source whilst the antenna tracks the source; the parallactic angle, given by

$$\chi = \tan^{-1}\Big(\frac{\cos(l)\sin(h)}{\sin(l)\cos(\delta) - \cos(l)\sin(\delta)\cos(h)}\Big), \tag{3.15}$$

where h is the source hour angle, δ is the source declination, and l is the latitude of the antenna. The response of the interferometer, i.e., the output of the correlation of the visibilities is a function of the outer product of the individual Jones matrices, multiplied by a vector characterizing the detected signal

$$R = (J_i \otimes J_k^*)\ S\ V_s, \tag{3.16}$$

where J_k^* represents the complex conjugate of J_k; V_s is vector of the Stokes visibilities (I_v, Q_v, U_v, V_v) which are the complex visibility for the distribution of the the Stokes parameters over the source, and S is a 4×4 transformation matrix from the Stokes parameters to the polarization coordinates of the antennae, given by

$$S = \frac{1}{2}\begin{pmatrix} 1 & 1 & 0 & 0 \\ 0 & 0 & 1 & j \\ 0 & 0 & 1 & -j \\ -1 & -1 & 0 & 0 \end{pmatrix} \tag{3.17}$$

where $j = \sqrt{-1}$. Thus, in the limit of weakly polarized source, as expected for maser radiation, and nearly perfect feeds, higher order terms involving instrumental and source polarization can be neglected. Hence, the response to the polarized radiation in terms of the Stokes visibilities on baseline $i \rightarrow k$ is

$$R_{XX} = \frac{1}{2} g_{iX} g_{kX}^* (I + Q\cos(2\chi) + U\sin(2\chi)), \tag{3.18}$$

$$R_{XY} = \frac{1}{2} g_{iX} g_{kY}^* ((d_{iX} - d_{kY}^*)I - Q\sin(2\chi) + U\cos(2\chi) + jV), \tag{3.19}$$

$$R_{YX} = \frac{1}{2} g_{iY} g_{kX}^* ((d_{kX}^* - d_{iY})I - Q\sin(2\chi) + U\cos(2\chi) - jV), \tag{3.20}$$

$$R_{YY} = \frac{1}{2} g_{iY} g_{kY}^* (I - Q\cos(2\chi) - U\sin(2\chi)). \tag{3.21}$$

After the correlation, the output signal enter in the calibration stage. It includes the correction of instrumental polarization, the calibration of the polarization angle, where observations of source with known polarization state are used. After calibration, the final step will be to determine the fractional polarization and the angle of polarization associated to the different spectral features. Calibration software like CASA, MIRIAD and AIPS are the most used for calibration and reconstruction of the final image of the source.

CHAPTER 4

Maser Polarization

Once ALMA full polarization capabilities are offered, it will become possible to perform detailed studies of polarized maser emission towards star-forming regions and late-type stars, such as (post-) asymptotic giant branch stars and young planetary nebulae. To derive the magnetic field orientation from maser linear polarization, a number of conditions involving the rate of stimulated emission R, the decay rate of the molecular state Γ*, and the Zeeman frequency* $g\Omega$ *need to be satisfied. We used a radiative transfer code to calculate the fractional linear polarization as a function of the emerging brightness temperature for a number of rotational transition of SiO,* H_2O *and HCN that have been observed to display maser emission at submillimetre wavelengths. We assumed typical magnetic field strengths measured towards galactic star-forming regions and circumstellar envelopes of late-type stars from previous VLBI observations. Since the Landé g-factors have not been reported for the different rotational transitions we modelled, we performed our calculations assuming conservative values of the Zeeman frequency for the different molecular species. Setting a lower limit for the Zeeman frequency that still satisfies the criteria* $g\Omega > R$ *and* $g\Omega > \Gamma$*, we find fractional polarization levels of up to 13%, 14% and 19% for the higher J transitions analysed for SiO,* H_2O *and HCN, respectively, without considering anisotropic pumping or any other non-Zeeman effect. These upper limits were calculated assuming a magnetic field oriented perpendicular to the direction of propagation of the maser radiation. According to our results SiO,* H_2O *and HCN maser emission within the ALMA frequency range can be detected with suitable linear polarization to trace the magnetic field structure towards star-forming regions and late-type stars even if the detected polarization has been enhanced by non-Zeeman effects. The contents of this chapter originally published in the A&A jounal (Pérez-Sánchez and Vlemmings 2013).*

Polarized maser emission has been detected towards the expanding CSE of late-type stars such as (post-) AGB stars and young planetary nebulae (e.g. Alves et al. (2012), Amiri et al. (2012), Leal-Ferreira et al. (2012), Vlemmings, Humphreys and Franco-Hernández (2011), Vlemmings et al. (2006)).

Both single-dish and interferometric observations have revealed that SiO, H_2O, HCN, (OH), among others, can naturally generate polarized maser emission in these enviroments (e.g. Vlemmings et al. (2006), Surcis et al. (2011a), Fish and Reid (2007b), Herpin et al. (2006), Kemball et al. (2009)). In particular, interferometric observations of the masers at radio wavelengths have become a useful tool for studying the magnetic field around late-type stars (e.g. Fish and Reid (2007a), Amiri, Vlemmings and van Langevelde (2010)). At shorter wavelengths, new instruments will enable the study of maser radiation from higher vibrationally-excited rotational transitions. In particular, the Atacama Large Millimeter/submillimeter Array (ALMA) has recently started the first scientific observations. Soon all of its capabilities, including polarimetry, will be available, providing more than an order of magnitude improvement in sensitivity and resolution. In the ALMA frequency range, a number of SiO, H_2O and HCN maser transitions that belong to vibrationally-excited levels up to $v = 3$ can be detected. The population inversion of rotational states belonging to different molecular species, or within different vibrational levels of a particular species, depends on the physical conditions of the emitting regions. By observing the maser polarization at different frequencies towards an extended source, we can hence constrain the magnetic field properties, i.e. field strength and/or direction, throughout large regions within the observed source. According to the Zeeman interpretation, the maser polarization strongly depends on the ratio between the Zeeman frequency ($g\Omega$), the rate of stimulated emission (R), and the rate of the decay of the molecular state (Γ). The Zeeman splitting induced by a magnetic field depends on the molecule's shell structure. For example, since SiO, H_2O and HCN are non-paramagnetic, closed-shell molecules, $g\Omega$ is expected to be less than the intrinsic line width $\Delta\omega$. Maser polarization theory (e.g Western and Watson (1984)) predicts fractional linear polarization (p_L) levels of up to 100% for $J = 1 - 0$ rotational transitions of diatomic molecules. These polarization levels can be reached in the presence of a magnetic field of a few Gauss in, for example, the SiO masing region in CSEs of late-type stars. But in the case of higher rotational transitions (i.e. $J = 2-1$, $J = 3-2$, etc.) theory predicts that unless anisotropic pumping is involved, the fractional linear polarization should decrease as the angular momentum number of the involved state increases. Before the observed maser polarization can be related to an intrinsic magnetic field, it is necessary to evaluate the ratios between the maser parameters R, $g\Omega$ and Γ for each single rotational transition detected with angular momentum higher than $J = 1$. Here, we determine if the polarized maser radiation produced by molecular transitions of SiO, H_2O and HCN in the ALMA frequency range could generate detectable levels of fractional linear polarization, while still satisfying the criteria ($g\Omega > R$ and $g\Omega > \Gamma$) for which the polarization direction is still directly related to the magnetic field. These maser transitions can then be used to infer the magnetic field structure towards SFRs and in the CSEs of (post-) AGB stars. To do this, we have run numerical models adapted from Nedoluha and Watson (1992) to calculate the fractional linear polarization level that can be generated by the interaction of the molecular states of SiO, H_2O and HCN in the ALMA frequency range, with a magnetic field in the masing region.

4.1 Maser polarization theory

Polarized maser radiation provides a unique tool for studying the role of magnetic fields inside high-density enviroments such as star-forming regions and circumstellar envelopes of evolved stars. Although the general maser emission mechanims from astronomical sources have been well understood throughout the past thirty years (e.g. Elitzur (1992), Gray (2012)), the generation and radiative transfer of polarized maser emission have been difficult to deal with. The polarization properties of maser emission strongly depend on the radiative conditions of the region where the maser is being generated (saturated or unsaturated) and on the nature of the molecular species generating the maser emission (paramagnetic or non-paramagnetic) (Watson 2008, Dinh-v-Trung 2009).

Maser-polarized radiation can be produced in both unsaturated and saturated frames. Maser emission is considered to be saturated when the rate for the stimulated emission R overcomes the decay rate of the molecular state involved, Γ. In this case, the growth of the possible polarization modes is determined by the population of the molecular states that can interact with a particular mode of the polarization (Nedoluha and Watson 1990a). Goldreich, Keeley and Kwan (1973) first identified two regimes where polarized emission can be generated in the saturated frame for the molecular rotational transition $J = 1-0$: a) The strong magnetic field strength regime, where the Zeeman frequency $g\Omega \gg R$ and $g\Omega \gg \Gamma$; and b) The intermediate magnetic field strength regime, where $(g\Omega)^2/\Gamma \gg R \gg g\Omega$. Western and Watson (1984), Deguchi and Watson (1990) and Nedoluha and Watson (1990a) extended the treatment of Goldreich, Keeley and Kwan (1973), solving the radiative transfer equations for polarized radiation as a function of the emerging intensity R/Γ, i.e. as a function of the saturation level. They considered linear, non-paramagnetic molecules, including the rotational transitions $J = 2-1$ and $J = 3-2$. Nedoluha and Watson (1990a) have shown that in the presence of a plausible magnetic field and without differences in the population of the magnetic substates involved in the maser emission, the upper limit of fractional linear polarization p_L that maser transitions other than $J = 1-0$ can achieve is 33%. The fractional linear polarization decreases for transitions with higher angular momentum, and is a function of the angle θ between the magnetic field ($\vec{B}$) and the direction of the maser radiation ($\vec{k}$).

Molecular states with angular momentum higher than $J = 1-0$ reach their maximum p_L value when the magnetic field lines are perpendicular to the direction of the propagation of the maser radiation, and have $p_L = 0$ when θ has the critical value $\theta_{cr} \sim 55°$, also known as the van Vleck angle, and when $\theta = 0°$.

The angle ϕ between the polarization vector and the plane $\vec{k} \cdot \vec{B}$ also varies as a function of the ratio $g\Omega/R$. For a fixed θ, the vector of polarization should be either perpendicular or parallel to the $\vec{k} \cdot \vec{B}$ plane if the condition $g\Omega \gg R$ is satisfied. On the other hand, for higher values of R, but still in the intermediate-strength magnetic field regime, the vector of polarization is already rotated away from the $\vec{k} \cdot \vec{B}$ plane, i.e. if $R > g\Omega$ the vector of polarization is neither parallel nor perpendicular to the plane $\vec{k} \cdot \vec{B}$. In this context, the van Vleck angle is the limit for θ where the polarization vector changes from being parallel to be perpendicular to the $\vec{k} \cdot \vec{B}$ plane. Therefore, as long as the conditions $g\Omega > R$ and

$g\Omega > \Gamma$ are satisfied, the information about the morphology of the magnetic field can be extracted from the polarization vector.

Observationally, fractional linear polarization of up to 100% for $J = 1 - 0$ SiO maser transitions (Amiri et al. 2012) and values higher than 33% for SiO molecular transitions involving higher angular momentum states (e.g Vlemmings, Humphreys and Franco-Hernández 2011) have been detected. Anisotropic pumping seems to be a possible process to explain such high p_L levels (Nedoluha and Watson 1990a). It can be produced by differences in the angular distribution of the radiation field involved in the population inversion process. In the absence of a magnetic field, anisotropic pumping could produce highly linearly polarized emission. In contrast to the effect of a magnetic field alone in the maser region, the fractional linear polarization can increase with the angular momentum due to an anisotropic population of the involved magnetic substates. Nevertheless, even considering that the linear polarization has been enhanced by anisotropic pumping, if $g\Omega > R$ and $g\Omega > \Gamma$ for the detected line, the magnetic field structure can still be traced directly from the polarization vector, because the magnetic field is the dominant axis of symmetry (Watson 2002). The study of magnetic fields from maser linear polarization thus depends critically on an analysis of the Zeeman frequency $g\Omega$ and the stimulated emission rate R.

4.2 Maser emission in the ALMA frequency range

4.2.1 SiO

Strong SiO emission arises from the innermost regions of the CSE of late-type stars, and a number of maser transitions have been detected in vibrational levels of up to $\upsilon = 4$, with rotational transitions as high as $J = 8 - 7$ (Menten et al. (2006), Humphreys (2007) and references therein). The most common SiO maser transitions detected are the two lowest rotational transitions of the $\upsilon = 1$ vibrational level, peaking around 43 GHz and 86 GHz (e.g. Barvainis and Predmore 1985). The list of SiO rotational transitions, including the isotopologues ^{29}SiO and ^{30}SiO, which can be observed as maser emission in the ALMA frequency range, are listed in Table 4.1 (Müller et al. 2001).

Polarized SiO maser emission has been detected towards oxygen-rich (post-)AGB stars. Barvainis and Predmore (1985) reported the detection of strong polarized emission in the rotational transitions $J = 1-0$ and $J = 2 - 1$, of both $\upsilon = 1$ and $\upsilon = 2$ vibrational levels.

Fractional linear polarization levels between 15% and 40% are commonly detected, though levels approaching 100% have also been reported (e.g. Barvainis and Predmore (1985), Kemball and Diamond (1997), Amiri et al. (2012)). Shinnaga et al. (2004) and Vlemmings, Humphreys and Franco-Hernández (2011) reported the detection of high fractional linear polarization levels ($p_L \geq 40\%$) of the $J = 5 - 4$ rotational transitions of the $\upsilon = 1$ vibrational level, towards the supergiant VX Sgr. Such high polarization levels cannot only be explained by the presence of a large-scale magnetic field permeating the masing region, but need to be enhanced by non-Zeeman effects.

4.2.2 H_2O

At submillimetre wavelengths a number of molecular transitions of H_2O have been detected displaying high flux density values and narrow line shapes characteristic of maser emission lines (Waters et al. (1980), Menten et al. (1990), Yates and Cohen (1996)). The submillimetre water maser transitions within the ground-vibrational state have been detected towards CSEs of O-rich late-type stars as well as from low- and high-mass SFRs, either tracing shocked regions or arising from the steadily expanding CSEs (e.g. Ivison, Yates and Hall (1998), Melnick et al. (1993)). The different water transitions observable in the ALMA frequency range within the ground-vibrational state and the $v_2 = 1$ bending mode are listed in the Table 4.2.The rotational maser transitions within the vibrationally excited level $v_2 = 1$ are thought to arise from regions where the physical conditions are similar to those that invert the level population of the SiO rotational transitions (Alcolea and Menten 1993).
In contrast to the case of SiO, there are not many references in the literature reporting the detection of H_2O maser polarized radiation in the ALMA frequency range. To date, only (Harwit et al. 2010) have succeeded in measuring linear polarization of water maser radiation at 620.7 GHz. Unfortunately, the very low atmospheric transmission around 621 GHz prevents the detection of this maser transition from ground-based telescopes.
The excitation conditions of the submillimetre water masers seem to be a subset of the broad excitation conditions generating the 22.2 GHz maser line (Neufeld and Melnick (1991), Humphreys (2007)). The dominating pumping process depends on the characteristics of the region where the maser emission arises; either from post-shock regions, where the inversion of the population of the molecular states is mainly collisional, or from the steadily expanding CSEs, where the pumping process is mainly thought to be caused by infrared photons of warm dust emission. Observations of 22.2 GHz H_2O maser polarized emission have been used to probe the magnetic field strengths within the steadily expanding CSEs of AGB and supergiant stars (e.g. Vlemmings, van Langevelde and Diamond 2005). In addition, polarized water maser emission has been detected towards the high-velocity outflows of the so-called water-fountains, with spectral features displaying high levels of fractional linear polarization ($p_L > 5\%$) and unusually broad velocity ranges. These observations have probed magnetically collimated "jets" that appear during the post-AGB phase, and are thought to be the precursors of bipolar (multipolar) planetary nebulae (Vlemmings, Diamond and Imai (2006), Pérez-Sánchez, Vlemmings and Chapman (2011)).

4.2.3 HCN

Strong HCN maser emission has also been detected towards the CSEs of several carbon-rich (C-rich) AGB stars in the ALMA frequency range (e.g. Bieging (2001), Schilke and Menten (2003)). Table 4.2 summarizes the different HCN transitions that can be observed as maser emission in the submillimetre wavelength regime (Müller et al. 2001). Linearly polarized HCN maser emission of the 89.087 GHz, $J = 1 - 0$ transition, within the $(0,2^0,0)$ vibrationally excited state, has been detected at approximately

20% towards the innermost region of the CSE of the C-rich star CIT 6 (Goldsmith et al. 1988). The masing region is thought to be located between the photosphere and the inner radius of the expanding envelope, similar to the SiO masers in the oxygen-rich late-type stars. Anisotropies in the population inversion of the masing transitions might affect the fractional linear polarization, but more observations are needed to determine the exact cause of the polarization.

4.3 Model results

Maser emission can be affected by several non-Zeeman processes that can enhance or even produce linear and/or circular polarization, such as anisotropic pumping or the change of the quantization axis along the amplification path (Wiebe and Watson 1998). Therefore, it is necessary to solve the radiative transfer equation for a particular rotational transition to learn whether the polarization detected can be correlated to a large-scale magnetic field permeating the masing region. Furthermore, it is necessary to determine if the involved rotational transition can produce appreciable levels of p_L when the quantization axis is defined by the magnetic field direction, i.e. when the Zeeman frequency $g\Omega$ is higher than the stimulated emission rate R. The inequalities $g\Omega > \Gamma$ and $g\Omega > R$ allow us to analyse the polarization observed in terms of the ordinary population of the magnetic substates (Watson 2008). In the case of SiO the decay rate Γ listed in Table 4.3 corresponds to the rate for the radiative decay from the first vibrationally excited state to the ground-vibrational state (Nedoluha and Watson 1990a). For water, this value is roughly the inverse lifetime for infrared transitions of the 22 GHz, H_2O maser transition (Nedoluha and Watson 1990b). In the case of HCN, this value corresponds to the decay rate associated to a pumping process dominated by infrared radiation (Goldreich and Kwan 1974).

Considering the Γ and $g\Omega$ values in Table 4.3, it is clear that for the case of interest the criterium $g\Omega > \Gamma$ is satisfied. To evaluate whether the stimulated emission rate satisfies the condition $g\Omega > R$ for a particular transition when p_L is sufficiently large to be detected, we have used a radiative transfer code adapted from Nedoluha and Watson (1992) and Vlemmings (2002). The stimulated emission rate R is given by

$$R \approx \frac{AkT_b\Delta\Omega}{4\pi h\nu}, \tag{4.1}$$

where A is the Einstein coefficient of the involved transition, which is calculated and listed for most of the transitions in Tables 4.1 and 4.2; k and h are the Boltzmann and Planck constant, ν is the maser frequency, T_b is the brightness temperature and $\Delta\Omega$ is the relation between the real angular size of the of the masing cloud and the observed angular size.

Although the quantities T_b and $\Delta\Omega$ are related to the observed intensity of the maser, it is a difficult task to constrain their value directly from observations. Brightness temperatures of up to $\sim 10^{15}$ K have been measured for water masers in SFRs, whereas estimated values for $\Delta\Omega$ are $\sim 10^{-1} - 10^{-2}$ sr for water masers detected towards the CSEs of late-type stars (Richards, Elitzur and Yates (2011), Vlemmings

Table 4.1: Spontaneous emission coefficient and frequencies of the detected SiO maser transitions in the ALMA frequency range

^{28}SiO					^{29}SiO				
v	$J_u - J_d$	Freq (GHz)	A (s^{-1})	ALMA band	v	$J_u - J_d$	Freq (GHz)	A (s^{-1})	ALMA band
0	1 - 0	43.42386	3.036×10^{-6}	1		1 - 0	42.87992	2.114×10^{-8}	1
	2 - 1	86.84699	2.915×10^{-5}	2		2 - 1	85.75906	2.460×10^{-7}	2
	1 - 0	43.12208	3.011×10^{-6}	1	0	3 - 2	128.63685	9.696×10^{-7}	4
	2 - 1	86.24344	2.891×10^{-5}	2		4 - 3	171.51255	2.532×10^{-6}	5
	3 - 2	129.36326	1.045×10^{-4}	4		5 - 4	214.38548	5.334×10^{-6}	6
1	4 - 3	172.48102	2.569×10^{-4}	5		6 - 5	257.25493	9.869×10^{-6}	6
	5 - 4	215.59592	5.131×10^{-4}	6		3 - 2	127.74849	3.350×10^{-4}	4
	6 - 5	258.70725	9.003×10^{-4}	6	1	4 - 3	170.32807	8.745×10^{-4}	5
	7 - 6	301.81430	1.445×10^{-3}	7		6 - 5	255.47849	3.407×10^{-3}	6
	1 - 0	42.82059	2.986×10^{-6}	1	2	6 - 5	253.70317	1.11139	6
	2 - 1	85.64046	2.866×10^{-5}	3					
	3 - 2	128.45881	1.036×10^{-4}	4	^{30}SiO				
2	4 - 3	171.27507	2.547×10^{-4}	5		1 - 0	42.373426	2.016×10^{-8}	1
	5 - 4	214.08848	5.088×10^{-4}	6	0	2 - 1	84.746170	2.346×10^{-7}	2
	6 - 5	256.89831	8.927×10^{-4}	6		5 - 4	211.853473	5.081×10^{-6}	6
	7 - 6	299.70386	1.433×10^{-3}	7	1	4 - 3	168.323352	8.054×10^{-4}	5
	1 - 0	42.51938	2.951×10^{-6}	1	2	4 - 3	167.160563	2.542×10^{-1}	5
3	3 - 2	127.55521	1.027×10^{-4}	4					
	4 - 3	170.07057	2.525×10^{-4}	5					
	5 - 4	212.58248	5.044×10^{-4}	6					
4	5 - 4	211.07784	4.986×10^{-4}	6					

Table 4.2: Einstein coefficient and frequencies of the detected H_2O and HCN maser transitions at submillimetre wavelengths.

H_2O				HCN			
$J_u - J_d$	Freq (GHz)	A (s^{-1})	ALMA band	$J_u - J_d$	Freq (GHz)	A (s^{-1})	ALMA band
3_{13} - 2_{20}	183.31012	3.629×10^{-6}	5	1 - 0	88.631602	1.771×10^{-7}	2/3
10_{29} - 9_{36}	321.22564	6.348×10^{-6}	7	$v_2 = 2^0$			
5_{15} - 4_{22}	325.15292	1.166×10^{-5}	7	1 - 0	89.0877	1.483×10^{-4}	2/3
17_{413} - 16_{710}	354.8089	1.096×10^{-5}	7	2 - 1	177.2387	4.578×10^{-5}	5
7_{53} - 6_{60}	437.34667	2.212×10^{-5}	8	$v_2 = 1^{1_c}$			
6_{43} - 5_{50}	439.15081	2.857×10^{-5}	8	3 - 2	267.1993	2.262×10^{-4}	6
6_{42} - 5_{51}	470.88895	3.534×10^{-5}	8	4 - 3	354.4605	6.122×10^{-4}	7
$v_2 = 1$				$v_2 = 4$			
4_{40} - 5_{33}	96.26116	4.719×10^{-7}	3	9 - 8	804.7509	-	10
5_{50} - 6_{43}	232.68670	4.770×10^{-6}	6	$v_1 = 1^1 \rightarrow v_2 = 4^0$			
6_{61} - 7_{52}	293.6645	-	6	10 - 9	890.761	-	10
1_{10} - 1_{01}	658.00655	5.568×10^{-3}	9				

Table 4.3: Fixed parameter values assumed in our numerical models.

Molecule	g	Γ (s^{-1})	$g\Omega_{1G}$ (s^{-1})	B (G)	$\Delta\Omega$ (sr)
SiO	0.155	5	1480.96	1	10^{-2}
H_2O	0.65	1	6226.22	0.05	10^{-2}
HCN	0.098	1	957.8	1	10^{-2}

and van Langevelde (2005)), and in some cases $\Delta\Omega \sim 10^{-5}$ sr for the masers detected towards SFRs (Nedoluha and Watson 1991).
The fractional linear polarization increases with $T_b\Delta\Omega$ in the presence of a magnetic field as long as $\theta \neq \theta_{cr}$. Since R increases faster than p_L when $T_b\Delta\Omega$ increases, the polarization vector of linearly polarized maser radiation detected with high brightness temperature does not necessarily satisfy the criterium $g\Omega > R$, and thus cannot always be directly correlated with the direction of the magnetic field lines, unless the emitted radiation has a high degree of beaming. On the other hand, low brightness temperatures might result in very low or undetectable values of fractional linear polarization. Furthermore, the value of $T_b\Delta\Omega$ scales with the ratio R/Γ, and higher values of the molecular decay rate Γ imply a lower level of fractional linear polarization for the same $T_b\Delta\Omega$ value. This reflects the dependence of the fractional linear polarization level of a particular rotational transition on the saturation level of the maser radiation.
The Zeeman frequency $g\Omega$ determines the energy-splitting of the magnetic sub-levels. In a masing region permeated by a constant magnetic field parallel to the z-axis of the coordinate system, the energy-shifting of the magnetic sub-levels is given by $\hbar g\Omega m/2 = g\mu_N Bm$, where μ_N and m are the nuclear magneton and the quantum number of the magnetic substate (Nedoluha and Watson 1990a). Hence the values for $g\Omega$ can be estimated using the relation

$$g\Omega = \frac{2g\mu_N}{\hbar}\frac{B[\mathrm{G}]}{1\times10^4}, \tag{4.2}$$

where the factor 1×10^4 originates from the conversion between the units of Tesla and Gauss. In general, the molecular Landé factor (g) is different for each magnetic sub-level. The data in the literature are very limited, and there are no reported g-factor values for all the different rotational transitions of HCN nor H_2O. The Landé g-factor for SiO has minor differences (less than 1%) for the $v = 0, v = 1$ and $v = 2$ vibrational transitions (Landolt-Börnstein 1982). The assumed g-factors for the different molecules are listed in Table 4.3. In the case of H_2O, Nedoluha and Watson (1992) calculated the $g\Omega$ values considering hyperfine splitting for the 6_{16} and 5_{23} rotational states of water. Nevertheless, in the present case, we have assume the lower limit suggested for g as it would be without hyperfine splitting (Kukolich 1969), to calculate $g\Omega$ for the different H_2O rotational transitions that we modelled. For HCN we assumed the lower g factor value reported for the $(0,1^{1^c},0)$ vibrational state, which corresponds to a magnetic field parallel to the molecular symmetry axis (Goldsmith et al. (1988) and references therein). Because for closed-shell, non-paramagnetic molecules the response to a magnetic field is weak, we consider the g-factor values listed in Table 4.3 as a conservative choice to constrain a minimum value for $g\Omega$ for the different molecular species. The $g\Omega$ values presented in Table 4.3 correspond to B= 1 G in Equation 4.2, and can be scaled according to magnetic field strengths reported for the different masing regions in both SFRs and CSEs of (post-)AGB stars.
Single-dish observations have revealed average magnetic field strengths of $\sim$ 3.5 G in the SiO maser region, whereas for H_2O the measured values range between 100−300 mG for the CSEs of AGB and supergiant stars, and between 15−150 mG at densities of $n_{H_2} = 10^8 - 10^{11}$ cm^{-3} in SFRs. For our

Table 4.4: Model results: Values of p_L assuming $\theta = 90^o$ and $g\Omega = 10R$ for rotational transitions of the $\upsilon = 1$ vibrational state of SiO and the ground-vibrational level of H_2O. For HCN, the $J = 1-0$ belongs to the vibrationally excited $\upsilon_2 = 2^o$ state, whereas the higher J transitions listed are from the $\upsilon_2 = 1^{1_c}$ vibrationally excited level

SiO		H_2O		HCN	
$J_u - J_d$	p_L	$J_u - J_d$	p_L	$J_u - J_d$	p_L
1−0	~0.32	3_{13} - 2_{20}	~0.19	1−0	~0.33
2−1	~0.23	5_{15} - 4_{22}	~0.16	2−1	~0.27
3−2	~0.18	6_{43} - 5_{50}	~0.15	3−2	~0.22
4−3	~0.15			4−3	~0.19
5−4	~0.14				
6−5	~0.13				

models we assumed the values of the magnetic field strength listed in Table 4.3. This allows us to analyse our results as a function of the minimum $g\Omega$ values for the three molecular species modelled. Thus, using Equation 4.2 for the corresponding magnetic field in Table 4.3, we calculate the $g\Omega$ in order to determine whether the inequality $g\Omega > R$ is satisfied or not.

4.4 Analysis

4.4.1 SiO maser

We present the results of our models for the SiO rotational transitions $J = 5-4$ and $J = 2-1$ of the $\upsilon = 1$ vibrational state in Figure 4.1. The results are for four different θ values and the vertical line corresponds to a $T_b\Delta\Omega$ where $g\Omega = 10R$. The ideal case of $\theta = 90^o$ determines the maximum fractional linear polarization value when a magnetic field permeates the masing region. The maximum fractional linear polarization for rotational transitions of the first SiO vibrationally excited state are listed in Table 4.4. These upper limits were established using the corresponding $g\Omega$ value listed in Table 4.3 for each molecular species, and subsequently finding the $T_b\Delta\Omega$ values where $g\Omega = 10R$. According to our results, it is possible to generate p_L values of up to 13% for the $J = 5-4$ rotational transition, and of up to 23% for the $J = 2-1$ rotational transition without consideration of non-Zeeman effects (Figure 4.1), while the much higher values of p_L detected for the SiO masers require anisotropic pumping.
Therefore, although anisotropic pumping has a strong impact on the fractional linear polarization level, submillimetre SiO maser features observed with brightness temperatures $< 10^9 - 10^{10}$ K fulfil $g\Omega > R$ and could in principle be used to trace the structure of the magnetic field permeating the SiO masing region.

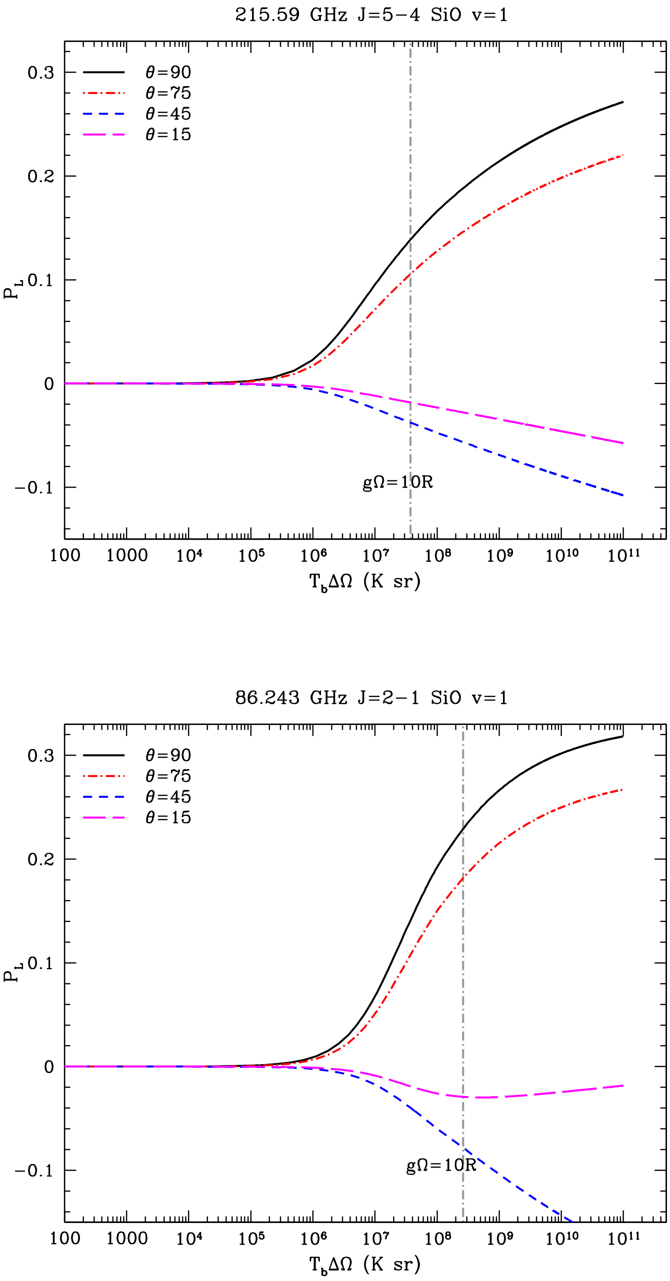

Figure 4.1: Fractional linear polarization as a function of $T_b\Delta\Omega$ for the 215 GHz, $J = 5-4$ (top), and the 86.2 GHz, $J = 2-1$ (bottom) SiO rotational transitions within the $v = 1$ vibrational level for four values of the angle between the magnetic field lines and the direction of propagation of the maser radition, θ, using the parameters listed in table 4.3 for SiO. Positive and negative p_L values mean that the vector of polarization is either perpendicular or parallel the magnetic field lines projected on the plane of the sky. The vertical line sets the $T_b\Delta\Omega$ value such that $g\Omega = 10R$.

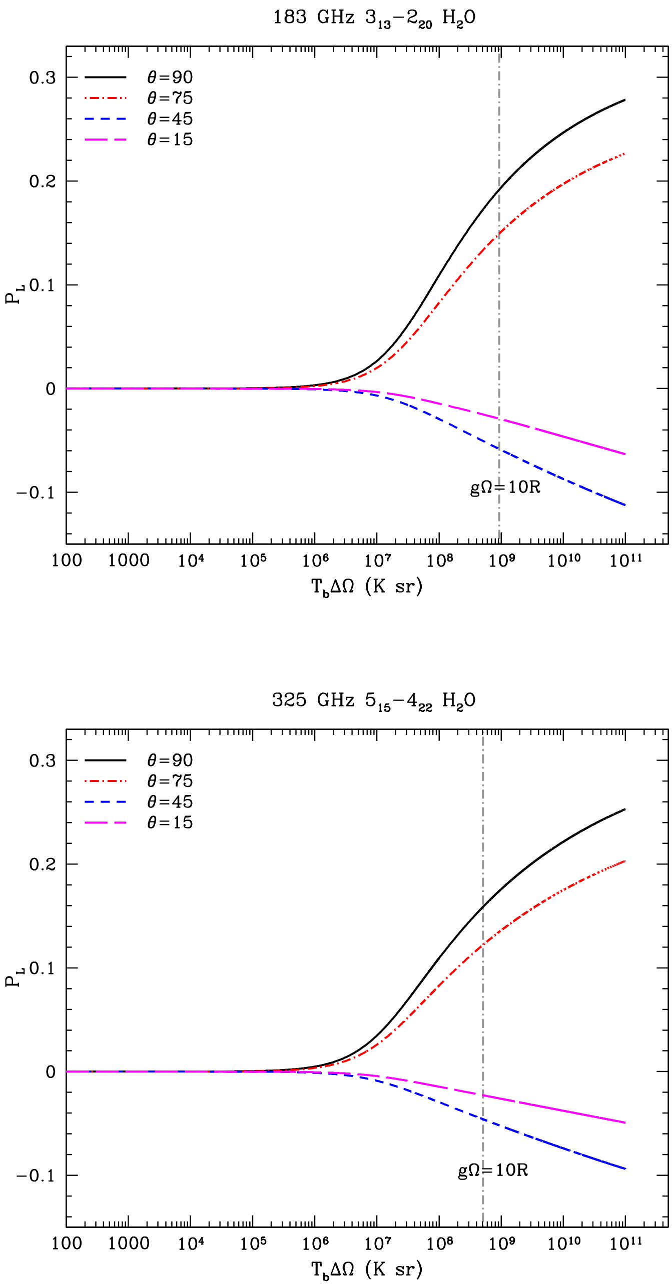

Figure 4.2: Fractional linear polarization as a function of $T_b\Delta\Omega$ for the 183 GHz, $3_{13}-2_{20}$ (top), and the 325 GHz, $5_{15}-4_{22}$ (bottom) H_2O rotational transitions, both within the ground-vibrational level, for four values of the angle between the magnetic field lines and the direction of propagation of the maser radiation, θ. We considered the magnetic field strength and decay rate listed in table 4.3 for H_2O. Positive and negative p_L values mean that the vector of polarization is either perpendicular or parallel the magnetic field lines projected on the plane of the sky. The vertical line sets the $T_b\Delta\Omega$ value such that $g\Omega = 10R$.

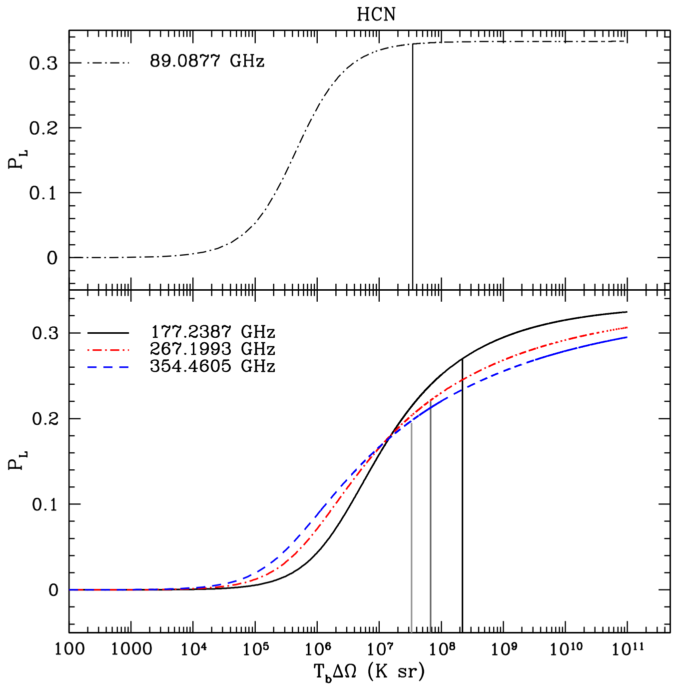

Figure 4.3: Fractional linear polarization as a function of $T_b\Delta\Omega$ for $J = 1-0$, $\upsilon_1 = 2^0$ rotational transition (top), and three HCN rotational transitions of the vibrationally excited state $\upsilon_1 = 1^{1_c}$ (bottom), assuming a magnetic field oriented perpendicular to the direction of propagation of the maser radiation. We considered the magnetic field strength and decay rate listed in table 4.3 for HCN. Under these assumptions, the vertical lines set the maximum linear polarization that the different maser lines can reach satisfying the condition $g\Omega = 10R$.

4.4.2 H_2O maser

To determine the level of fractional linear polarization that water maser transitions can reach when the masing region is permeated by a large-scale magnetic field, we ran numerical models of the rotational transitions within the ground-vibrational state, using the assumptions described in section 4.4.1, together with the corresponding parameters in table 4.3. The results are presented in Table 4.4. In Fig. 4.2 we present the results for the 183 GHz and 325 GHz lines for four different θ values. Our results suggest upper limits for fractional linear polarization of up to 19% and 16% for the 183 GHz and 325 GHz lines, respectively. Therefore, considering the values we assumed for the input parameters listed in Table 4.3, maser features with 10^8 K< T_b < 10^{11} K can produce observable fractional linear polarization levels that can be used to determine the magnetic field morphology. However, if T_b is larger, the observed polarization direction will be rotated away from the projected magnetic field direction on the plane of the sky.

4.4.3 HCN maser

In Table 4.4 we present our results for the maximum fractional linear polarization that the $\upsilon_2 = 2^0$, $J = 1-0$ rotational transition and higher J transitions within the $\upsilon_2 = 1^{1_c}$ vibrational state can produce.

Table 4.5: Sensitivity values at the different maser frequencies of SiO, H_2O and HCN within the ALMA frequency range. The σ listed corresponds to the sensitivity achieved after 1h of on-source time, with 0.1 km/s for a source that reaches a maximum elevation of 59°.

SiO		H_2O		HCN	
υ (GHz)	σ (mJy)	υ (GHz)	σ (mJy)	υ (GHz)	σ (mJy)
86.243	4.58	183.310	38.37	89.0877	4.49
129.363	4.32	325.153	39.58	177.238	4.97
172.481	4.74	439.151	59.25	267.199	4.12
215.596	3.63			354.461	4.99
258.707	4.76				

In Figure 4.3 we show our results assuming a magnetic field oriented perpedicular to the direction of propagation of the maser radiation, and the parameters listed in table 4.3 for HCN. Fractional linear polarization of up to $\sim$ 33% can be generated in the case of the $J = 1 - 0$ rotational transition for $g\Omega = 10R$. This value decreases for rotational transitions with higher J values, as expected. The values of $T_b\Omega$ scale with R/Γ, and consequently, lower Γ values will increase the fractional polarization level that a particular rotational transition can reach while still satisfying $g\Omega > R$. Nevertheless, according to our results, HCN maser emission towards C-rich AGB stars can be generated with high fractional polarization values within the $g\Omega > R$ regime. Thus, the vector of polarization detected from HCN maser observations could be used to probe the magnetic field structure around C-rich AGB stars, even if the level of polarization has been enhanced by non-Zeeman effects.

4.5 Observing maser polarization with ALMA

The temperature and density conditions that favour the population inversion of different masing molecules in SFRs and CSEs of (post-) AGB stars are not the same. Most problably these conditions also differ for different rotational transitions. Therefore, detecting polarized maser emission from multiple rotational transitions and from multiple molecular species with ALMA will enable us to trace the magnetic field structure throughout extended regions around those sources. The accuracy of the ALMA polarimetry will allow us to detect polarized emission of 0.1 % of the detected Stokes I. Therefore, fractional linear polarization can be detected in short observations with very good signal-to-noise ratios. To probe whether the measured polarization of a maser traces the magnetic field permeating the masing region, it is necessary to calculate the brightness temperature of the spectral feature and evaluate if the product $T_b\Delta\Omega$ satisfies the inequality $g\Omega > R$ for the observed emission. For detected spectral features it is possible to constrain T_b by considering the equation

$$\frac{T_b}{[\mathrm{K}]} = \frac{S(\upsilon)}{[\mathrm{Jy}]}\Big(\frac{\Sigma^2}{[\mathrm{mas}^2]}\Big)^{-1}\zeta_\upsilon, \tag{4.3}$$

where $S(\upsilon)$ is the detected flux density, Σ is the maser angular size and ζ_υ is a constant factor that includes a proportionality factor obtained for a Gaussian shape (Burns, Owen and Rudnick 1979). It scales with frequency according to the relation

$$\zeta_\upsilon = 6.1305 \times 10^{11} \left(\frac{\upsilon}{\mathrm{GHz}}\right)^{-2} \frac{\mathrm{mas}^2}{\mathrm{Jy}} \mathrm{K}. \tag{4.4}$$

We calculated the rms value at the different maser frequencies that we modelled using the ALMA sensitivity calculator for an array of 50 12-m antennas. The results are presented in Table 4.5 and correspond to observations of 1 h of on-source time with 0.1 km/s of spectral resolution. To estimate the brightness temperature from observations that do not resolve individual features, it is necessary to assume a value for the size of the masing region generating the spectral feature. VLBI studies have revealed masers to be very compact spots with typical sizes of 1 AU. Based on observed peak-flux density values for maser emission of SiO, H_2O and HCN, assuming a size of 1 mas, i.e. a source distance of 1 kpc, we here give a few examples of potential ALMA observations of maser polarization.

SiO masers: SiO maser emission has been reported displaying flux density values between 7.4 Jy and 64 Jy (Shinnaga et al. 2004) for the $\upsilon = 1$, $J = 5-4$ rotational transition. Moreover, Barvainis and Predmore (1985) reported flux density values between 210 Jy and 625 Jy for the SiO $J = 2-1$ rotational transition of the same vibrationally excited state. As an example, we investigate the detection of a maser spectral feature with a peak-flux density of 10 Jy of the SiO $J = 5-4$ ($\upsilon = 1$) rotational transition. For these values, Equation 4.3 gives $T_b = 1.32 \times 10^8$ K. Comparing this with the $T_b\Delta\Omega$ value, which corresponds to the limit of $g\Omega = 10R$ (Figure 4.1), maser emission with beaming angles $\Delta\Omega < 2.84 \times 10^{-1}$ sr will have a linear polarization that can be used to trace the magnetic field direction. But usually SiO maser spectra exhibit blended components. If this is the case, the flux density observed corresponds to a number of maser spots with similar line-of-sight velocities increasing the observed $S(\upsilon)$. Therefore, the brightness temperature derived using Equation 4.3 could be overestimated, but still could be used to set an upper limit value for T_b. To reach the regime where $g\Omega > R$, it is necessary to associate a $\Delta\Omega$ value to the brightness temperature derived from the $S(\upsilon)$ of the blended components. Hence, since individual maser spectral features might have lower T_b than the blended feature which contains it, even unbeamed maser radiation could still place the linear polarization detected within the regime where $g\Omega > R$ is satisfied.
Finally, according to the ALMA sensitivity calculator, a 5σ detection of 1% of fractional linear polarization of SiO maser emission with low peak-flux densities (few tens of Jy/beam) requires short on-source observation time ($t < 1$ h).

H_2O masers: Submillimetre H_2O lines have been detected with flux densities from a few tens to several thousands of Jy. For the minimun peak-flux density (243 Jy/beam) reported for the 183 GHz by (van Kempen, Wilner and Gurwell 2009), the brightness temperature we obtain using Equation 4.3 is

$T_b = 4.43 \times 10^9$ K. Hence, H_2O maser emission detected with beaming solid angles $\Delta\Omega \geq 1.6 \times 10^{-3}$ sr can generate fractional linear polarization levels higher than 1% (Figure 4.2), satisfying the condition $g\Omega > R$. The 1% of linear polarization level of the weakest 183 GHz maser feature detected by (van Kempen, Wilner and Gurwell 2009) can be easily detected in very short integration times. Unfortunately, many H_2O maser lines are affected by the atmospheric PWV. For maser spectral features with peak-flux densities of the order of 20 Jy/beam at 439.151 GHz, for instance, a 3σ detection of 1 % will require $\sim$ 1 h of on-source observation time.

HCN masers: HCN $J = 1 - 0$, ($v_2 = 2^0$) maser emission at 89.0877 GHz has been detected with fractional linear polarization of 20% for a spectral feature with flux density of 38 Jy (Goldsmith et al. 1988). Furthermore, Lucas and Cernicharo (1989) reported the detection of HCN $v_2 = 1^{1c}$ maser emission with a peak-flux density $\sim$ 400 Jy at 177 GHz. Schilke, Mehringer and Menten (2000) reported the detection of the vibrationally excited HCN (04^00) $J = 9 - 8$ maser line near 805 GHz with a flux density of $\sim$1500 Jy.
For emission reported by Goldsmith et al. (1988), assuming a magnetic field perpendicular to the propagation of the maser radiation, 20% of fractional linear polarization corresponds to $T_b\Delta\Omega = 7.65 \times 10^5$ K sr (Figure 4.3, top), which places the polarization detected in the regime where $g\Omega > R$. On the other hand, considering a spectral feature of $S(v) = 38$ Jy, Equation 4.3 gives $T_b = 2.94 \times 10^9$ K, implying a beaming angle of 2.6×10^{-4} sr, assuming a maser of 1 mas. A beaming angle $\Delta\Omega \sim 10^{-2}$ sr is needed for this maser to satisfy $g\Omega \geq 10R$ and be a realiable tracer of the magnetic field within the masing region. However, if the emission consists of a contribution from multiple maser spots, the brightness temperature of the spectral feature will be overestimated, as discussed previously for blended SiO maser lines. Finally, as in the case of SiO maser emission, 1 % of linear polarization could be observed with very low rms values in short on-source observation times (Table 4.5).

4.6 Conclusions

We have run numerical models to calculate the fractional linear polarization p_L of maser emission generated by the interaction of a magnetic field with the different rotational transitions of SiO, H_2O and HCN within the ALMA frequency range. The fractional linear polarization was calculated as a function of $T_b\Delta\Omega$, a quantity that can be related to the stimulated emission rate R of the involved transition. Considering both the minimun value of the Landé g-factor for each molecular species and a suitable magnetic field strength for the different masing regions, we found the maximum p_L that the analysed rotational transitions can reach while satisfying both conditions $g\Omega > R$ and $g\Omega > \Gamma$. Meeting these criteria allow us to use the detected vector of polarization as a tracer of the magnetic field in the masing region, even if the polarization observed has been affected by non-Zeeman effects.
According to our results, SiO, H_2O and HCN submillimetre maser emission can be detected with observable fractional polarization levels (> 1%) in the regime $g\Omega > R$. But especially for the strongest

masers, a careful analysis of the brightness temperature is needed to confirm that the maser polarization is still in this regime. Thus, observing with ALMA full-polarization capabilities will enable us to use polarized maser emission as tracer of the magnetic field structure towards SFRs and CSEs of (post-)AGB stars. Depending on the maser spectral features detected, both the brightness temperature and the beaming solid angle can be better constrained, leading to a more accurate determination of the direction of the magnetic field in the masing region.

CHAPTER 5

Water maser polarization of the water fountains IRAS 15445−5449 and IRAS 18043−2116

We present the morphology and linear polarization of the 22-GHz H_2O masers in the high-velocity outflow of two post-AGB sources, d46 (IRAS 15445−5449) and b292 (IRAS 18043−2116). The observations were performed using The Australia Telescope Compact Array. Different levels of saturated maser emission have been detected for both sources. We also present the mid-infrared image of d46 overlaid with the distribution of the maser features that we have observed in the red-shifted lobe of the bipolar structure. The relative position of the observed masers and a previous radio continuum observation suggests that the continnum is produced along the blue-shifted lobe of the jet. It is likely due to synchrontron radiation, implying the presence of a strong magnetic field in the jet. The fractional polarization levels measured for the maser features of d46 indicate that the polarization vectors are tracing the poloidal component of the magnetic field in the emitting region. For the H_2O masers of b292 we have measured low levels of fractional linear polarization. The linear polarization in the H_2O maser region of this source likely indicates a dominant toroidal or poloidal magnetic field component. Since circular polarization was not detected it is not possible to determine the magnetic field strength. However, we present a 3-σ evaluation of the upper limit intensity of the magnetic field in the maser emitting regions of both observed sources. The contents of this chapter originally published in the MNRAS journal (Pérez-Sánchez, Vlemmings and Chapman 2011).

Post-Asymtoptic Giant Branch (post-AGB) stars represent a very short phase in the evolution of low and intermediate initial mass stars. During the post-AGB phase, the high mass-loss rate (10^{-7} – $10^{-4} M_{\odot} yr^{-1}$) observed at the end of the Asymtoptic Giant Branch (AGB) evolution decreases. Simultaneously, the effective temperature of the central star increases, while the circumstellar envelope (CSE) slowly detaches from the star (see Habing and Olofsson (2003) for a review). The post-AGB phase

ends when the central star is hot enough to ionize the material which was ejected from the AGB phase, forming a new Planetary Nebula (PN) (e.g. van Winckel 2003). It is generally assumed that the mass-loss process along the evolution in the AGB is spherically symmetric (Habing and Olofsson 2003). However, a high percentage of PNe have been observed showing aspherical symmetries that include elliptical, bipolar or multipolar shapes. It is still not clear at what point in the evolution toward a PNe the departure from the spherical symmetry starts and even more importantly, what the physical processes involved to form the complex shapes observed are. Companion interactions, binary sources, magnetic fields, fast and slow wind interaction, disks and a combination of these have been considered as the main factors to shape PNe (e.g. Sahai, Morris and Villar (2011), Balick and Frank (2002) and references therein).
Hydroxyl (OH) and Water (H_2O) maser emission have been observed in the CSE of the progenitors of the (pre-)PNe. Typically, for spherically symmetric CSEs, the double peak spectra of the OH masers defines the most blue- and red-shifted velocities in the CSE with respect to the stellar velocity. The velocity range of the H_2O maser spectra is narrower than the OH velocity distribution, and the H_2O masers are confined closer to the central star. A class of post-AGB stars, the so called "Water Fountains", is characterized by the detection of H_2O maser emission over an unusually large velocity range broader than the velocity range defined by the OH maser emission (Likkel and Morris 1988). Sources with H_2O maser velocity spread over a range of $\gg$ 100 km s^{-1} have been detected (e.g. Likkel and Morris (1988), Deacon et al. (2007), Walsh et al. (2009), Gómez et al. (2011)). Those H_2O masers have been observed in regions where the interaction between the high-velocity outflow and the slow AGB wind seems to be active, hence the H_2O masers are probably excited in the post-shock region. Recent infrared imaging of water fountains have revealed bipolar and multipolar morphologies (Lagadec et al. 2011). Vlemmings, Diamond and Imai (2006) have detected circular and linear polarization in the H_2O maser features along the jet of W43A, the archetypal water fountain. They found that the jets of W43A are magnetically collimated. Therefore, the detection of polarized maser emission from water fountains is useful to determine the role of the magnetic fields on the onset of wind asymmetries during the evolution from AGB stars to aspherical PNe. Here we report the detection of linear polarization of 22-GHz H_2O maser emission from two water fountains d46 and b292 (IRAS 15445−5449, IRAS 18043−2116).

5.1 Observation and data reduction

The Australia Telescope Compact Array (ATCA) was used to observe the H_2O maser emission from d46 (IRAS 15445−5449) on 2006 November 28-30 using the 6B array configuration, and b292 (IRAS 18043−2116) on 2007 July 6-9 with the 6C array configuration. The full track of observations of d46 was 8 hr, consisting of observations of the source interspersed with scans on the phase calibrator 1613−586. Later, b292 was observed over 16 hr, and likewise, its observations were interleaved with a phase reference source, 1730−130. The primary flux calibrator source, 1934−638, was observed during each observation program. The flux density of 1934−638 at 22.2-GHz was taken to be 0.81 Jy. Both

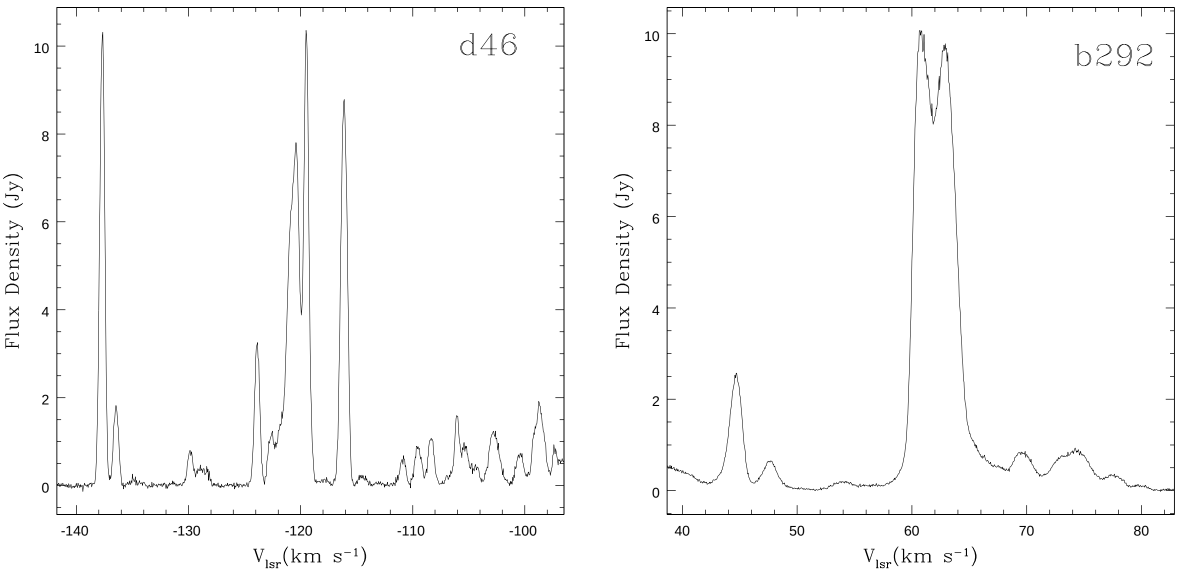

Figure 5.1: The observed section of the H_2O maser spectra for: d46 (IRAS 15445−5449), and b292 (IRAS 18043−2116). The velocity width of the spectra was limited by the bandwidth available at the ATCA at the time of our observations. The observations were centered on the brightest emission peak.

observations were performed in full polarization mode, with rest frequency of 22.23508-GHz, using 4-MHz bandwidth with 1024 spectral channels, covering a velocity width $\sim$ 50 km s^{-1} and a velocity resolution of 0.05 km s^{-1}. Before starting the full observations, some snapshots were carried out, for each source, to determine at what range of velocity the brightest emission occurred. As we could not cover the entire velocity range, the observing bands were centered on the brightest emission peak.
The data reduction was performed using the MIRIAD package (Sault, Teuben and Wright 1995). After flagging bad visibilities, the flux density for each phase calibrator was determined using the flux density of primary flux calibrator. We obtained flux densities of 1.83 Jy and 2.83 Jy for 1613−586 and 1730−130 respectively. Both sources were used to perform the polarization calibration as well as to determine amplitude and phase solutions, which were applied to the corresponding target data set. For polarization analysis, image cubes for stokes I, Q, U and V were created. The resulting noise level in the emission free channels of the I cube of d46 was $\sim$ 37 mJy beam^{-1}, whereas that of b292 was $\sim$ 13 mJy beam^{-1}. The stokes I image cubes were analysed using the AIPS task SAD, which was used to fit, channel by channel, all the components with peak flux densities higher than five times the rms with two-dimensional Gaussians. Only those maser features found in at least five consecutive channels were considered reliable detections. The Right Ascension and Declination for the maser features were calculated as the mean position for each set of consecutive channels. Fig. 6.1 shows the H_2O maser spectra for both sources.

Table 5.1: Maser features.

d46 (IRAS 15445−5449)						
Feature	Peak Intensity (Jy beam^{-1})	RA (15 48 X)	DEC (−54 58 X)	V_{lsr} (km s^{-1})	P_L (per cent)	χ (deg)
1	11.662	19.4063	20.165	−137.6	4.1 ± 0.6	−73.0 ± 1.6
2	2.055	19.4064	20.155	−136.5	7.5 ± 0.7	−40.7 ± 4.6
3	0.909	19.4025	20.099	−129.9	–	–
4	0.537	19.4086	20.090	−128.9	–	–
5	5.021	19.3972	19.942	−123.8	–	–
6	9.077	19.4032	20.069	−120.4	3.4 ± 0.9	−51.6 ± 13.1
7[a]	11.883	19.4038	20.083	−119.5	2.9 ± 0.5	−56.5 ± 4.8
8	10.334	19.4029	20.057	−116.1	8.3 ± 0.9	83.4 ± 2.7
9	0.351	19.3950	19.922	−114.9	–	–
10	0.735	19.3736	19.363	−113.2	–	–
11	0.820	19.4012	20.041	−110.8	–	–
12	1.166	19.3994	19.997	−109.5	–	–
13	1.380	19.3897	19.977	−108.4	–	–
14	2.055	19.4011	20.011	−106.4	–	–
15	1.619	19.3960	19.898	−105.3	–	–
16	2.201	19.3564	19.933	−104.2	–	–
17	2.606	19.3912	19.851	−102.8	–	–
18	2.922	19.3598	19.889	−100.3	–	–
19	7.142	19.3593	19.858	−98.6	–	–
20	3.209	19.3601	19.824	−97.3	–	–
b292 (IRAS 18043−2116)						
Feature	Peak Intensity (Jy *beam*$^{-1}$)	RA (18 07 X)	DEC (−21 16 X)	V_{lsr} (km s^{-1})	P_L (per cent)	χ (deg)
1	2.820	20.8484	11.845	44.7	–	–
2	0.751	20.8485	11.891	47.7	–	–
3	0.240	20.8500	11.886	54.3	–	–
4[a]	11.206	20.8480	11.860	60.8	1.3 ± 0.2	−4.2 ± 4.9
5	10.821	20.8485	11.865	62.9	1.5 ± 0.2	−6.8 ± 7.3
6	0.942	20.8483	11.844	69.4	–	–
7	0.500	20.8488	11.835	72.0	–	–
8	1.023	20.8477	11.838	74.3	–	–
9	0.667	20.8484	11.880	77.6	–	–
10	0.163	20.8476	12.040	79.8	–	–

[a] Reference features in figures 5.2 and 5.3

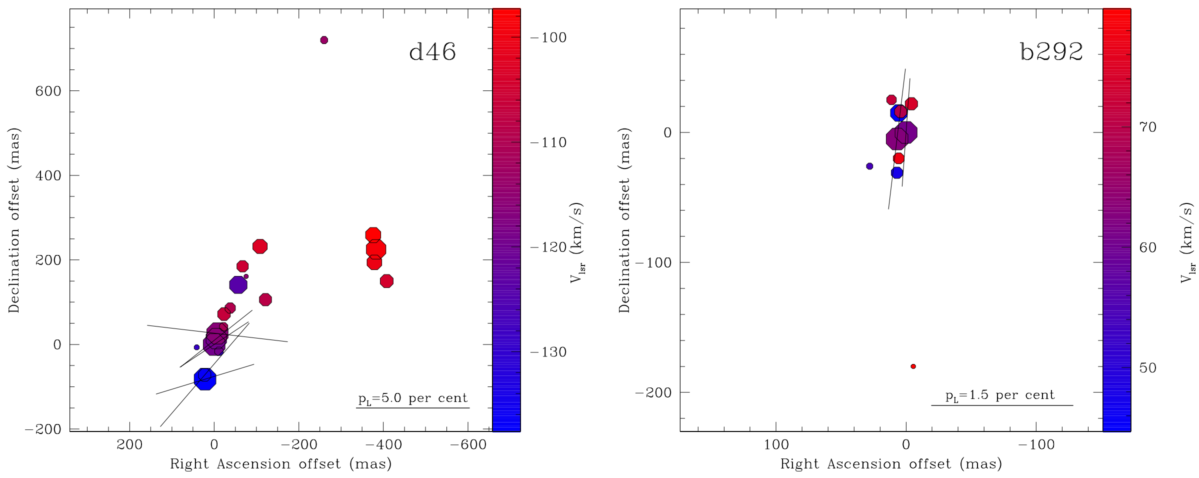

Figure 5.2: H_2O maser region of d46 (*left*) and b292 (*right*). The offset positions are with respect to the reference position indicated in table 5.1 , which are the brightest maser spots in each region. The vectors show the polarization angle, whose length is scaled according the linear polarization fraction. The horizontal bar at the bottom of each image sets 5 per cent (d46) and 1.5 per cent (b292) of linear polarization fraction.

5.2 Results

In Table 5.1, we present the results of the analysis of the H_2O masers features of d46 and b292. We list the peak intensity, the position as RA and DEC, LSR velocity ($V_{\rm lsr}$), fractional linear polarization (p_L) and polarization angle (χ). In Fig. 5.2 we show a map of the H_2O maser regions for both observed sources. The size of each feature is scaled according to the peak intensity, the radial velocity is colour-coded and the vectors show the polarization angles. We have identified twenty H_2O maser features for d46, with emission detected at velocities from -97.3 km s^{-1} to -137.6 km s^{-1}, red-shifted respect to the systemic velocity ~ -150 km s^{-1} (Deacon et al. 2007). Fractional linear polarization has been detected for five of the twenty features, particularly for the most blue-shifted features, with levels from 2.9 ± 0.5 per cent to 8.3 ± 0.9 per cent. No significant circular polarization was detected.

Ten H_2O maser features have been identified in our observation of b292, with emission at velocities from 44.7 km s^{-1} to 79.8 km s^{-1}. Deacon, Chapman and Green (2004) have derived the systemic velocity of the source from the double-peaked 1665-MHz spectrum, obtaining a stellar velocity of 87.0 km s^{-1}. Thus, because of the limited bandwidth, our observation was restricted to blue-shifted velocities only. Fractional linear polarization was detected only for the two brightest features. As presented in table 5.1, not only are the fractional linear polarization levels for both features almost the same, but so is the polarization angle. As was the case for d46, no significant circular polarization was detected.

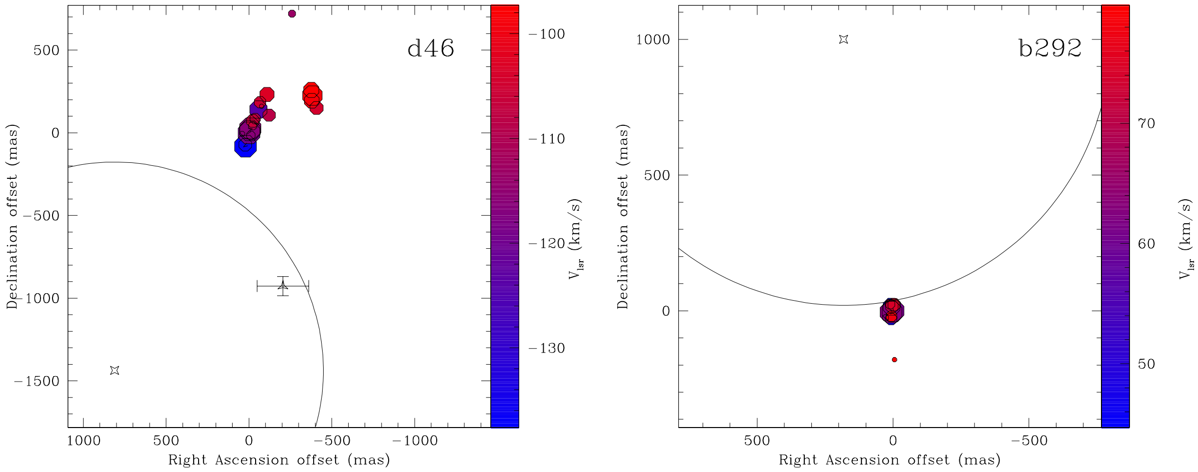

Figure 5.3: The image in the left shows the position of the radio continuum emission (triangle with error bars) (Bains et al. 2009), the OH position (star) and its uncertainty (arc) (Deacon, Chapman and Green 2004) with respect to the H_2O maser features that we have detected for d46. In the same way, the right image shows the OH position (star with four peaks) and its uncertainty (arc) relative to the H_2O maser features from our analysis for b292

5.3 Discussion

5.3.1 d46 (*IRAS 15445−5449, OH326.530−00.419*)

Previous Observations

According to the MSX ([8−12],[15−21]) two-colour diagram, d46 has been classified as a highly-evolve late post-AGB object (Sevenster (2002), Deacon, Chapman and Green (2004), Bains et al. (2009)). After 22-GHz H_2O maser emission was detected with a velocity range beyond that of the OH masers, it was classified as a water fountain source (Deacon et al. 2007).

Both main-line and 1612-MHz OH maser emission have been detected toward d46 (Sevenster et al. (1997b), Deacon, Chapman and Green (2004)). Based on the irregular line profile of the three lines detected, Deacon, Chapman and Green (2004) suggested that the source was likely a bipolar object, since irregular OH maser profiles are associated with sources that almost certainly have bipolar outflows and a remnant AGB wind. This hypothesis was confirmed by the Mid-infrared images (11.85 and 12.81 μm) of the source, obtained with VISIR/VLT and recently published by Lagadec et al. (2011). From the images the bipolar structure of the object is clear, with dust emission around the jet lobes. Indeed, the infrared photometry and the IRAS LRS data reported in the literature (Bains et al. (2009), Lagadec et al. (2011)) show that the contribution at short wavelengths, which is due to the photospheric component, is

still weak and the double-peaked infrared SED, characteristic of post-AGB objects, is mainly dominated by the dust emission. Therefore, the central star is surrounded by an optically thick structure (Lagadec et al. 2011) which could be a dense equatorial torus.
Non-thermal radio continuum emission has been detected at 3, 6 and 13 cm (Cohen et al. (2006), Bains et al. (2009)) with significant flux variation among the observations (spectral index $\alpha \approx -0.8$ (Cohen et al. 2006), $\alpha \approx -0.34$ (Bains et al. 2009)). Such detections have been associated with synchrotron emission produced by shocks between the high-velocity wind and the slow AGB remnant. The flux variation has been interpreted as episodic shocks between both wind components.

The H_2O masers

We have observed H_2O maser features only from the red-shifted velocities with respect to the OH maser features, which are centered at ~ -150 km s^{-1} (Deacon et al. 2007). The brightest features were detected between -115.0 and -140.0 km s^{-1}, considering the overlapped region, the overall H_2O spectrum that we have detected is quite similar to the spectrum detected by (Deacon et al. 2007), although as expected with some difference of the flux densities. Fig. 5.2 (*left*) shows that the projected spatial distribution of the H_2O maser features resembles a bow-shock-like structure, similar to that observed by (Boboltz and Marvel 2005) for the water fountain OH 12.8−0.9. Fig. 5.3 (*left*) shows both the OH and radio continuum positions with respect to the projected distribution of the 22-GHz H_2O maser features that we have detected. The solid circle represents the uncertainty on the OH position, the error bars show the accuracy of the radio continuum position, whereas the error on the H_2O maser position of each feature is within the size of the symbols. The offset of the radio continuum position with respect to that of the H_2O maser agrees very well with the mid-infrared image, and it seems likely that both emitting region are at different points along the jet. In fact, since the H_2O maser features have been produced at the red-shifted side of the jet, the position of the radio continuum could be related to the position of the central star. But, because the spectral index of the radio continuum implies non-thermal emission (Deacon et al. 2007) it is more likely synchrotron radiation produced at a region along the jet. This suggests the presence of a strong magnetic field along the axis defined by the direction of the high-velocity outflow. In Fig. 5.4 we show the Mid-Infrared image of d46 recently published by (Lagadec et al. 2011). The corrected position of the center of the mid-infrared image is RA 15 48 19.420, DEC −54 58 20.100, with an error circle of radius 2 arcsec (Lagadec, private comunication). Thus, as the relative positions are not known accurately enough, for illustration we have overlaid the H_2O maser features with the red-shifted lobe. The offset of the continuum emission suggest that it could arise from the blue-shifted lobe, as an effect of a strong magnetic field, as mentioned above. Although the error of the OH position encloses part of the blue-shifted lobe, it is likely produced in the outer shells of the CSE where the gas has been accelerated to high velocities through wind-wind collisions.

Magnetic field

Two of the maser features were detected to have a high percentage of linear polarization ($p_L > 5$ per cent), which likely is a result of maser emission in the saturated regime (Vlemmings et al. 2006). For H_2O masers, the percentage of linear polarization depends on the degree of saturation of the emiting region and on the angle (θ) between the direction of the maser propagation and the magnetic field lines. Additionally, there is a critical value $\theta_{\rm crit}$, such that if $\theta \lesssim \theta_{\rm crit} = 55°$, the polarization vectors are parallel to the magnetic field lines, otherwise they both are perpendicular. According to the p_L levels measured, the polarization vectors in Fig. 5.2 should be perpedicular to the magnetic field lines. The vectors then appear to trace the poloidal field component, ie, along the direction of the high-velocity outflow. We did not detect circularly polarized emission. As the masers are relatively weak the resulting 3-σ magnetic field limit is high, $|B_{||}| < 470$ mG.

5.3.2 b292 (*IRAS 18043−2116, OH009.1−0.4*)

Previous Observations

According to its position on the ([8]−[12],[15]−[21]) MSX two-colour diagram (Sevenster 2002), b292 is likely to be a young post-AGB object (Sevenster (2002), Deacon, Chapman and Green (2004)) . This source was confirmed as a water fountain by Deacon et al. (2007), who have detected 22-GHz H_2O maser emission over a wide velocity range of ≈ 210 km s^{-1}. In later observations performed by Walsh et al. (2009) H_2O maser emission over the even larger velocity range of 398 km s^{-1} has been detected, one of the largest velocity spread in any Galactic H_2O maser source. Until the recent observation reported by Gómez et al. (2011), it was the water fountain with the largest range in H_2O maser velocities. In addition, b292 was the first post-AGB object discovered with emission from the 1720-MHz OH satellite line (Sevenster and Chapman 2001). The 1720-MHz OH transition is produced in regions with special conditions of temperature and density and it is often associated with both Galactic star-forming regions (SFRs) and Supernova remnants (Lockett, Gauthier and Elitzur 1999). Its detection is interpreted as an indicator of the existence of C-shocks in the emitting regions. The detection of OH maser emission at 1665-MHz and 1612-MHz associated with the position of the 1720-MHz maser region did confirm that all the OH maser transitions are related to the same stellar source (Deacon, Chapman and Green 2004). In fact, the position offset from the 1665-MHz and 1612-MHz emitting region is less than 0.3” (Sevenster and Chapman 2001). Neither Sevenster and Chapman (2001) nor Deacon, Chapman and Green (2004) have detected the OH 1667-MHz maser transition, which is unusual for a source having maser emission at 1665-MHz.

The H_2O masers

As mentioned above, Walsh et al. (2009) have detected H_2O maser emission at both blue-shifted and red-shifted velocities relative to the systemic velocity. The projected spatial distribution and position

of such features within the same velocity range (e.g. Fig. 2 of Walsh et al. (2009)) is quite consistent with the projected position of those features that we have detected (Fig. 5.2). But, considering that the observations were carried out with a time period of almost a year in between, it is important to point out the strong variability of the maser flux intesity. In our spectra (Fig. 6.1 *right*) there is no maser emission at 53.1 km s^{-1}, while Walsh et al. (2009) detected the brightest peak at that velocity. Besides, they have detected our brightest feature at only a half the intensity.
As pointed out by Walsh et al. (2009), the spread in the projected distribution of the maser features with the most extreme velocities could be caused by a very small angle between the jet propagation direction and the line-of-sight. In addition, Sevenster and Chapman (2001) have pointed out that the lack of a second (red-shifted) peak of the 1720-MHz OH maser emission might be because the line-of-sight is almost parallel to the jet propagation direction. Although high-resolution images have not been obtained, we can thus assume that we are looking at the emerging jet almost pole-on. From Walsh et al. (2009), the projected orientation in the sky of the jets is East-West. The 22-GHz H_2O maser transition is probably excited by the shock front of the high-velocity outflow, which hits the slow expanding AGB envelope. Surcis et al. (2011b) have reported detection of 22-GHz H_2O maser emission produced in regions under C-shock conditions in a high mass SFR. In late-type stars, C-shocks should be produced at the tip of the emergent outflows, whereas the post-shock region seems to achieve the necessary conditions to produce the 1720-MHz OH maser emission. Fig. 5.3 (*right*) indicates the position of the OH maser reported by Sevenster et al. (1997a) relative to the 22-GHz H_2O maser features identified in our analisys. The uncertainty of the OH maser position is represented by the solid circle.

Magnetic field

The fractional polarization level detected for the brightest features is low (< 5 per cent) and corresponds to non-saturated H_2O maser emission. Consequently, the polarization vectors could be either perpendicular or parallel to the magnetic field component projected in the sky plane. Considering the projected jet direction is East-West, this implies that the B-field is either almost exactly parallel or perpendicular to the jet. The field in the H_2O maser region of b292 is thus potentially toroidal, as observed for W43A (Vlemmings et al. 2006) or poloidal as seen in d46. Significant levels of circular polarization were not detected. The 3-σ upper limit for the field strength is $|B_{||}| < 175$ mG.

5.4 Conclusions

We have used the ATCA to observe high-velocity H_2O emission from two late-type stars, d46 and b292. We have presented new high angular resolution images of the H_2O maser emission in parts of the jet and measured linear polarization for both sources. The first H_2O maser maps of d46 show a bow-shock morphology similar to that of OH 12.8−0.9. According to the level of p_L that we have measured, the maser emission is in the saturated regime, and the polarization vectors should be perpendicular to the

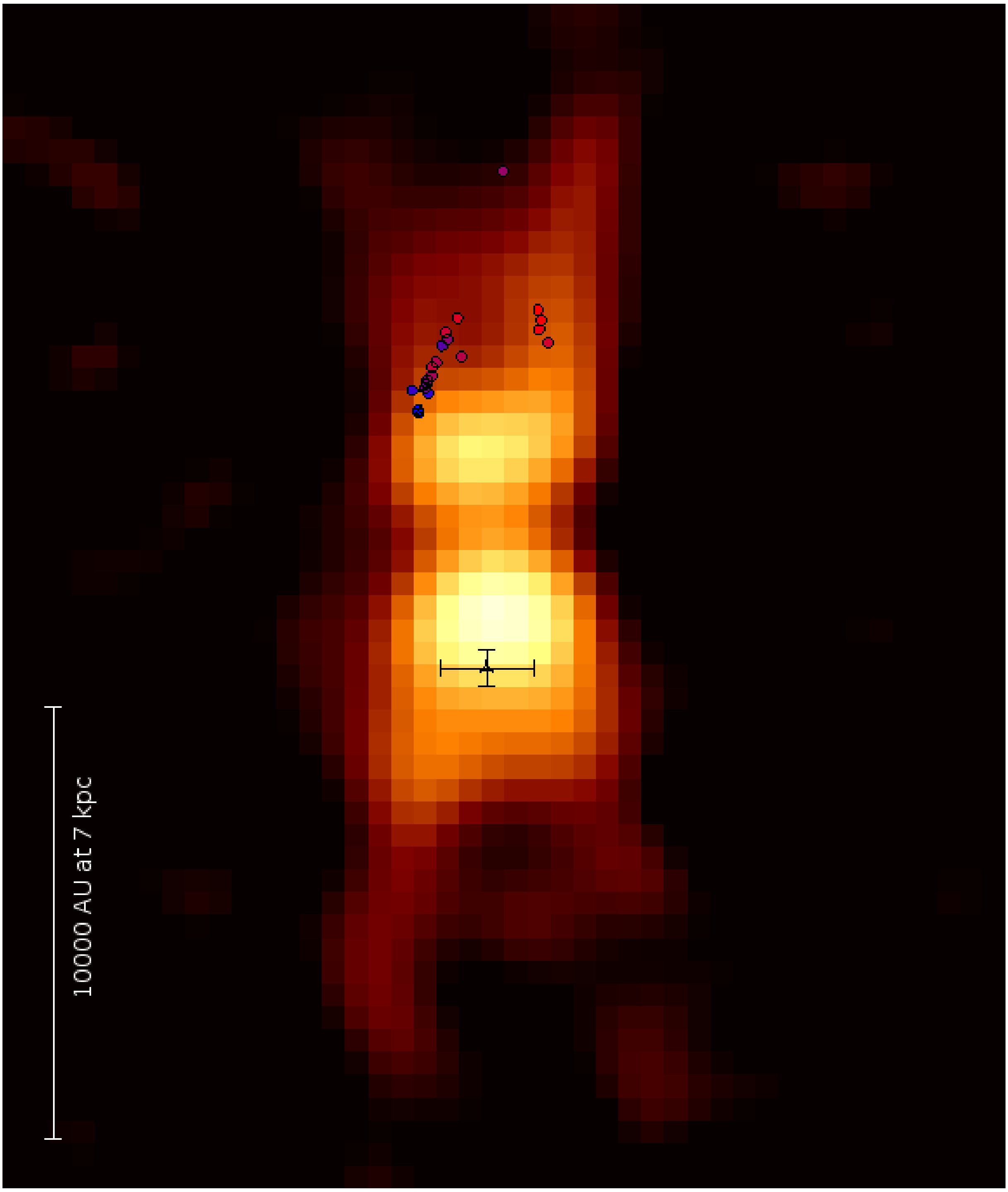

Figure 5.4: H_2O maser and radio continuum position overlaid on the mid-infrared image published by (lagadec). For illustration, we have shifted the mid-infrared image, within the 2 arcsec of uncertainty of its position, in order of align the H_2O maser features with the red-shifted side of the high-velocity outflow.

magnetic field lines, which consequently are the poloidal component. In Fig. 5.4 we have overlaid the position of the masers with the red-shifted lobe of the jet on the mid-infrared VLTI image of d46 from Lagadec et al. (2011). The relative position of the radio continuum emission with respect to those maser features suggest that it is arising from the blue-shifted lobe and is likely due to synchrotron radiation, indicating the potential presence of a significant magnetic field in the jet. Circular polarization was not detected, and we cannot infer the magnetic field strength along the line-of-sight to better than a 3-σ limit of $|B_{||}| < 470$ mG for d46. New polarization observations, including that of the radio continuum emission and a broader velocity range of the H_2O spectrum could give accurate measurements of the magnetic field strength along the jets of d46. For the H_2O of b292 we have measured low p_L levels, and the polarization vectors could be either parallel or perpendicular to the magnetic field lines projected on the sky plane. In fact, the projection of the jets in the sky is likely East-West, and the polarization vectors could be associated to either the poloidal (i.e. East-West) or toroidal (i.e. North-South) component of the B-field. Also in this case, no significant levels of circular polarization were not detected. The 3-σ upper limit for the magnetic field strength, is $|B_{||}| < 175$ mG.

CHAPTER 6

First resolved image of a synchrotron jet towards a post-AGB star.

The evolution of low- and intermediated-inital-mass stars beyond the asymptotic giant branch (AGB) remains poorly understood. High-velocity outflows launched shortly after the AGB phase are thought to be the primary shaping mechanism of bipolar and multipolar planetary nebulae (PNe). However, little is known about the launching and driving mechanism for these jets, whose energies often far exceed the energy that can be provided by radiation pressure alone. Here, we report, for the first time, direct evidence of a magnetically collimated jet shaping the bipolar morphology of the circumstellar envelope of a post-AGB star. We present radio continuum observations of the post-AGB star IRAS 15445−5449, which has water masers tracing a fast bipolar outflow. We resolve a radio jet, whose spectral energy distribution (SED) has a steep negative spectral index above ~ 3 *GHz. The SED is consistent with a synchrotron jet embedded in a sheath of thermal electrons. The jet is found to be responsible for the bipolar shape of the object observed at other wavelengths, and is collimated by a magnetic field of approximately 1.2 mG. We recover observations from the ATCA archive that indicate that the emission measure of the thermal component has increased by a factor of four between 1998 and 2005 after which it has remained constant. The short timescale evolution of the radio emission suggests a short lifetime for the jet. The observations of a synchrotron jet from a post-AGB star with characteristics similar to those from protostars suggest that magnetic launching and collimation is a common feature of astrophysical jets. The contents of this chapter originally published in MNRAS letters (Pérez-Sánchez et al. 2013).*

Synchrotron radiation is commonly detected towards relativistic jets emerging in high-energy astrophysical sources such as active galactic nuclei and quasars. It also has been detected towards a magnetized jet from a young stellar object (YSO) (Carrasco-González et al. 2010), where owing to density and temperature conditions, relativistic outflows were thought to be unlikely. The mechanism that leads to synchrotron emission involves the interaction between relativistic particles moving in a region where the dynamics are controlled by a magnetic field. Highly collimated outflows, similar to those seen toward YSOs, have also been found in the vicinity of post-Asymptotic Giant Branch (post-AGB) stars (Bujarrabal et al. 2001). If these high-velocity outflows are launched under the influence of strong magnetic fields, synchrotron emission could be expected. However, to date, no direct evidence of synchrotron radio emission exists from these high-velocity sources. Post-AGB stars are thought to represent the group of stars that recently left the asymptotic giant branch (AGB) phase and will develop into a planetary nebula (PN) (van Winckel 2003). During the evolution of low- and intermediate-initial-mass stars ($\sim$ 1-8 $M_\odot$) on the AGB, high mass-loss rates ($10^{-7} < \dot{M} < 10^{-4}$ $M_\odot$ yr^{-1}) together with an acceleration mechanism, which drives the ejected material outwards, lead to the formation of a dense and extended circumstellar envelope (CSE). The CSE expands outwards in radial directions with constant velocity of order 10 km s^{-1}. Generally, it is assumed that the mass-loss process is spherically symmetric during the AGB (Habing and Olofsson 2003) and that asymmetries form in a short timescale before entering the PNe phase (e.g. Sahai et al. 2007). Therefore, the post-AGB is a key phase for the understanding of the evolution of the CSE, where the mechanism(s) responsible for shaping asymmetric PNe must become important. Binary systems, large-scale magnetic fields and interactions with sub-stellar companions are among the proposed mechanisms that can generate aspherical CSEs (Balick and Frank 2002). The evolution of the CSEs beyond the AGB often involves the interaction between a fast collimated wind, which could be created during the very last thermal pulses of the central star, and the steadily expanding CSE formed during the AGB. Strong evidence of this interaction and of the generation of strong shocks within the CSE, is the detection of post-AGB sources with water maser emission spread over unusually large velocity ranges ($\geq$ 100 km s^{-1}) the so called water fountains (Likkel and Morris (1988), Gómez et al. (2011)). The peculiar H_2O maser emission is thought to trace regions that have been swept up by a high-velocity outflow. Polarized H_2O maser emission has also been detected towards water fountains, suggesting that the high-velocity outflow of at least one of the water fountain sources is collimated by the magnetic field (Vlemmings, Diamond and Imai 2006). Nevertheless, the lauching mechanism of high-velocity outflows in post-AGB stars, as well as the origin of the collimating magnetic field, are still under debate. One of the 20 detected water fountains is IRAS 15445−5449, which has been classified as an evolved post-AGB star according to the MSX two-color diagram (Sevenster (2002), Deacon, Chapman and Green (2004)). Observations have revealed H_2O maser emission spread over $\approx$ 100 km s^{-1}, with the spectral features redshifted with respect to the systemic velocity of the source. Based on both satellite- and main-line OH maser observations, Deacon et al. (2007) suggested that $v_{lsr} \approx -150$ km s^{-1}. We note however, that the source has also been classified as a massive YSO candidate in the RMS survey, where radio continuum was detected at 3 cm (Urquhart et al. 2007b), a classification that could be supported by the detection of relatively strong line emission of $^{13}CO(1-0)$ centered at -44 kms^{-1} (Urquhart et al. 2007a). However, if the ^{13}CO is associated with IRAS 15445−5449, the central velocity of the line emission will define the v_{lsr} of the source, and in that case, both the H_2O and OH maser emission would arise from a blue-shifted outflow. Specifically, this would imply that the OH emission centered at $v_{lsr} \approx -150$ km s^{-1} and spread over ~ 60 km s^{-1}, originates in an outflow with velocity > 200 km s^{-1}. This would correspond to the highest velocity Galactic OH maser and is very unlikely. Additionally, strong Galactic CO emission is known to occur around -40 km^{-1}, leading us to conclude that the ^{13}CO emission is likely Galactic in origin and not associated with 15445−5449. Although a YSO classification cannot yet be ruled out, its classification as a post-AGB star is more likely. The projected spatial distribution of the detected H_2O maser features resemble a bow-shock structure at the red-shifted lobe, which is likely caused by a collimated outflow that pierces the steady-expanding CSE of the AGB phase (Pérez-Sánchez, Vlemmings and Chapman 2011). Additionally, mid-infrared images confirm the bipolar morphology of this source (Lagadec et al. 2011). Finally, strong and seemingly non-thermal radio emission was detected and thought to arise from either the star itself or a shocked interaction region between the AGB envelope and a fast wind (Bains et al. 2009). Here we report observations indicating the radio continuum to originate from a jet.

6.1 Observations and results

6.1.1 Recent and archive observations

We performed observations of IRAS 15445−5449 with the Australia Telescope Compact Array (ATCA) on 2012 September 2. The 12-h observation run was carried out with the 6A array configuration, using 2 GHz bandwidths at 1.3 cm, 3 cm, 6 cm, and 16 cm. The observations with the 1.3 cm and 16 cm bands were carried out using the Compact Array Broadband Backend (CABB) mode 1 M-0.5 k, whereas the 3 cm and 6 cm bands were set up simultaneously with CABB mode 64 M-32 k. The four bands were set up in full polarization mode. The calibration and the imaging of the data were done using the package MIRIAD (Sault, Teuben and Wright 1995). Bandpass and flux calibration were performed on the standard calibrator 1934−638 and phase calibration was performed on 1613−586. The flux densities for 1934−638 were taken from the available models of this calibrator. The flux densities of 1613−586 were determined in order to check the absolute flux calibration accuracy. The measured flux densities for this source are in agreement with the values presented in the ATCA calibrators database, within an uncertainty of less than 10%. The bands at 3 cm, 6 cm, and 16 cm were split in two sub-bands each, in order to confirm a potential steep spectral index over the large fractional bandwidth at these wavelength. After calibration, the imaging of the source was performed using multifrequency synthesis. The different maps were deconvolved using the MIRIAD task MFCLEAN, with which Stokes I, Q, U and V images were produced. No linear or circular polarization was detected. Maps of smaller frequency ranges were created in order to test if the lack of linear polarization was due to a large rotation measure across the individual bands, but the emission was found to be unpolarized. We also retrieved radio continuum observations of IRAS 15445−5449 from the Australia Telescope Online Archive, the results of which are included in Table 6.1.

Table 6.1: Flux density of IRAS 15445−5449.
[a] This paper, [b] Bains et al. (2009), [c] Observations carried out on 1998 June 13 (D. Hunstead, private comunication; (Murphy et al. 2007)), [d] Observations taken on 1999 September 2 (ATCA archive), [e] Observations carried out on 1998 November 9−14 (Deacon et al. 2007).

Epoch 2012[a]			Epoch 2005[b]			Epoch 1998/99		
Freq (GHz)	Flux (mJy)	Beam (arcsec^2)	Freq (GHz)	Flux (mJy)	Beam (arcsec^2)	Freq (GHz)	Flux (mJy)	Beam (arcsec^2)
-	-	-	-	-	-	0.84	32.5±4.1[c]	-
2.1	20.36±0.14	5.6×3.0	-	-	-	1.4	23.0±5.3	7.6×4.9[d]
2.5	21.72±0.05	4.7×2.6	-	-	-	2.5	31.2±6.2	3.3×3.0[e]
5.0	25.41±0.04	1.9×1.5	4.8	22.81±1.11	5.6×2.1	4.8	18.4±2.4	2.0×1.6[e]
5.8	23.59±0.05	1.6×1.3	-	-	-	-	-	-
8.5	18.45±0.05	1.1×0.9	8.6	18.67±0.47	3.0×1.2	8.6	10.7±2.3	1.2×0.8[e]
9.3	17.70±0.03	1.0×0.8	-	-	-	-	-	-
22.0	12.31±0.03	0.48×0.34	-	-	-	-	-	-

6.1.2 Maps and spectral energy distribution

The derived flux densities, the beam size, and the rms of each map of IRAS 15445−5449 are listed in Table 6.1 for our observations in 2012, the observations in 2005 reported by (bains), and the data taken from the ATCA archive. The source was detected in 1998 at 0.84 GHz (D. Hunstead, private comunication; (Molonglo)). It was also detected during another survey between 2002 and 2004 at 8.6 GHz, with a flux density of 11.9 mJy (Urquhart). The observed spectral energy distribution (SED) of IRAS 15445−5449 at radio frequencies is characterized by a turn-over around $\nu_c \approx 3$ GHz (Fig. 6.1) with a steep negative spectral index at higher frequencies. Between 5.0 GHz and 22 GHz the continuum emission has a spectral index $\alpha = -0.56$. At 22 GHz we resolved the dense continuum emission along the north-south direction (Fig. 6.2) extending about 1.9 arcsec, which is consistent with the bipolar morphology seen in the mid-infrared image of the source (Fig. 6.3).

6.2 Analysis

6.2.1 Model

The shape of the SED indicates that the radio continuum is a superposition of a foreground thermal component, which is optically thick for $\nu < \nu_c$, and a non-thermal component, which dominates the radio continuum flux when the thermal component becomes optically thin, i.e., for $\nu \geq \nu_c$. We model the observations as arising from non-thermal emission in a cylindrical region surrounded by a sheath of thermal electrons with constant density ($n_e = 3.5 \times 10^4$ cm^{-3}) and temperature ($T_e = 6000$ K) and a thickness of approximately 1000 AU. The thickness is limited by the unresolved width of the emission at 22 GHz. The brightness temperature of the non-thermal jet implies its width to be less than 500 AU.

For this configuration the emission has two regimes: at low frequencies the thermal emission becomes optically thick, which causes the emission from the non-thermal electrons to be absorbed, and the SED to exhibit a positive spectral index. On the other hand, since at high frequencies the thermal emission becomes optically thin, the contribution from the non-thermal electrons becomes dominant, resulting in the negative spectral index. Although the spectral index indicates synchroton emission, polarized emission was not detected. This is a direct consequence of depolarization due to the thermal electrons surrounding the region where the synchrotron emission arises.

6.2.2 Fermi acceleration and magnetic field

Our best fit to the observed SED implies a spectral index $\alpha = -0.68 \pm 0.01$ for the non-thermal component. As the stellar temperature is approximately 12000 K (Bains et al. 2009), ionization by the star is unlikely to provide many free electrons. But, if we assume a strong shock (J-shock) between the magnetically collimated outflow and the slow AGB wind, then ionized material will propagate downstream throughout the shock-front. Eventually, a fraction of the electrons will be accelerated to relativistic speeds through the Fermi shock acceleration mechanism. Hence, Fermi accelerated electrons interacting with the magnetic field lines that collimate the outflow generate the observed non-thermal emission. Within this framework, we can assume that the total internal energy of the shocked region is split between the particles (electrons and protrons) and the magnetic field. When the total energy density is minimized with respect to the magnetic field, the energy density of the particles becomes nearly equal to the energy density of the magnetic field, and we can assume equipartition of the energy. This assumption enables us to estimate the strength of the minimum-energy magnetic field interacting with the relativistic electrons. This minimum-energy magnetic field and the minimum total energy can be calculated from

$$B_{min} = [4.5c_{12}(1+k)L/\phi]^{2/7}R^{-6/7}\ G, \quad \text{and} \tag{6.1}$$

$$E_{min} = c_{13}[(1+k)L]^{4/7}\phi^{3/7}R^{9/7} erg, \tag{6.2}$$

where R is the size of the source, L is the integrated radio luminosity, k is the ratio between the energy of heavy particles (protons) and the electrons, ϕ is the volume filling factor of the emitting region, and c_{12} and c_{13} are functions of both the spectral index, and the maximum and minumum frequencies considered for the integration of the spectral energy distribution (Pacholczyk 1970). The distance to the source is not known, and only its (near) kinematic distance has been reported $D = 7.1$ kpc. From the measured extent we estimate that the size of the source is $R = 6.74\times10^3$ [$D/7.1$ kpc] AU. Integrating the radio luminosity between $\nu_{min} = 10^7$ Hz and $\nu_{max} = 10^{11}$ Hz, assuming a spectral index of $\alpha = -0.68$, a volume filling factor $\phi = 0.004[D/7.1\ \text{kpc}]^{-2}$ (for a cylinder of 500 AU radius), and $k = 40$ (which is an appropriate value for electrons undergoing Fermi shock acceleration in a non-relativistic jet (Beck and Krause 2005), we obtain $B_{min} = 5.43\ [D/7.1\ \mathrm{kpc}]^{-2/7}$ mG and $E_{min} = 4.75 \times 10^{43}\ [D/7.1\ \mathrm{kpc}]^{3/7}$ erg. Since we have not detected any linear polarization, we cannot determine if the synchrotron radiation traces either the poloidal (B_r) or the toroidal (B_ϕ) component of the magnetic field. However, since $B_r \propto r^{-2}$, this component can likely be neglected at $r > 1000$ AU compared to the toroidal field, which has $B_\phi \propto r^{-1}$. Therefore, assuming that the measured magnetic field strength corresponds to the toroidal component at $R = 6.74 \times 10^3\ [D/7.1\ \mathrm{kpc}]$ AU, the magnetic field at $R_\star = 2$ AU is $B_\phi \approx 18.3\ [D/7.1\ \mathrm{kpc}]^{1/7}$ G, which is similar to the extrapolated magnetic field strengths towards other (post-)AGB stars from maser observations (e.g. Vlemmings, Diamond and Imai 2006).

6.2.3 Variability and lifetime

A negative spectral index was obtained from the archive observations towards IRAS 15445−5449 (Table 6.1). The spectral index below 13 cm, of the SED observed in 1998/1999, is $\alpha = -0.85 \pm 0.05$, with a turn-over frequency shifted toward a lower frequency compared with the SED observed in 2012. Additionally, radio continuum observation at 3 cm and 6 cm carried out in 2005 yielded a spectral index $\alpha = -0.34 \pm 0.24$ (Bains et al. 2009). Because it is a single data point taken between epochs 1998/99 and 2005, the observation at 3 cm reported by Urquhart et al. (2007b), which yielded a similar flux density to that reported by Bains et al. (2009), is not included in our fit. Since the time between the two observations is negligible compared with the synchrotron life time of relativistic electrons, we can assume that the flux of the synchrotron emission remained nearly constant between 1998 and 2012 and fit all observations considering a single synchrotron component and an increasing emission measure of the surrounding sheath of thermal electrons (Fig. 6.1). An increase of the emission measure by a factor of 3 between 1998 and 2005, and stable thereafter, can fit all three observational epochs. This implies that, assuming the dimensions of the surrounding sheath of thermal electrons remained the same, the electron density increased by a factor of two in seven years, likely by the same shock-ionization process that produces the electrons that are accelerated to relativistic velocities by the Fermi mechanism. In recent years, the production rate of thermal electrons is in equilibrium with their recombination rate. The stability of the non-thermal component over almost 15 years indicates that this emission is unlikely to originate from the colliding winds of binary systems such as observed around, for example, binary Wolf-Rayet stars (e.g. Chapman et al. 1999).

The rapid initial increase of emission measure between 1998 and 2005 likely implies the jet, responsible for the ionizing fast shocks, to have been launched only shortly before. Additionally, as the synchrotron flux depends on the effectiveness of the Fermi shock acceleration mechanism, once the shock front reaches outer layers where the strength of B_ϕ and the density of the CSE decrease, the synchrotron component would no longer be observable. This also suggest that the magnetically collimated outflow was launched recently. Thus, the lifetime of the synchrotron radiation toward post-AGB sources will most likely be determined by the time of propagation of the collimated outflow throughout regions of the CSE where the shock conditions enable the Fermi shock acceleration mechanism. Consequently, the

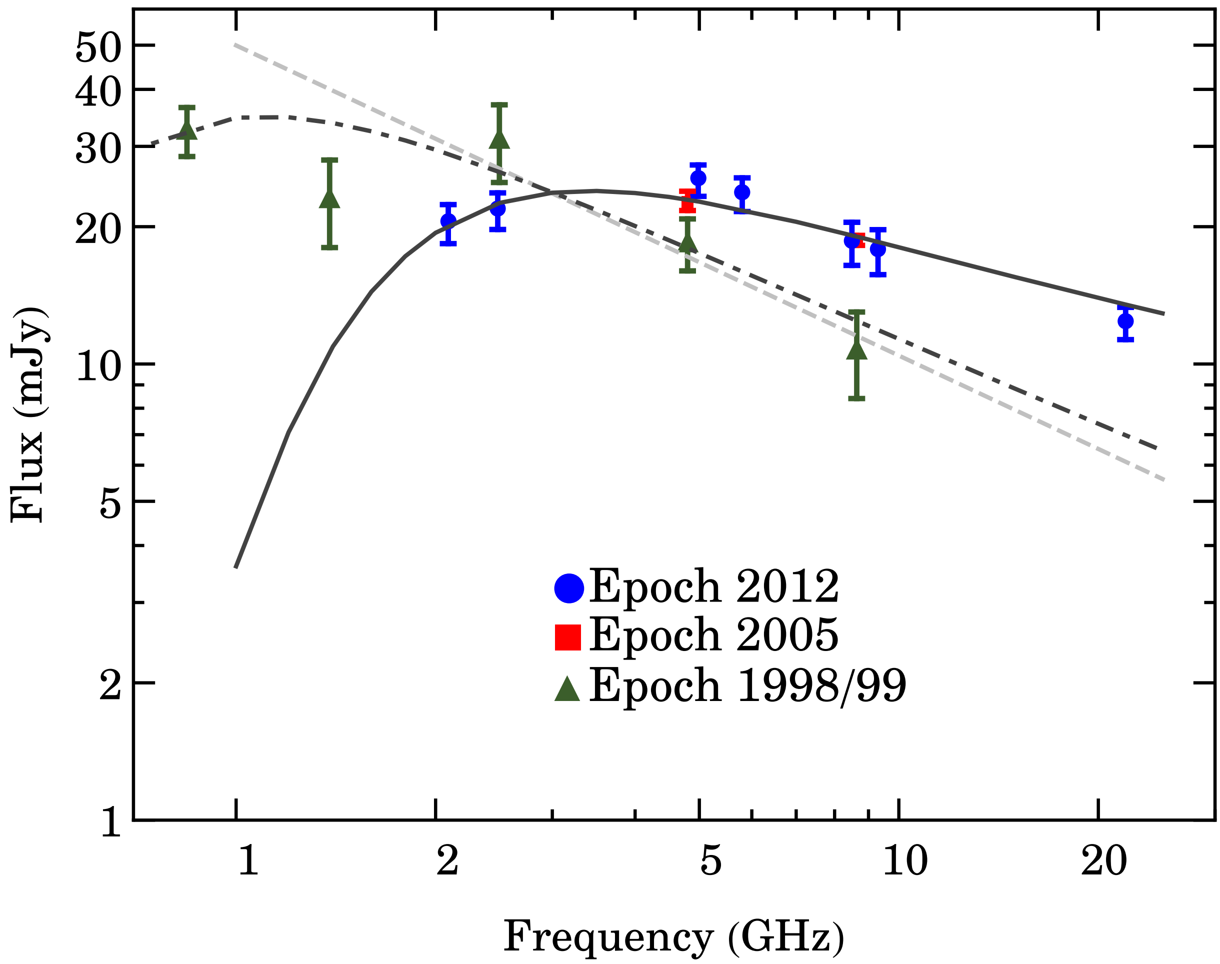

Figure 6.1: Spectral energy distribution of the radio continuum of IRAS 15445−5449 for three different epochs: 1998/99 (references listed in Table 6.1), 2005 reported by Bains et al. (2009), and our observation in 2012. The solid line (epoch 2012) and the dot-dashed line (epoch 1998/99) are the results of our models, that fit the observations. We consider a synchrotron jet surrounded by a sheath of thermal electrons. Assuming that the synchrotron emission remained constant between 1998 and 2012, our model suggest that the electron density of the region surrounding the synchrotron emitting region has increased by a factor of two between 1998 and 2005, and remained stable since then. The grey-dashed line indicates the synchrotron component. The best fit yielded a spectral index of $\alpha = -0.68 \pm 0.01$ for the synchrotron component.

time scale for the synchrotron radiation would at most be a few hundred years. Depending on the initial mass of the star, the synchrotron radiation time scale would be shorter than, or almost comparable with, the time scale of the post-AGB phase (van Winckel (2003) and references therein). The fact that the source is a water fountain suggests that, in principle, this kind of source would have conditions required to trigger the Fermi shock acceleration mechanism. Nevertheless, a larger sample of confirmed water fountains and further observations are necessary to directly correlate both phenomena.

6.2.4 Implications for post-AGB outflows

The physical processes responsible for shapping the asymmetrical envelopes observed towards PNe have been subject of intense debate along the last three decades. Recently, it has been suggested that the bipolar structures observed towards post-AGB stars and young PNe are associated with low-density axisymmetric regions that are illuminated by a central star obscured by a dense equatorial torus (e.g. Koning, Kwok and Steffen 2013). These low-density regions are assumed to be formed as a result of the propagation of high-momentum, collimated outflows that emerge from the inner regions of the CSE, creating cavities along the axis defined by its propagation direction. Nevertheless, the actual formation process of such cavities is not yet clear. On the other hand, observations of molecular outflows traced by CO lines towards a large sample of post-AGB stars revealed the existence of very fast collimated outflows (Bujarrabal et al. 2001). The momentum carried by most of these fast, highly collimated outflows cannot be explained considering a radiatively driven wind only, but the minimum energy calculated for the jet of IRAS 15445−5449 is within the typical range of the kinetic energy measured from the observation of these molecular outflows (10^{42} – 10^{46} erg). Magnetohydrodynamical simulations have shown that magnetic fields can be an important agent in the collimation of the outflows observed towards PNe (García-Segura et al. 1999). Dust polarization observations have been carried out in order to trace the magnetic field morphology. But so far the observational study of the properties of magnetic fields towards AGB and post-AGB stars and PNe has relied on the detection of dust polarization and polarized maser emission arising in their CSEs and high-velocity outflows (e.g. Sabin, Zijlstra and Greaves (2007), Vlemmings, Diamond and Imai (2006)). Our results provide strong observational evidence that indicates that the magnetic field is an important source of energy and is thus of great importance for the launching and driving mechanisms of the high-velocity jets from post-AGB stars. Furthermore, it will now be possible to directly test which class of magnetic launching models fits the observations (e.g. Huarte-Espinosa et al. 2012).

6.3 Discussion

For the first time, we resolve a synchrotron jet towards a post-AGB star. The resolved radio continuum emission is consistent with the bipolar morphology of IRAS 15445−5449 observed at the infrared, reported by Lagadec et al. (2011), and suggests the jet is responsible for shaping the CSE. Although

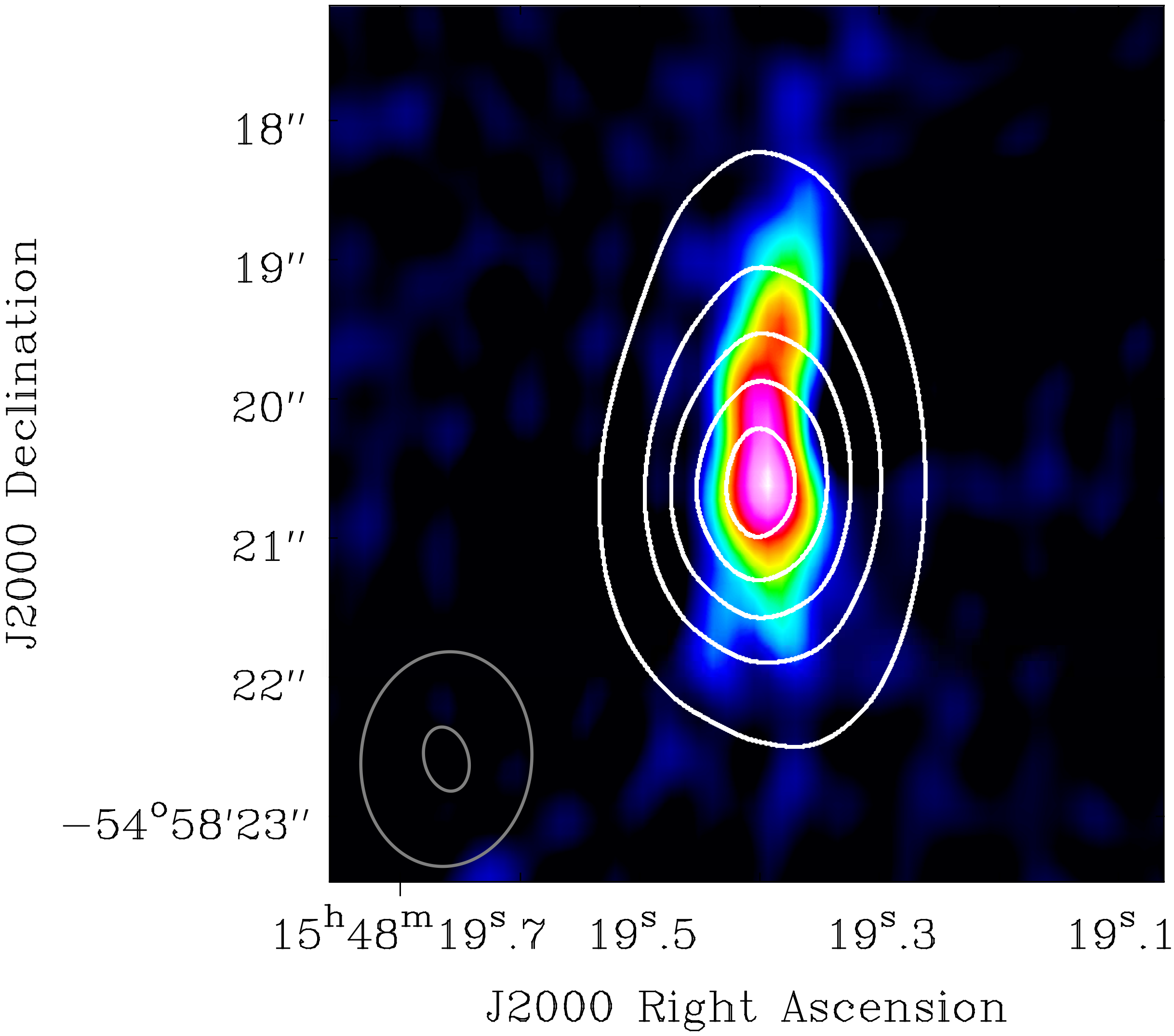

Figure 6.2: Radio continuum map of IRAS 15445−5449 at 22.0 GHz (color) and 5 GHz (contours). The peak-flux density of the 22.0 GHz image is 3.65 mJy/beam, while $\sigma = 5.0\times10^{-2}$ mJy. The contour lines at 5 GHz are drawn at 10, 30, 50, 70, and 90% of the peak flux of 16.6 mJy/beam. The beam size for the 22.0 and 5 GHz observations are drawn in the bottom left corner.

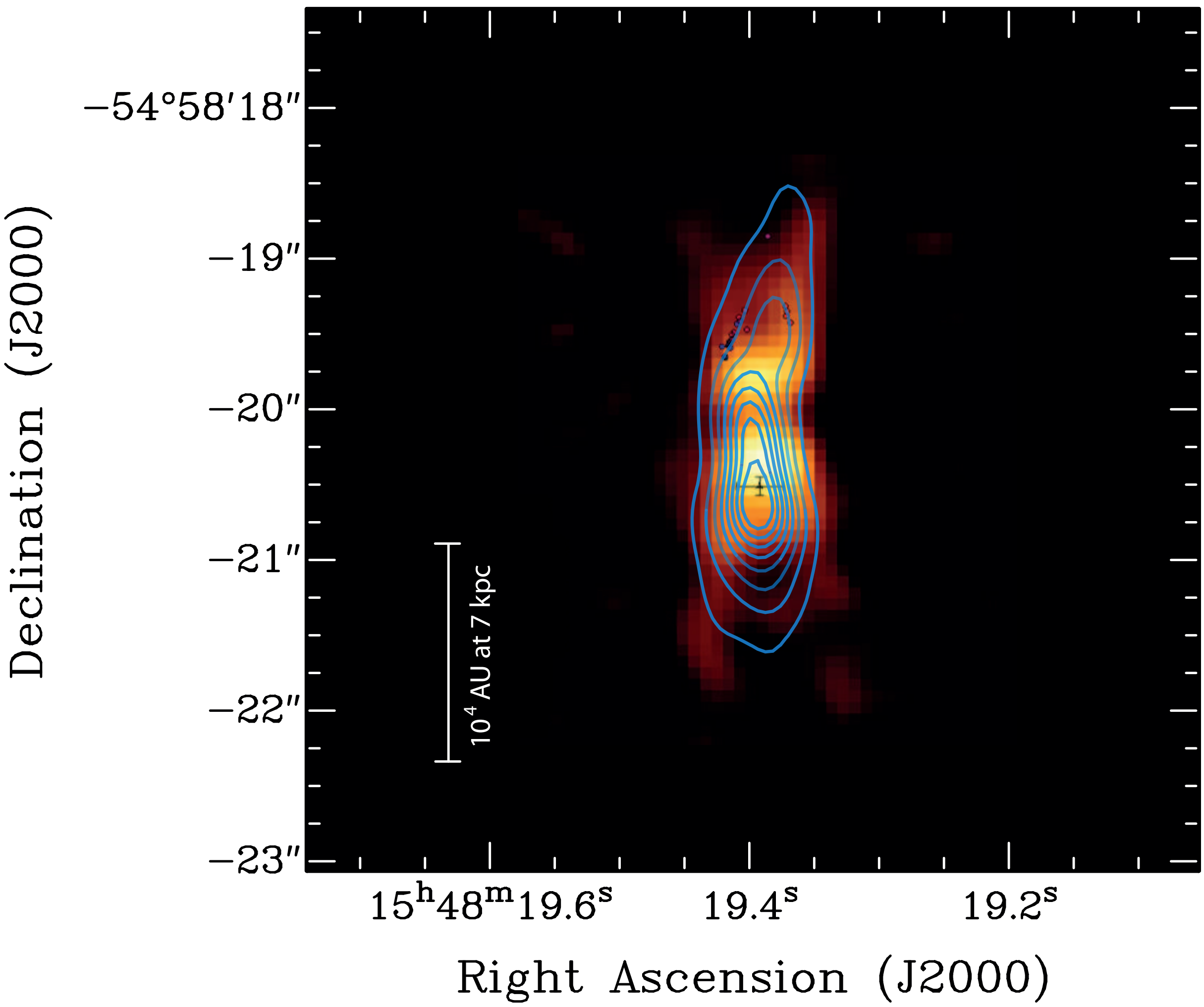

Figure 6.3: 2012 radio continuum map of IRAS 15445−5449 at 22.0 GHz (contours) overlaid on the mid-infrared VLTI image (Lagadec et al. 2011), the H_2O masers (colored symbols) observed in the redshifted lobe of the high-velocity outflow (Pérez-Sánchez, Vlemmings and Chapman 2011) and the radio continuum position (solid triangle with error bars) determined in the 2005 epoch (Bains et al. 2009). The contours are drawn from 10σ at intervals of 10σ. The mid-infrared image has been shifted to match the observed outflow for illustration, as the positional uncertainty of the mid-infrared observations, with an original centre of RA $15^h48^m19^s.42$ and Dec −54°58′20”.10, is 2 arcseconds.

both theoretical models and previous H_2O maser observations have been used to infer the presence of magnetically collimated outflows towards post-AGB stars, our result represents a direct observational evidence and the first unambigous proof that magnetic fields are a key agent to explain the asymetries observed towards PNe. Still, the source of the stellar magnetic field remains unclear. A large scale magnetic field could arise from (convective) dynamo action in a single star or require a binary (or planetary) system to be maintained. In one of the binary scenarios, the bipolar outflows are launched from a low-mass companion accreting mass ejected by the more evolved star. In this case, the collimation of the outflow might occur via a mechanism similar to that collimating the bipolar outflows from protostars, for example a disc-wind or an X-wind (Blandford and Payne (1982), Shu et al. (1994)). Our results cannot yet discern which is the most likely scenario for IRAS 15445−5449, although a hint of curvature might point to a binary ejection mechanism. Finally, our detection of synchrotron radiation towards IRAS 15445−5449 also demonstrates that the conditions for the Fermi shock acceleration of electrons can be attained at the final stages of the evolution of intermediate-initial-mass stars.

CHAPTER 7

CO line emission from asymmetrical AGB sources

Combining radio observations of circumstellar molecular line emission with radiative transfer models is one of the most reliable methods to better understand the processes behind the return of nuclear-processed material to the interstellar medium from stars evolving along the AGB (e.g Ramstedt et al. 2008). It is commonly used to constrain the kinematics and the chemical composition of the outflowing gas, which allows the study of the mass-loss history of the star, and also provides information concerning the nuclear processes that take place in the interior of the star prior to the material ejection. In this context, the CO molecule is the most studied species towards the CSEs of AGB sources (e.g Schöier and Olofsson 2001, and references therein); its high abundance relative to other molecular species in the CSEs makes it a solid probe of their molecular gas component. Due to the high dissociation energy of the CO molecule, as well as due to H_2- and self-shielding, the interstellar UV radiation affects the CO abundance only at the outermost regions of the CSEs of AGB stars. This fact makes the CO molecule also an unique indicator of the morphology and the size scales of CSEs of AGB stars. In addition, the CO molecule is a common species for all types of stars evolving along the AGB, i.e., M-, S- and C-type AGB stars.

In the CSEs of AGB stars, the excitation of the different CO rotational transitions is thought to be dominated by collisions with H_2 molecules, although radiative excitation via infrared emission may be more efficient for low mass-loss rate sources. In the ground vibrational state, the high energy radiative transitions of CO are usually found tracing regions with high temperatures, i.e., regions close to the central stars, while low energy CO transitions (J=2-1, 1-0) are observed through the entire CSEs, up to the outer regions where CO is finally photodissociated. Hence, observations of multiple CO radiative transitions towards a particular source can in principle be used to constrain the kinetic temperature distribution of the molecular gas within the regions traced by the CO emission.

Radio observations of CO emission yield broad line profiles whose shapes, width and integrated intensities can be related to physical properties of the emitting source such as, for instance, optical depth, kinetic temperature, expansion velocity, and morphology. However, the large number of variables and unknown parameters that need to be considered in the models leads to results which strongly depend on the model itself. In the case of the CO line emission, conservative values are generally assumed for parameters which account for distance to the source, photodissociation radii, heating and cooling processes, fractional abundances, isotopic ratios, dust-to-gas ratio, among many others. Constant gas expansion velocity and isotropic mass-loss rates are commonly assumed; the steady-wind scenario, which accounts for density distribution of H_2 falling as r^{-2} and constant mass-loss rates. The assumption of spherical symmetry is rather common and grounded on the scenario of isotropic mass-loss. Such assumption considerably reduce the computational cost of the modelling, and also simplify the treatment down to a one-dimension system where both the density and temperature distribution are functions of the distance to the star only. However, the new generation of telescopes such as ALMA represent an important increase of spatial resolution which allows us to identify substructures that can be related to large variations of the mass-loss rates or to anisotropic mass-loss such as asphericity, clumps, disks, and shells (e.g Maercker et al. 2012). Consequently, the sensitivity of one-dimensional radiative transfer models to the effects that such substructures, or the non-sphericity of the CSEs, can induce on the circumstellar emission lines needs to be evaluated in order to know the range of accuracy of their results. In this chapter we present the results of an initial approach to the problem of CSEs displaying nonspherical symmetric morphologies. Emission from synthetic sources are calculated aiming to analyse the CO spectral features which could be detected towards CSEs of AGB stars with morphologies resembling spheroids with different degrees of oblateness. Jura (1983) presented an analytic approach to oblate morphologies of CSEs, and here we present the results of full 3-D radiative transfer models using LIME (Brinch and Hogerheijde 2010). The models are described in section 7.1. The results and the analysis are presented in sections 7.2 and 7.3, respectively. Our conclusions are presented in section 7.4

7.1 The model

The models of CO line emission are calculated assuming that the CSEs are spheroids with different degree of oblateness. The simplest case is the spherical symmetric density distribution given by

$$\rho(r) = \frac{\dot{M}}{4\pi v r^2}, \tag{7.1}$$

where v is the expansion velocity of the CSE and $\dot{M}$ is the mass-loss rate.
When an anisotropic density distribution is assumed, the magnitude of the radial vector s is

$$s^2 = x^2 + y^2 + \frac{z^2}{a^2}, \tag{7.2}$$

where the parameter a is the ratio between the major and minor axis of the ellipsoid. That is, if $a = 1$ then $s = r$ and the density distribution is spherically symmetric. In the case of $a \neq 1$

$$s^2 = \frac{r^2}{a^2}((a^2 - 1)\sin^2\theta + 1). \tag{7.3}$$

where θ is the polar angle measured from the z-axis. Integrating the mass-loss over a spheroid of radius r and surface area dA, and assuming only the case of an oblate ellipsoid ($0 < a < 1$), the density distribution is

$$\rho(r, \theta) = \frac{\dot{M}}{4\pi v r^2} F(a, \theta). \tag{7.4}$$

where the factor $F(a, \theta)$ is

$$F(a, \theta) = \frac{a(1 - a^2)^{1/2}}{\tan^{-1}\left(\frac{(1-a^2)^{1/2}}{a}\right)(a^2\sin^2\theta + \cos^2\theta)}. \tag{7.5}$$

The result is an oblate ellipsoid where the gas density distribution extends further out over the x- and y-axis than along the z-axis. The oblate density distribution can be assumed as a result of anisotropic mass-loss and an isotropic velocity field or vice versa. In this case we assume the latest case, i.e., isotropic mass-loss rate and anisotropic velocity field that could be the result of the onset of a collimated outflow. Consequently, the expansion velocity along the major axis is v, while along the minor axis it is v/a. The factor $F(a, \theta)$ in Eq. 7.5 allows a direct comparison between the spherical and the oblate density distribution for models considering equal values of total integrated mass-loss rates. We assume three values of a in Eq. 7.4 to generate the oblate shapes; $a = 0.9, 0.7$ and 0.5. Although the spherical symmetric case is modelled using Eq. 7.1, it will be addressed as the $a = 1$ case hereafter. An example of the modelled density distributions is shown in Fig. 7.1.

Once the geometry of the models is defined, the radiative transfer model is split in two stages. The first stage is to specify the gas temperature distribution throughout the CSE. In LIME it can be done defining the temperature as an analytical function of the coordinates of each particular model. However, we use the full 3-D radiative transfer code RADMC-3D (Dullemond 2012) to calculate the dust temperature considering the dust density distribution given by either case $a = 1$ or $a < 1$, assuming a gas-to-dust mass ratio of 1.0×10^2. The modelling of the dust has been performed using the standard dust opacity file provided by RADMC-3D, which is calculated from the optical constants of amorphous silicates (MgFeSiO4) taken from the Jena database (Jaeger et al. 1994, Dorschner et al. 1995) for dust grains particles with 0.1 μm radius. Hence, assuming that the dust grains and the molecular gas are fully coupled, the dust temperature is used as the input temperature for the LIME models of the molecular gas.

The second stage is the actual LIME model of the CO emission. It includes 40 radiative transitions of both ^{12}CO and ^{13}CO. The fractional abundance $f_{^{12}\mathrm{CO}}$ and the isotopic ratio ^{12}CO/^{13}CO values assumed

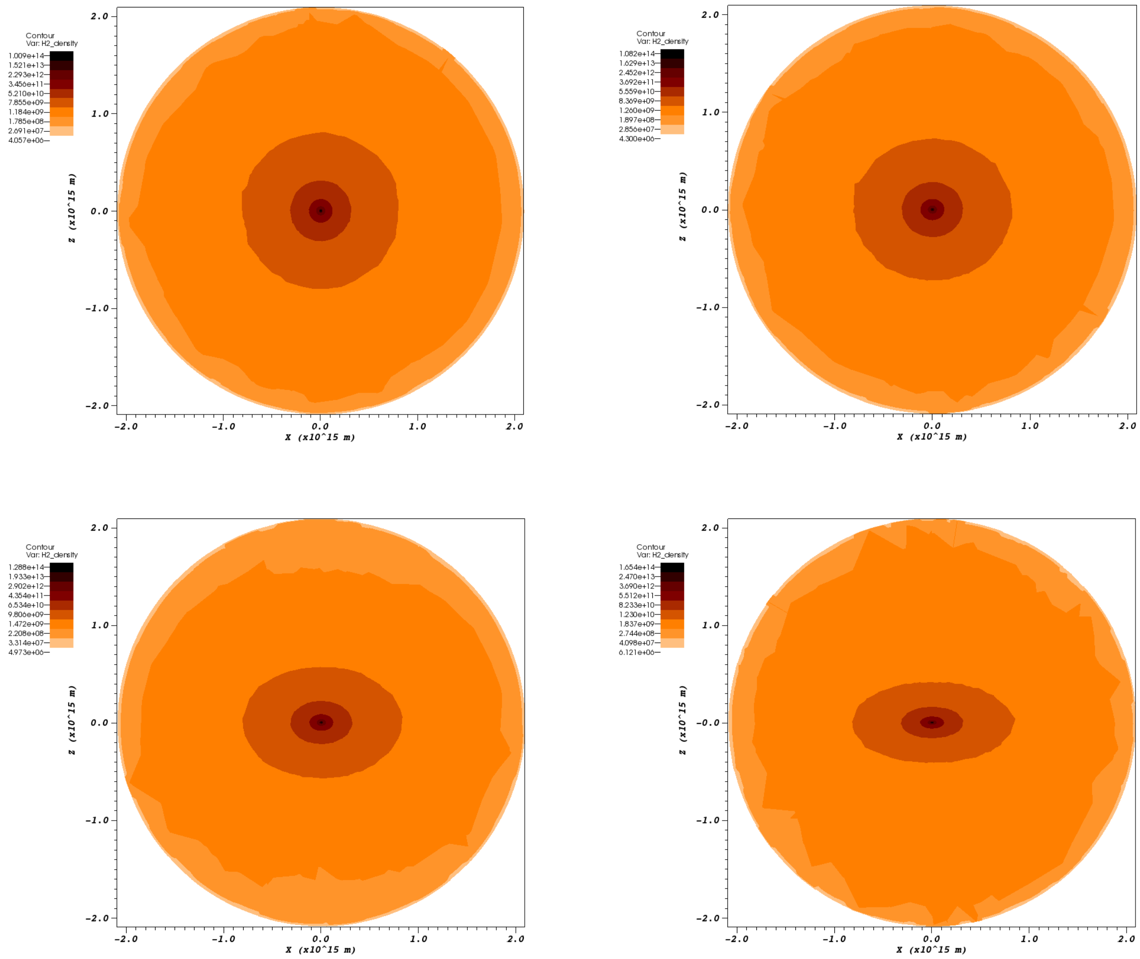

Figure 7.1: Density distribution projected on the X-Z plane for a synthetic source with $\dot{M} = 5 \times 10^{-5}$ $M_{\odot}yr^{-1}$. The spherical symmetric case (top left), $a = 0.9$ (top right), $a = 0.7$ (bottom left) $a = 0.5$ (bottom right).

Table 7.1: Model parameters.

a	0.5, 0.7, 0.9, 1.0
$\dot{M}$ [$M_\odot$ yr^{-1}]	5×10^{-7}, 5×10^{-6}, 5×10^{-5}
v_{exp} [km s^{-1}]	10, 15
D	150 pc, 1 kpc
$T_\star$	2000 K
$L_\star$	8300 $L_\odot$
R_{in}	20 AU
R_{out}	14000 AU
f_{CO}	$5{\times}10^{-4}$
$^{12}CO/^{13}CO$	20

are 5×10^{-4} and 20, respectively, which are within the range of the values that are usually reported in the literature. The values of the full set of parameters adopted in the models are listed in Table 7.1.
In order to analyze the spectral features of CO, each model includes the imaging of five rotational transitions in the ground vibrational state ($J = 1-0,\ 2-1,\ 3-2,\ 6-5,\ 15-14$) of both ^{12}CO and ^{13}CO. The images of the brightness distribution are calculated along three line-of-sight from the point of view of the observer: Face-on (X-Y plane), a rotation of 45° around the X-axis, and edge-on (X-Z plane). The images are data cubes of 400 channels along the line-of-sight velocity, centered at the systemic velocity of the source $v_{lsr} = 0$ km s^{-1}, with velocity (channel) resolution of 0.25 km s^{-1}. For illustration, the three images calculated for the $J = 3-2$ ^{12}CO transition for the case $a = 0.5$ are shown in the Fig. 7.2.

The spectral features of each rotational transition modelled are obtained after the convolution of the synthetic brightness distribution with a 2-D gaussian beam using the CASA task *imsmooth*. This allow us to simulate single-dish observations of the same synthetic source along the three line-of-sights modelled for each transition, assuming beam sizes of real radio telescopes at each frequency (see Table 7.2). Hence, the integrated intensities of the spectral lines obtained are calculated and compared.

Table 7.2: Beam sizes for the simulated observations.

Transition	beam size	Telescope
1-0	33"	*OSO*
2-1	21"	*JCMT*
3-2	14"	*JCMT*
6-5	8"	*JCMT*
15-14	12"	*HERSCHEL / HIFI*

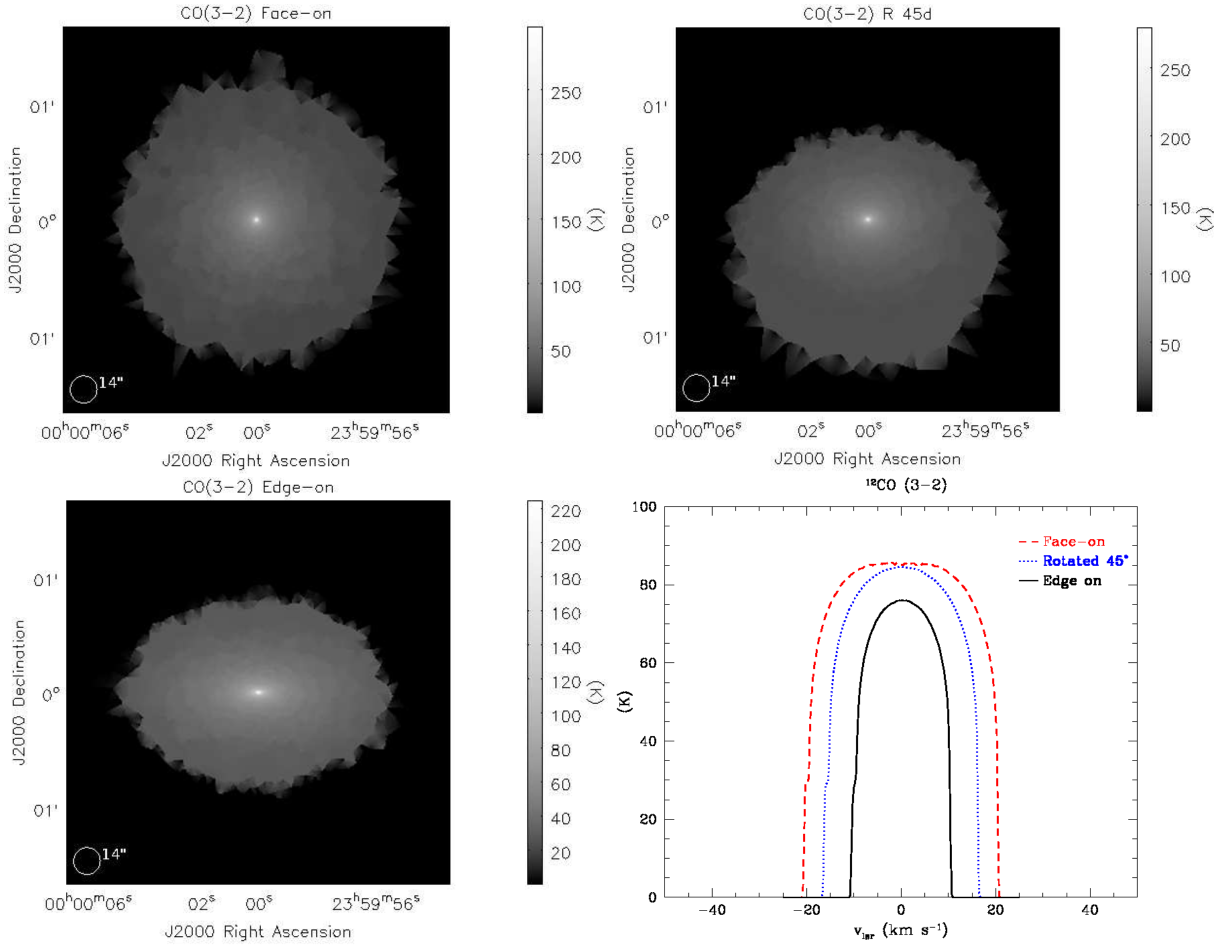

Figure 7.2: Image of the CO(3-2) transition calculated for $a = 0.5$, $\upsilon_{exp} = 10$ km s^{-1} and $\dot{M} = 5 \times 10^{-5}$ M$_{\odot}$ yr^{-1} for line-of-sight face-on (X-Y plane), rotated 45° around the X-axis and edge-on (X-Z plane). The bottom right panel shows the profile of the $J = 3-2$ ^{12}CO line emission for each line-of-sight for a simulated gaussian beam of 14" towards the center of the source.

7.2 Results

7.2.1 Line profiles

The line profiles obtained from observations towards AGB sources provides information about the optical depth of the transition along the line-of-sight towards the observed source, as well as of the relative size of the source with respect to the telescope beam (Olofsson et al. 1993). The line profiles obtained from our simulated observations towards the synthetic sources display characteristics of both spatially resolved and unresolved; optically thin and optically thick emission. In fact, optically thin, spatially resolved emission (double-peaked features) is usually observed for the three lower energy transitions modelled, but mostly towards the synthetic sources with low mass-loss rate. Flat-topped profiles, which corresponds to optically thin, spatially unresolved emission are also observed, mostly for the source at

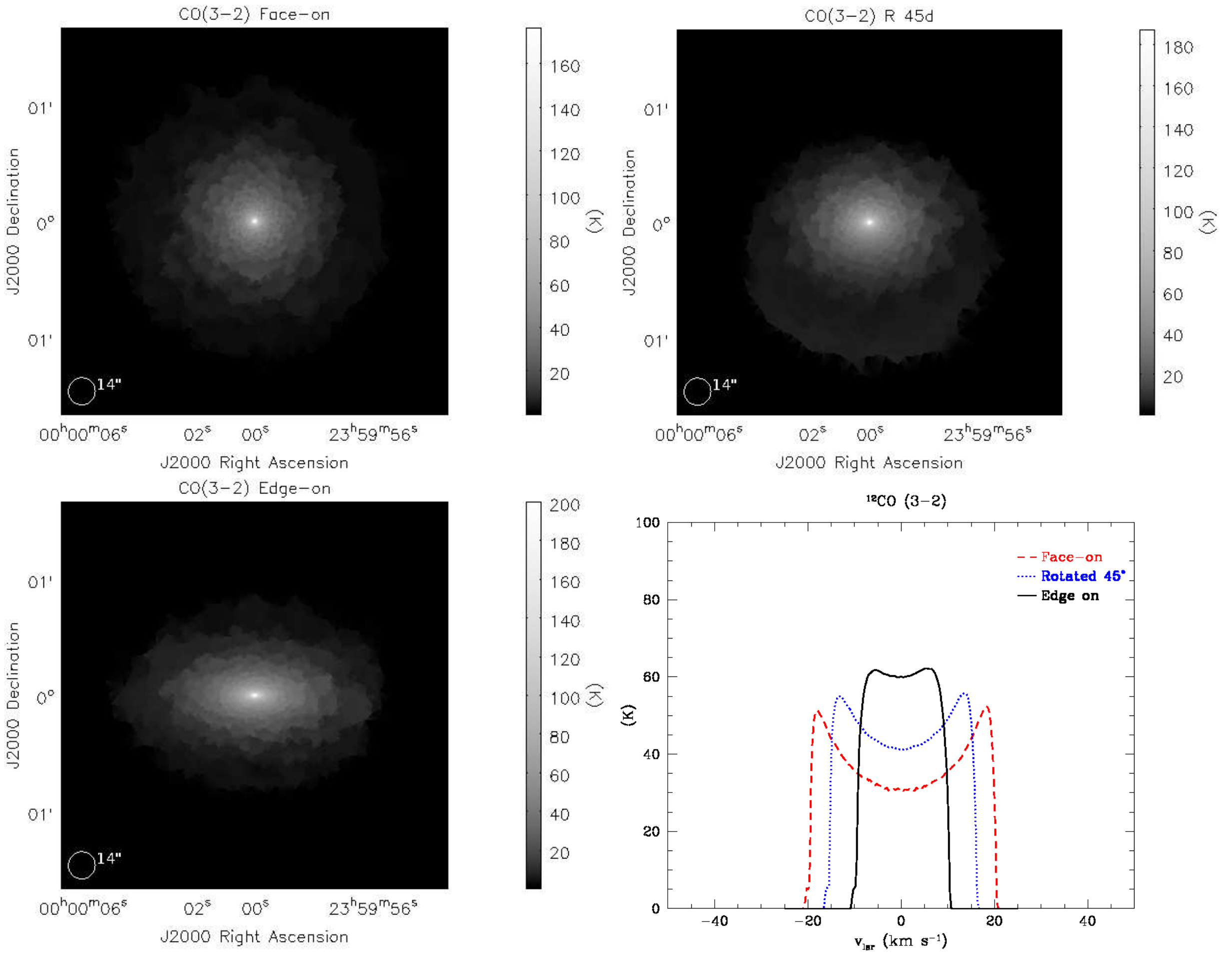

Figure 7.3: Image of the CO(3-2) transition calculated for $a = 0.5$, $v_{exp} = 10$ km s^{-1} and $\dot{M} = 5 \times 10^{-6}$ M$_\odot$ yr^{-1} for line-of-sight face-on (X-Y plane), rotated 45° around the X-axis, and edge-on (X-Z plane). The bottom right panel shows the profile of the $J = 3-2$ ^{12}CO line emission for each line-of-sight for a simulated gaussian beam of 14" towards the center of the source.

1 kpc in the three lower transitions modelled; whereas for the source at 150 kpc, it is observed for the J=6→5 transition in some cases. The triangular line profile is also common for the source at 1 kpc, whereas for the source at 150 pc it is only observed in the J=15→14 transition. Such line profile is indicative of optically thick, spatially unresolved emission.
Besides the changes on the line profile, the most common effect seen for all the lines is the increase of the observed peak flux when the mass-loss rate increases from $\dot{M} = 5 \times 10^{-7}$ M$_\odot$ yr^{-1} (hereafter $\dot{M}_{-7}$) to $\dot{M} = 5 \times 10^{-5}$ M$_\odot$ yr^{-1} (hereafter $\dot{M}_{-5}$) as expected.

In the case of the synthetic sources with different degrees of oblateness, observing along the three line-of-sight results in spectral features covering different velocity ranges. For observations along the minor axis ($\theta = 0$), the component of the expansion velocity along the line-of-sight is scaled by a factor of $1/a$, whereas for observations at $\theta = \pi/4$, the component of the expansion velocity along the line-of-sight is given by

$$v_{\pi/4} = \frac{v_{exp}}{a} \cos\left(\frac{\pi}{4}\right) \sqrt{1 + a^2}. \quad (7.6)$$

Observations along the major axis (at $\theta = \pi/2$) yield spectral lines covering the same velocity range than the lines obtained from the observations towards the spherically symmetric case. Furthermore, the three spectral features obtained for each transition corresponding to observations along the different line-of-sight exhibit different peak-flux values, whose differences increase for the most oblate sources. Therefore, is important to calculate the velocity integrated intensity for each spectral line ($I = \int T_{mb}\, dv$) observed along each line-of-sight in order to learn whether the emission is affected by the oblateness of the source. Moreover, the velocity integrated intensity is a parameter that is involved in the calculations of the mass-loss rate towards the CSEs of AGB stars.

The spherical symmetric case

The spectral features obtained from the simulated observations towards the spherical CSEs are shown in Fig. 7.4 for the two assumed distances, with the beam sizes from Table 7.2. In the case of the source at 150 pc, only the J=1→0 transition display double-peaked line-profiles for all the different mass-loss rates, whereas the line profile of the J=2→1 and the J=3→2 transitions change as a function of the mass-loss rate from optically thin to optically thick, both spatially resolved emission. The J=6→5 transition displays a line profile that corresponds to optically thin, spatially unresolved emission for the $\dot{M}_{-7}$ source, whereas for the $\dot{M}_{-6}$ source the line profile corresponds to partially resolved emission. Although the line profile is not as pronounced as for the $\dot{M}_{-5}$ source, where the emission is spatially resolved, the profile of the line for the $\dot{M}_{-6}$ and $\dot{M}_{-5}$ sources indicate that the emission is optically thick. In the case of the J=15→14 transition, the observations result in optically thick, spatially unresolved emission, and the only apparent changes between the different mass-loss rate sources is the value of the peak flux and the smoother line profiles for the higher mass-loss rate sources.
In the case of the source with distance of 1 kpc, the only partially resolved features are those observed in the J=2→1, J=3→2 and J=6→5 transitions for the $\dot{M}_{-5}$ source. The features observed in this case corresponds to optically thick emission. Spatially unresolved emission is observed for the J=15→14 and the J=1→0 for all cases; the former being optically thick and the latest optically thin for the three mass-loss rate values considered. Observations along the different line-of-sight yield similar spectral features, as is expected.

The slightly oblate CSE case: a = 0.9

In Fig. 7.5 are shown the line profiles obtained from simulated observations of ^{12}CO emission towards the synthetic CSEs whose density distribution resembles an ellipsoid with a ratio between the major axis (either the x- or y-axis) and the minor axis (z-axis) of a = 0.9, assuming that the distances to the

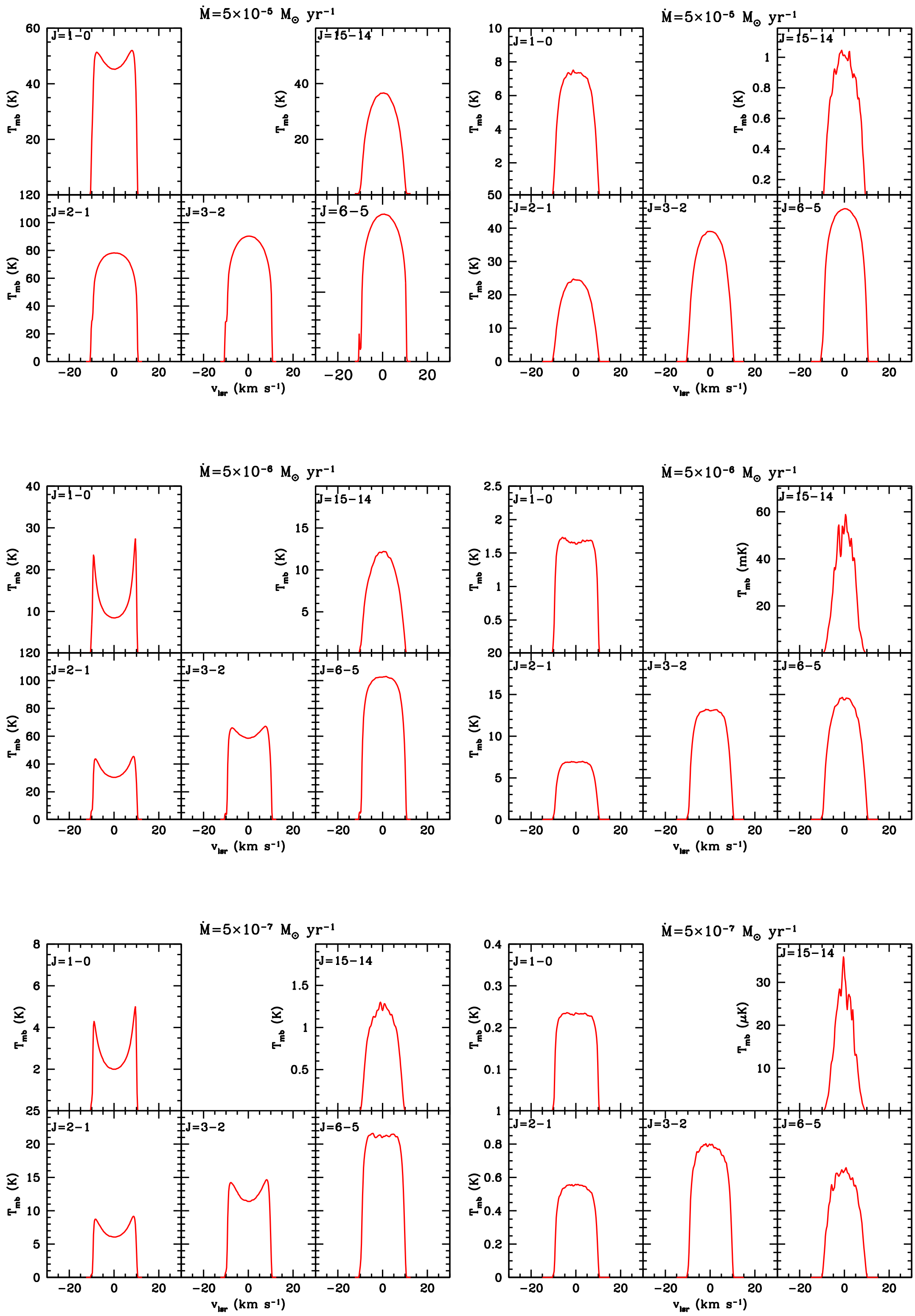

Figure 7.4: Spectral features of the different transitions modelled for the a = 1.0 case. The different panels show the line profile obtained from the simulated observations towards sources with different mass-loss rates at 150 pc (left) and 1 kpc (right).

source are 150 pc and 1 kpc. Observing along the minor axis results in spectral features whose width is 22.2 km s^{-1}, while observations at $\theta = \pi/4$ results in spectral features 21.2 km s^{-1} wide. The simulated observations along the major axis result in the most narrow spectral features, covering a velocity range of 20.0 km s^{-1}.
In the optically thin limit, the lines observed along the major axis display higher peak-flux values, different from the optically thick case ($\dot{M}_{-5}$), where the wider spectral features also exhibit higher peak flux values than the narrow ones. For all the mass-loss rate values, the profile of the spectral features of each individual transition does not change as a function of the line-of-sight, i.e. the spectral features of the same transition display characteristics of either optically thin or optically thick; spatially resolved or unresolved emission along the three line-of-sights considered. The only exception seems to be the J=1→0 transition observed towards the $\dot{M}_{-5}$ source at 1 kpc, whose emission exhibit a more pronounced line profile along the major axis than along the minor axis of the oblate ellipsoid. In this case, the emission shows a hint of being optically thick, spatially unresolved emission along the major axis, whereas along the other two line-of-sights the line profile is more flat-topped than triangular. In contrast, the counterpart emission towards the source at 150 pc exhibits line profiles which corresponds to optically thin emission along the three line-of-sights. In the case of the closest source, the emitting region of the J=1→0 transition is far too extended compared to the size of the 2-D gaussian kernel (beam) used to convolve the brightness distribution. Therefore, the emission observed along the different axis may trace regions with similar temperature distribution. On the other hand, because the beam size is comparable with the extension of the J=1→0 emission towards the most distant source, the observations along the different line-of-sights trace more extended regions where the difference on the temperature distribution as a function of the distance to the star becomes relevant. For the other lines, the difference introduced by the distance to the observed source is related, as expected, to the peak flux observed. In addition, those optically thin, spatially resolved features observed towards the source at 150 pc become optically thin, spatially unresolved emission for the more distant source, as would be also expected. The J=15→14 transition shows a more irregular line profile towards the source at 1 kpc than towards the closest one.

The $a = 0.7$ case

In Fig. 7.6 are shown the line profiles obtained from the simulated observations towards oblate synthetic source with ratio between the major and the minor axis $a = 0.7$. The velocity ranges of the spectral features observed at $\theta = 0$ and $\theta = \pi/4$ are 28.6 km s^{-1} and 24.7 km s^{-1} respectively, whereas along the major axis it is 20 km s^{-1}, similar to the spherical case.
In the case of the closest source, all the features of the four lower energy transition correspond to optically thin emission when observed towards the lowest mass-loss rate ($\dot{M}_{-7}$) source. For the three lower transitions the simulated observations yield spatially resolved spectral features along the three

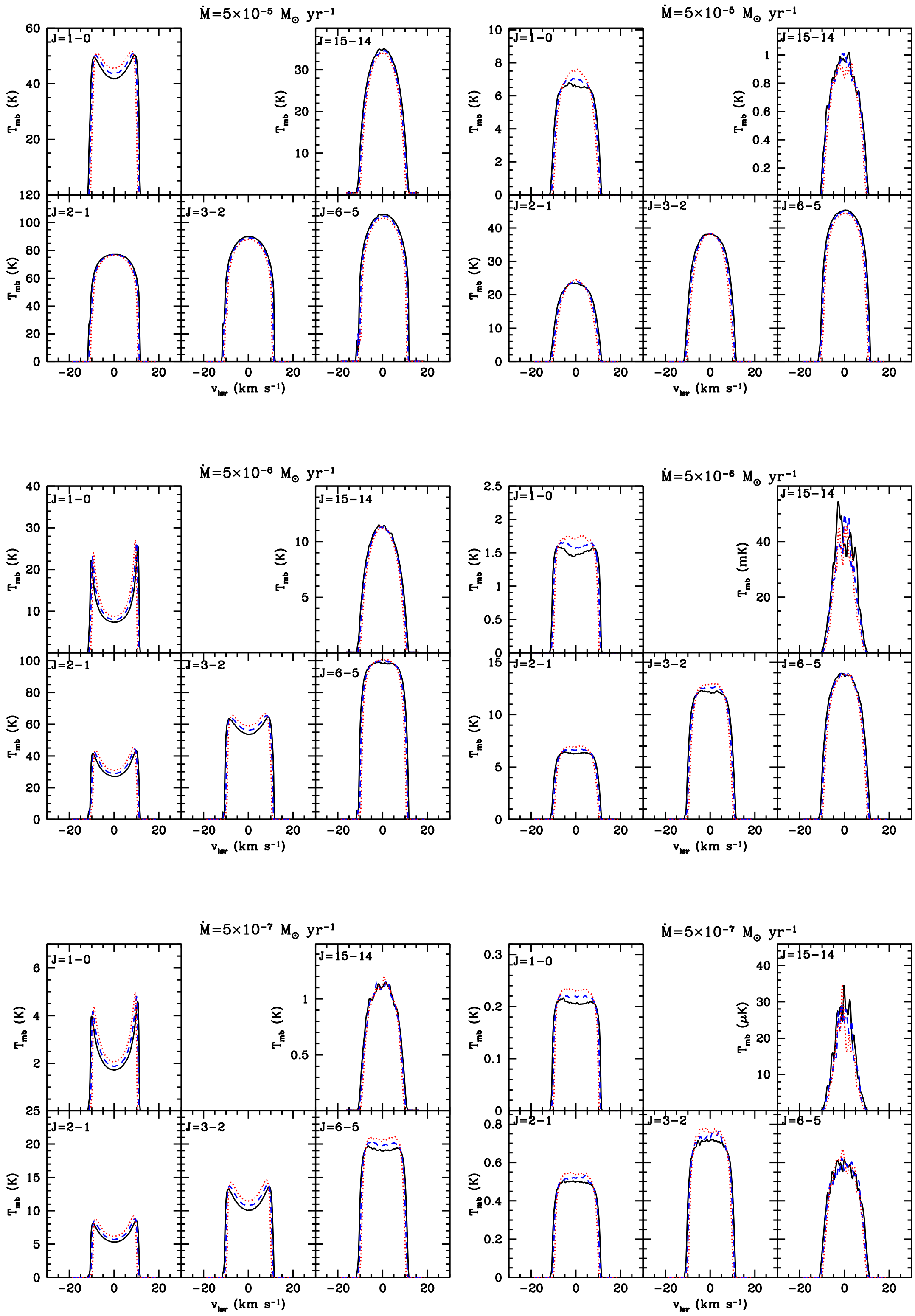

Figure 7.5: Spectral features of the different transitions modelled for the $a = 0.9$ case assuming distances to the source of 150 pc (left) and 1 kpc (right). The dotted (red) and dashed (blue) lines show the spectral features obtained from simulated observations at $\theta = \pi/2$ and $\theta = \pi/4$, while the solid line shows the line profile for observations at $\theta = 0$.

line-of-sights. In the case of the J=6→5 lines, the profile of the lines for the different line-of-sights are slightly different. Along the major axis the line profile is flat-topped, indicative of spatially unresolved emission. At $\theta = \pi/4$ the emission is still spatially unresolved, but at $\theta = 0$ a tentative double-peaked feature appears.
For the most distant synthetic source with the lowest mass-loss rate modelled, the line profiles observed in the three lower energy transitions also correspond to optically thin emission. In the case of the J=6→5, the line profiles becomes irregular and display similar peak-flux values along the three line-of-sights. The differences of the line profiles observed along the different line-of-sights are more clear for the J=15→14 transition, where the peak-flux observed along the major axis is about a factor of 3 lower than along the minor axis.

The simulated observations towards the closest source with $\dot{M}_{-6}$ yield spectral features which correspond to spatially resolved emission along the three line-of-sights for the three lower energy transitions modelled. The J=15→14 transition already shows characteristics of spatially unresolved emission, with lower peak-flux value for the narrower feature (observed along the major axis) than the peak-flux of the broader emission (observed at $\theta = 0$). The J=6→5 transition display differences on the line profile that can be related to spatially unresolved, optically thin emission at $\theta = 0$, and to spatially resolved, optically thick emission at $\theta = \pi/2$.
Observing towards the more distant source results in different line profiles along the different line-of-sights. Such change is more evident in the J=1→0 case, where the observations along the minor axis exhibit a clear double-peak line profile, different from the parabolic profile observed along the major axis. In the case of the J=2→1 and J=3→2 transitions, the emission seems to be partially resolved, optically thin emission along the minor axis; and spatially unresolved, optically thin emission along the $\theta = \pi/4$ direction. In contrast, observing along the major axis results in a smooth parabola profile for the J=2→1.

From the simulated observation towards the synthetic sources with $\dot{M}_{-5}$, the line profiles of the J=3→2 and J=6→5 transitions corresponds to optically thick emission for both sources at 150 pc and 1 kpc. Although their line profiles are similar along the three line-of-sights for the closest source, the J=3→2 lines observed towards the more distant source yield a line profile which is more flat-topped than the one along the major axis. The J=1→0 and the J=2→1 transitions show clear differences for observations along the different line-of-sights towards the source at 1 kpc. Both display triangular features which corresponds to optically thick, spatially unresolved emission from the observations along the major axis, whereas along the minor axis, the line profiles correspond to optically thin emission.

The $a = 0.5$ case

In Fig. 7.7 we show the spectral features obtained from the simulated observations towards the oblate synthetic CSEs with major and minor axis ratio $a = 0.5$. The spectral velocity range for the three different line-of-sights are 40 km s^{-1} at $\theta = 0$; 31.6 km s^{-1} at $\theta = \pi/4$, and 20.0 km s^{-1} at $\pi/2$.

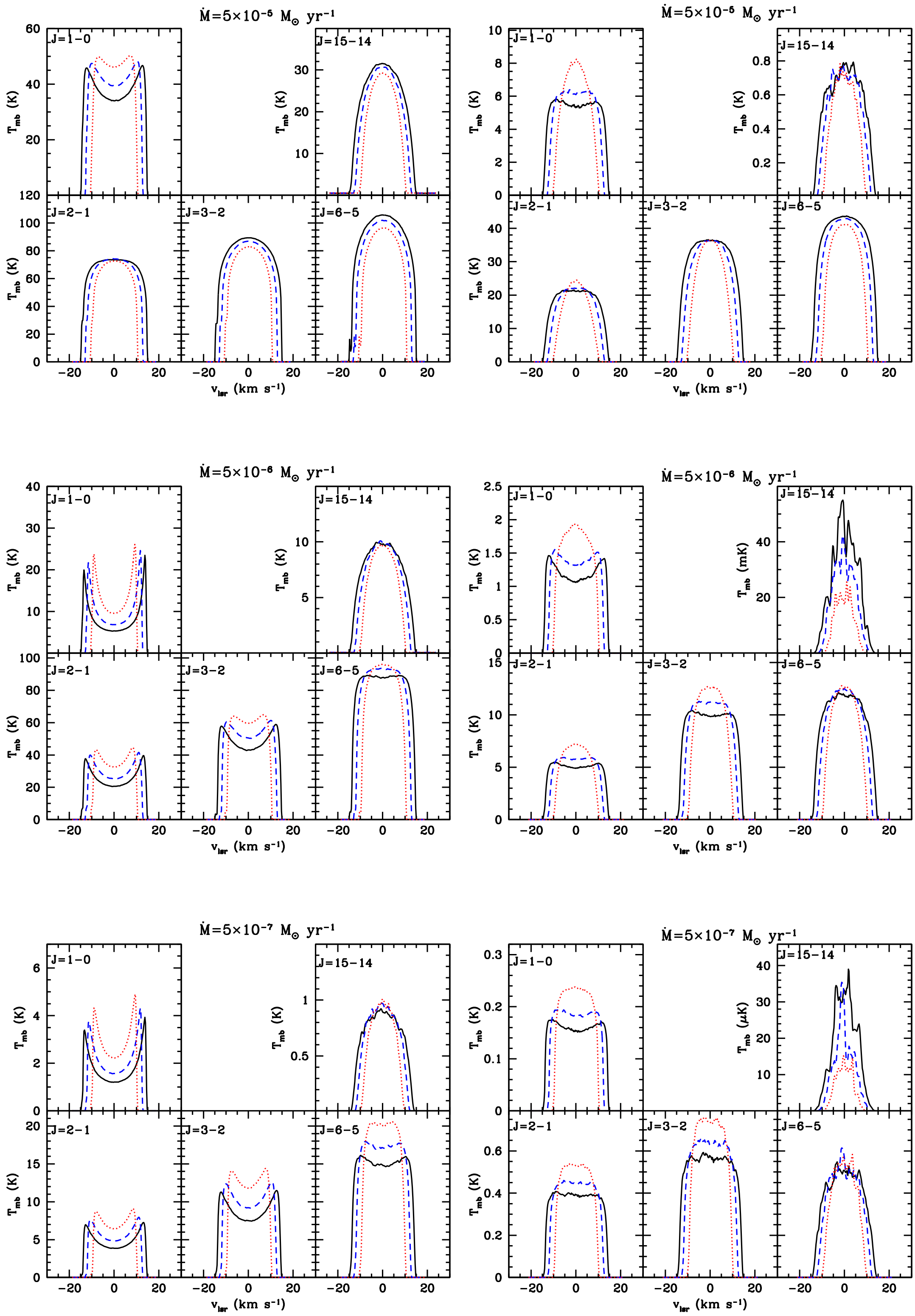

Figure 7.6: Spectral features of the different transitions modelled for the $a = 0.7$ case assuming distances to the source of 150 pc (left) and 1 kpc (right). The dotted (red) and dashed (blue) lines show the spectral features obtained from simulated observations at $\theta = \pi/2$ and $\theta = \pi/4$, while the solid line shows the line profile for observations at $\theta = 0$.

For the closest source with $\dot{M}_{-7}$, the three lower energy transition modelled display line profiles which correspond to optically thin, spatially resolved emission along the three line-of-sights. In the case of the J=6→5 transition, the line profile corresponds to spatially unresolved emission at $\theta = \pi/2$, different from the observations along the minor axis, where the line exhibits a double-peaked profile. At $\theta = \pi/4$ the profile also corresponds to spatially unresolved, optically thin emission, although a hint of a double-peaked profile can also be seen. The line profiles of J=15→14 in the $\dot{M}_{-7}$ source are also different along the different line-of-sights. At $\theta = \pi/2$ and $\theta = \pi/4$ the line profiles have the triangular shape corresponding to optically thick, spatially unresolved emission. At $\theta = 0$ the line profile obtained is less pronounced at the top, which could be an indicative of optically thin, spatially unresolved emission.
For the $\dot{M}_{-7}$ at a distance of 1 kpc, there are more evident differences between the line profiles observed along the three line-of-sights, and in particular for the J=1→0 and the J=15→14 transitions. The former exhibit well defined double-peaked profiles for observations at $\theta = 0$ and $\theta = \pi/4$, while along the major axis the line profile becomes triangular. In the case of the J=15→14 line, the difference between the line profiles observed along the different line-of-sights is evident in the peak-flux of the lines observed, although such difference is reduced as the mass-loss increases.
The line profiles observed towards the closest $\dot{M}_{-6}$ source for the J=1→0 transition correspond to optically thin, spatially resolved emission along the different line-of-sights. It is also the case for the J=2→1 and the J=3→2 transitions. In the latest, the line profile observed along the major axis shows a double-peaked profile, but it is clear that it is less optically thin than along the $\theta = \pi/4$ and $\theta = 0$. The simulated observations of the J=6→5 transition results in different line profiles along the three line-of-sights. At $\theta = 0$ the emission observed is optically thin, spatially resolved. At $\theta = \pi/4$ the line profile corresponds to optically thin, spatially unresolved emission, whereas at $\theta = \pi/2$ the emission observed is optically thick, spatially resolved. For the J=15→14 transition, the lines have roughly the same peak-flux. Their profile correspond to spatially unresolved emission. At $\theta = \pi/2$ the triangular shape of the line is more obvious than along any other direction, indicating that the transition is optically thick. At $\theta = \pi/4$ the line profile is less pronounced, but it likely corresponds to optically thick rather than to optically thin emission. At $\theta = 0$ the profile is rather rounded, indicating that in this case the emission is more spatially resolved. Again, the differences between the line profiles observed along the three line-of-sights are more evident towards the source at 1 kpc. However, the line profiles obtained along the minor axis and at $\theta = \pi/4$ are the same despite the distance to the source, while along the major axis, the line profiles obtained towards the more distant source correspond to optically thick, spatially unresolved emission.

For the closest $\dot{M}_{-5}$ source, the line profiles of the four lower transitions corresponds to spatially resolved emission, while the line profile of the J=15→14 transition corresponds to spatially unresolved, optically thick emission. Regardless the J=1→0 transition, the line profile of all the lines observed at $\theta = \pi/2$ are optically thick. At $\theta = \pi/4$, the J=2→1 transition exhibits a profile between flat-topped and a smooth-parabola, while for the higher transitions the latest is better defined. At $\theta = 0$, the shape of the lines correspond to optically thin emission for the J=1→0 and J=2→1, and to optically thick for the

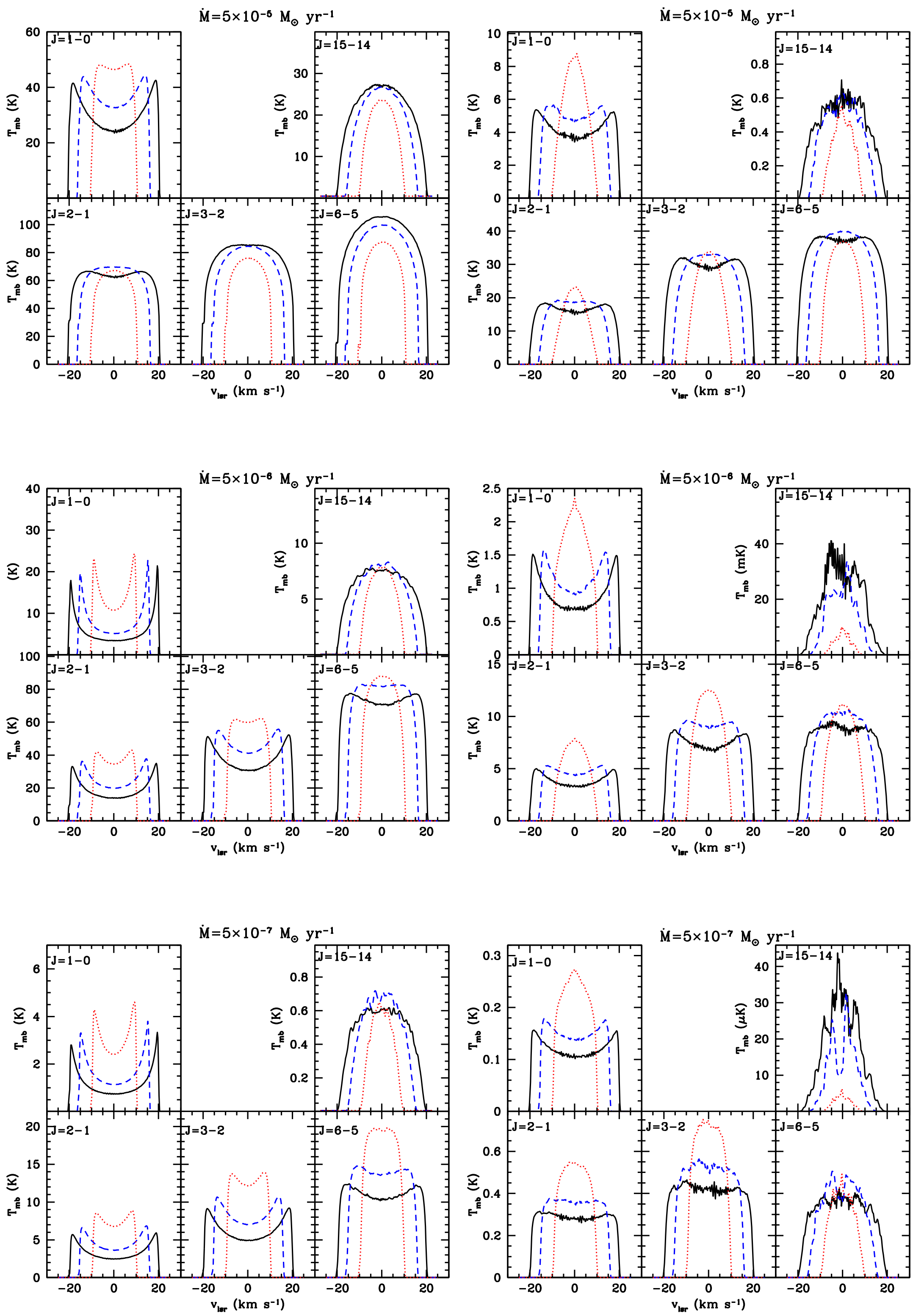

Figure 7.7: Spectral features of the different transitions modelled for the $a = 0.5$ case assuming distances to the source of 150 pc (left) and 1 kpc (right). The dotted (blue) and dashed (red) lines show the spectral features obtained from simulated observations at $\theta = \pi/2$ and $\theta = \pi/4$, while the solid line shows the line profile for observations at $\theta = 0$.

J=6→5 transition. The line profile of the J=3→2 is between the smooth-parabola and the flat-topped profile. For the more distant source, all the observations along the major axis yield optically thick, spatially unresolved features. In contrast, the line profiles along the minor axis exhibit double-peaked profiles, with the exception of the J=15→14 transition.

7.3 Analysis

As mentioned above, the line profiles obtained from radio observations provide useful information about both the expansion velocity and the size of the emitting region relative to the beam size of the telescope. The low-energy CO transitions trace the most extended regions of the CSEs, whereas the higher transitions trace their innermost regions. Multi-transition observations towards the CSEs are performed in order to estimate the mass-loss rate of the observed sources (e.g. Olofsson et al. (1993), Schöier and Olofsson (2001), Decin et al. (2007), Ramstedt et al. (2008)). In general, the radiative transfer models combine the fitting of both the spectral line profiles and the velocity-integrated intensity in order to estimate the mass-loss rate of the observed sources. However, because the calculated line profiles are sensitive to small changes on different parameters used in the radiative transfer models, detailed fits to the observed line profiles of each single transitions are rarely achieved. In addition, the estimated uncertainties introduced by the calibration process itself on the measured integrated intensities is around 20%, even for observed data sets with high signal-to-noise ratios (Schöier and Olofsson 2001). This together with the degeneracy of the parameter space make the determination of the mass-loss rates of AGB sources to be a rather complex case.

The results from our simulated observations towards the synthetic sources suggest two different situations depending on whether the emission is spatially resolved or not. In the case of the spatially resolved emission, the profiles of the spectral features (regardless the width and the peak intensity) do not change as a function of the line-of-sight, i.e. either double-peaked, flat-topped, or parabolic profiles are observed for the same transition along the different line-of-sights. This is particularly true for the three lower-energy transitions modelled ($J_u \leq 3$) and can be seen even for the most oblate source modelled (a = 0.5). This suggest that the most significant errors on the calculated mass-loss rate value obtained from fitting the line profile relies on the parameters that account for the width and peak-flux of the observed line, rather than on both the radial density and temperature distribution, and on the optical depth of the observed transition inferred from the line shape. Therefore in the spatially resolved case, fitting the line profiles assuming a spherically symmetric model could yield fair mass-loss rate estimates whose reliability relies on the fit of the measured integrated intensity and on the errors intrinsic to the parameter space of the model itself.

In order to investigate the effect induced by the oblateness on the velocity-integrated intensity (I) measured towards the synthetic sources, I is calculated from the spectral features obtained from the simulated observations towards the oblate sources and compared with the integrated intensities measured towards their spherical counterparts (I_{sph}). The results are shown in Fig. 7.8, where the integrated intensities measured along the different line of sights (I_0 observing along the minor axis, I_{45} observing along the direction defined by $\theta = \pi/4$, I_{90} observing along the major axis) are normalized with the measured value for the spherical case (I_{sph}). In the case of the resolved sources, the differences between the measured I_i ($i = 0, 45, 90$) for each transition increases with the mass-loss rate of our modelled synthetic objects. The largest difference is always seen towards the $\dot{M}_{-5}$ source, where with exception of the J=1→0, the spectral profiles observed correspond to optically thick emission along the different line-of-sights. Moreover, the differences between the integrated intesities measured along the different line-of-sights increases with the J_u of the rotational transitions. The differences between the integrated intensity measured for the transitions with $J_u \leq 6$ along the different line-of-sights towards the $\dot{M}_{-7}$ source are not larger than 10% with respect to I_{sph}, even for the more oblate synthetic sources. In the case of the most oblate source with $\dot{M}_{-6}$, the largest difference between I_i and I_{sph} for the transitions with $J_u \leq 3$ is measured along the minor axis, where I_0 is 25% larger than I_{sph} for the J=3→2, whereas for the J=1→0 and J=2→1 the difference with I_{sph} is not larger than 20%.

The scenario is different for the two higher J_u transitions of our models. Although for the $a = 0.9$ source with $\dot{M}_{-6}$ the difference with respect to the spherical case is not larger than 10% for both the J=6→5 and the J=15→14, the difference increases for the more oblate sources. In the $a = 0.7$ case, the measured I_0 for the J=6→5 transition is 40% and 30% larger than I_{90} and I_{sph}, respectively, and becomes even larger for the source with $a = 0.5$ ($I_0/I_{90} \sim 1.75$ and $I_0/I_{sph} \sim 1.55$). Therefore, fitting the velocity-integrated intensity of rotational transitions of CO with $J_u \leq 6$ towards resolved sources with $\dot{M} < 10^{-6}$ M$_\odot$ yr^{-1} could yield reliable results even if the source is assumed spherically symmetric. For sources with higher mass-loss rates, fitting the integrated intensity measured from rotational transitions with $J_u \leq 3$ assuming that the source is spherically symmetric could still yield reliable values for oblate sources with minor-to-major axis ratio ≥ 0.7. However, such assumption could lead to significant errors on the mass-loss rate estimated from fitting the velocity-integrate intensity measured from higher J transitions of CO.

The velocity-integrated intensities measured along the different line-of-sights towards the more distant synthetic sources are also compared with the measurements done towards their spherical counterpart. Notices that, in this case, observing along the minor axis yields a larger integrated intensity value with respect to both I_{45} and I_{90} in all the cases, whereas observing along the major axis results in the lowest value. The ratio formed by I_0/I_{90} increases with both the J_u number of the transition and the oblateness of the source. The largest difference is measured towards the $\dot{M}_{-5}$ source for the transitions with $J_u \leq 6$. In fact, observing along the minor axis towards the $\dot{M}_{-5}$ source with minor-to-major axis ratio $a = 0.7$ results in I_0 being 20% higher than I_{sph} in the J=1→0 transition, whereas $I_0/I_{sph} \sim 1.4$ for the other transitions with $J_u \leq 6$.

In the case of the $\dot{M}_{-6}$ and $\dot{M}_{-7}$ sources with $a = 0.9$, $I_i/I_{sph} \sim 1$ for the J=1→0 transition, while for the other transitions with $J_u \leq 6$ the largest difference with respect to the spherical case is lower than 10%. For the more oblate sources the J=2→1 and J=3→2 transitions appears to be more sensitive to the oblateness than towards the closest source. It may be related to the fact that the line profiles

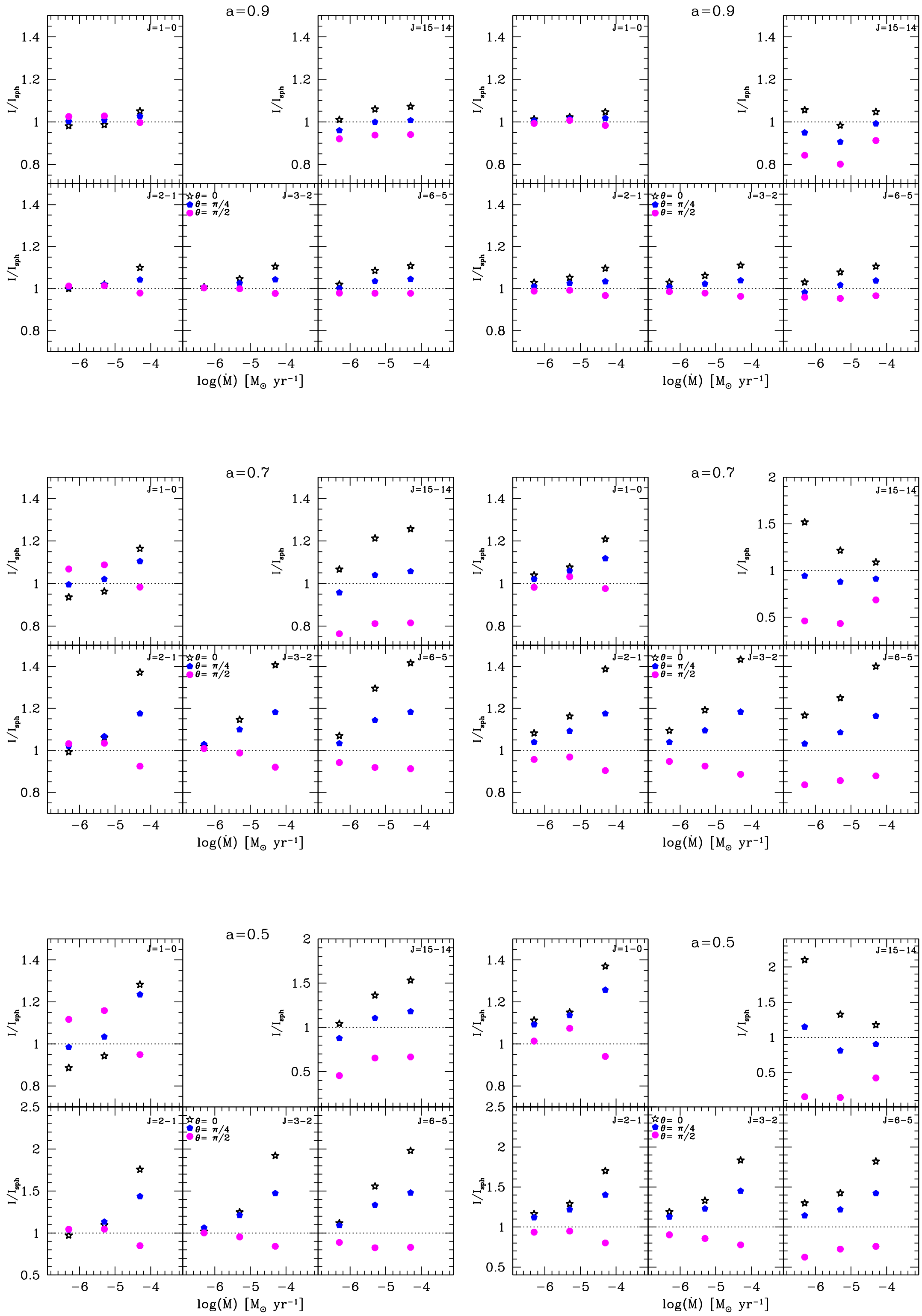

Figure 7.8: Integrated intensity values measured for the different mass-loss rates values considered in our models, for the two distances assumed, (left) 150 pc and (right) 1 kpc. The values presented are normalized with the integrated intensities measured for each transition for the $a = 1$ case.

along the different line-of-sights correspond to either optically thin emission (along the minor axis) or optically thick emission (along the major axis). In the case of the oblate source with minor-to-major axis ratio $a = 0.7$, the difference between I_0 and I_{90} is about 15% towards $\dot{M}_{-7}$, but not larger than 10% the I_{sph}. For the J=6→5 transition, the difference on the measured integrated intensity by observing along the minor and major axis is about ∼ 35%, whereas with respect to the spherical case the differences are about 20%. Therefore, the fact that observing along the different line-of-sights yields such differences on the velocity-integrated intensity may be reflected on the mass-loss rate values that could be estimated from fitting the integrated intensity measured towards an observed source. Different from the spatially resolved case where the differences between the line profiles is only minor (compared to the spatially unresolved case) and the emitting region traced is consistent along the three line-of-sights, the interplay between fitting both the velocity-integrated intensity and the shape of the line may lead to a large uncertainty range on the case of the synthetic unresolved sources.

In order to estimate the difference between the mass-loss rate derived from fitting the velocity-integrated intensity from the observations along the different line of sights, we use the formula derived by Ramstedt et al. (2008)

$$\dot{M} = s_J (I_{CO} \theta_b^2 D^2)^{a_J} v_e^{b_J} f_{CO}^{-c_J}, \tag{7.7}$$

where $\dot{M}$ is given $M_\odot$ yr^{-1}, θ_b is the telescope's beam size, D is the distant to the source, v_e the expansion velocity of the CSE and f_{CO} the fractional abundance of the CO molecule. The parameters s_J, a_J, b_J and c_J were obtained from fitting the Eq. 7.7 to the output of their radiative transfer models calculated for a grid of 60 sample stars (Ramstedt et al. 2008). According to the autors this formula only applies to unresolved emission, and the values of the parameters mentioned above are valid within the ranges $10^{-7} \leq \dot{M} \leq 10^{-5}$ $M_\odot$ yr^{-1}, $5 \leq v_e \leq 20$ km s^{-1}, $10^{-4} \leq f_{CO} \leq 10^{-3}$ (see the Table A1 in their paper). Because the results of Eq. 7.7 are consistent with the results of their 1-D Monte Carlo radiative transfer code, we use it in order to estimate the mass-loss rate from the velocity-integrated intensity measured along the different line-of-sights. Given that the expansion velocity obtained from the spectral profiles detected along the major axis is the same than in the spherical case, the comparison between the mass-loss rates is straightforward in this particular case. Thus

$$\frac{\dot{M}_{90}}{\dot{M}_{sph}} = \left(\frac{I_{90}}{I_{sph}}\right)^{a_J}, \tag{7.8}$$

allows to estimate the mass-loss rates assuming that the source is spherically symmetric, and then compare it with the spherically symmetric counterpart. For the synthetic object with $a = 0.9$, using the I_{90} measured for the J=3→2 towards the $\dot{M}_{-6}$ source and $a_J(J = 3 \rightarrow 2) = 0.91$, the mass-loss rate estimated is only ∼ 1.8% lower than the mass-loss rate of the spherically symmetric source. In other words, assuming that the oblate source with $a = 0.9$ is spherically symmetric and then fitting the measured I_{90}, lead to slightly underestimate its mass-loss rate if it is estimated using the J=3→2 transition. The integrated intensities measured for the J=2→1 and J=1→0 along the major axis yield similar values than the observations towards the spherical source. Hence, assuming that the source is spherically symmetric yield accurate estimates of the mass-loss rate for the slightly oblate, unresolved synthetic sources.

In the case of the oblate source with $a = 0.7$, using the integrated intensities for the three lower transitions measured along the major axis towards the $\dot{M}_{-6}$ source results in mass-loss rates that are 1.9% higher (J=1→0), and 2.7% (J=2→1) and 6.7% (J=3→2) lower than the spherical case. Furthermore, in the case of the more oblate source ($a = 0.5$), the mass-loss rate estimated using the J=1→0 is 4.7% higher than I_{sph}, while for J=2→1 and J=3→2 it is 4.3% and 12.9% lower, respectively. Because the ratios I_{90}/I_{sph} are in general closer to the unity for the $\dot{M}_{-7}$ source than for the higher mass-loss rate sources, fitting the velocity-integrated intensity of CO rotational transitions with $J_u \leq 3$, and assuming that the source is spherically symmetric, could yield reliable estimates of the mass-loss rate. Therefore, a (conservative) uncertainty range for observations along the major axis will be 20% for the synthetic sources with $\dot{M} < 5 \times 10^{-6}$ M$_\odot$ yr^{-1}. On the other hand, because the ratio formed by I_{sph} and I_{90} increases for the sources with higher mass-loss rates, to assume the source as spherically symmetric can lead to underestimate the mass-loss rate of the source by larger factors than 20%.

Observing along the minor axis and the direction defined by $\theta = \pi/4$ result in higher integrated intensity values than along the major axis. Thus, in principle, fitting the integrated intensity measured along the major axis towards our synthetic sources, for instance, will lead us to derive a different mass-loss rate value, higher than the estimated value along the major axis for oblate sources with $a \leq 0.7$.
When a circumstellar envelope is observed, the expansion velocity of the emitting region is derived from the width of the spectral features detected. Hence, the CSEs are assume to be spherically symmetric, and half the width of the line profile to be its overall expansion velocity. Then, given that the line-of-sight velocity for the observations along the minor axis and along the direction defined by $\theta = \pi/4$ are scaled by $1/a$ and by the expression in Eq. 7.6, respectively, we used Eq. 7.7 in order to calculate the velocity-integrated intensity for a source with $\dot{M} = 5 \times 10^{-6}$ M$_\odot$ yr^{-1} from the CO rotational transitions with $J_u \leq 3$

$$I_{CO} = \frac{\dot{M_{sph}}}{\theta_b^2 D^2 (s_J v_e^{b_J} f_{CO}^{-c_J})^{1/a_J}}. \tag{7.9}$$

This allow us to compare the mass-loss rate estimated for a spherical source, whose v_e is inferred from the line profile observed towards the oblate sources, with the mass-loss rate estimated using I_0. Observations along the minor axis yield spectral features 28.6 km s^{-1} wide for the source with $a = 0.7$, which implies that the expansion velocity of the observed source is $\sim$ 14.3 km s^{-1}. Hence, from the expression

$$\dot{M}_0 = \left(\frac{I_0}{I_{CO}}\right)^{a_J} \dot{M}_{sph}, \tag{7.10}$$

the mass-loss rate estimated using the integrated intensity measured along the minor axis for the J=3→2 transition towards the oblate source with $\dot{M}_{-6}$ is ~ 70% higher than the value estimated for a spherically symmetric source whose expansion velocity is ~ 14.3 km s^{-1}. Therefore, using a 1-D radiative transfer code will lead to significantly overestimate the mass-loss rate of the synthetic, unresolved sources.

The discrepancy between the mass-loss rate derived fitting both the line profile and the velocity-integrated intensities measured along the different line of sights for the rotational transitions with $J_u \geq 6$ modelled appears to be even more critical. In particular, the J=15→14 transition exhibit large differences between both the line profile and integrated intensity measured along the minor and the major axis towards the more distant source. In contrast with the integrated intensity measured for the other rotational transitions, the larger difference between I_0 and I_{90} is measured for the lowest mass-loss rate source modelled. Because it traces the innermost regions of the CSEs modelled, the line profile and the integrated intensity of the J=15→14 transition is more sensitive to the oblateness of the source. In fact, for the source with $a = 0.9$ and $\dot{M}_{-7}$, the difference between the integrated intensities measured along the minor and major axis is ~ 20%. Therefore, it seems unlikely to obtain reliable mass-loss rates values from the observations towards the oblate synthetic sources fitting the spectral features and integrated intensities measured for the high J transitions assuming that the source is spherically symmetric.

7.4 Conclusions

We have modelled circumstellar emission using the 3-D radiative transfer code LIME for five CO rotational transitions: J=1→0, J=2→1, J=3→2, J=6→5, and J=15→14. The models have been calculated for sources whose mass-loss rates are $\dot{M} = 5 \times 10^{-7}, 10^{-6}, 10^{5}$ M$_\odot$ yr^{-1} assuming the CSEs as oblate spheroids with minor-to-major axis ratios of 0.5, 0.7, 0.9, and 1.0 which stands for the spherically symmetric case. Then, in order to simulate single-dish radio observations, we have convolved the synthetic brightness distribution with a 2-D gaussian kernel using the CASA task *imsmooth*. The observations have been simulated towards each single source along three different line of sights: Along the minor and major axis, as well as along an intermediate direction defined by $\theta = \pi/4$ (where θ is the polar angle measured from the z-axis). Both the line profile and the velocity-integrated intensity has been obtained from the simulated observations along each line of sight towards the synthetic sources located at 150 pc and 1 kpc. Our results suggest that in the case of spatially resolved emission, which is the case of rotational transitions with $J_u \leq 3$ observed towards the closest synthetic source, the difference on the line profile and the velocity-integrated intensity for the synthetic sources with $\dot{M} \leq 5 \times 10^{-6}$ M$_\odot$ yr^{-1} could lead to accurate estimates of their mass-loss rates assuming that the CSEs are spherically symmetric. On the other hand, the differences of the line profiles observed towards the most distant source along the different line of sights suggest that to estimate the mass-loss rate assuming that the emitting region is spherically symmetric could lead to reliable values only if the source has minor-to-major ratio $a \geq 0.9$. Fitting both the line profile and the integrated intensity measured for a particular rotational

transition for most oblate sources assuming them to be spherically symmetric leads to mass-loss estimates which, depending on the line of sight, can be larger than 20% the mass-loss rate of the observed synthetic source.
The results presented in this chapter are still preliminary, and will be complemented by using a 1-D Monte Carlo radiative transfer code in order to fit both the line profiles obtained from the simulated observations and the velocity-integrated intensity measured towards the synthetic sources. A similar analysis will be performed for the results of the modelled ^{13}CO emission. These results will be submitted for publication to the Astronomy and Astrophysics journal.

CHAPTER 8

Summary

In this thesis work, theory, observations, and computational models are combined aiming to study the emergence of asymmetries in the CSEs of AGB and post-AGB stars. This research has been focused on both the role played by large scale magnetic fields in the collimated bipolar outflows observed towards Water Fountains, and on the analysis of molecular line emission towards synthetic sources whose morphology resemble oblate ellipsoids.

One of the methods commonly used for the study of the magnetic field towards the CSEs of AGB and post-AGB stars is based on the detection of polarized maser emission. Since there are non-Zemman effects which can mimic or enhance the polarization state of the maser radiation, an analysis of the polarization properties of SiO, H_2O and HCN have been carried out. The aim of this study is to determine the maximum fractional linear polarization that can be detected in the ALMA frequency range which can be truly related to the presence of a magnetic field in the region where the maser emission is generated. We find that even for the high J transitions of SiO, H_2O and HCN, maser emission can be observed in the (sub)millimeter frequency range with suitable fractional linear polarization levels to trace the magnetic field morphology towards late-type stars even if the detected polarization has been affected by non-Zeeman effects.

In the observational context, this thesis includes the results of radio observations of both H_2O polarized maser emission and radio continuum emission. The observations were carried out using the Australia Telescope Compact Array (ATCA) towards two (out of 14 known up to date) water fountain sources. The results of these observations include the detection of fractional linear polarization of H_2O maser emission arising from the high-velocity outflows of the sources IRAS 15445−5449 and IRAS 18043−2116, whose polarization vector are tracing either the poloidal or toroidal component of the magnetic field along the bipolar outflows. Furthermore, we have resolved, for the first time towards a source of this kind, synchrotron emission which is consistent with the direction of the bipolar outflow observed at the infrared towards the source IRAS 15445−5449. The non-thermal emission is found tracing its collimated jet, implying that the toroidal component of the magnetic field collimates the bipolar outflow.

Finally, molecular ^{12}CO line emission from synthetic sources is modelled aiming to analyse the spectral features which could be detected towards CSEs of AGB stars whose morphologies resemble spheroids with different degrees of oblateness, mimicking the onset of collimated outflows. The 3-D radiative transfer code LIME is implemented in order to solve the equation of transfer throughout the oblate CSEs, along the major and minor axis, as well as along an intermediate direction. Then, the brightness distribution of CO obtained is convolved with a 2-D gaussian kernel aiming to simulate radio observations towards the synthetic sources using beam sizes of real radio telescope. We compare both the spectral line profiles and the velocity-integrated intensity obtained from the simulated observations towards the oblate CSEs with the spherically symmetric case. The simulated observations have been carried out for modelled sources with distances 150 pc and 1 kpc, this in order to analyse both, spatially resolved and unresolved emission. Our results suggest the uncertainties on the mass-loss rate estimated for sources with $\dot{M} < 10^{-6}$ M$_\odot$ yr^{-1} from fitting both the line profile and the velocity-integrated intensity of CO rotational transitions with $J_u \leq 3$ are unimportant even if the source is assumed to be spherically symmetric. On the other hand, when including in the analysis those CO transitions with $J_u \geq 6$ the effects of even slight asymmetries become relevant. Furthermore, we find that the differences of line profile and integrated intensity of transitions with $J_u \geq 6$ for the unresolved source are such that an accurate mass-loss estimate from those transitions seems unlikely.

8.1 Outlook

The study of the formation of the aspherical morphologies observed towards PN sources have gained great interest and relevance during the last decades. The results from my thesis a strong fundation for research that can be carried out in the near future.
The construction and functionality of cutting-edge telescopes as ALMA, the constant upgrading of the technology used on telescopes like JVLA and ATCA, and the improvement of both observation techniques and software for calibration and analysis of data, have been gradually increasing the range of accessible frequencies for the astronomy community, and in particular, for the study of AGB and post-AGB stars. Within the submillimeter wavelength range, a number of molecular transitions generating both thermal emission line and maser emission can be observed towards AGB, post-AGB and PNe sources. For instance, both interferometric and single-dish (sub-)millimeter observations of CO emission towards late-type stars are a powerful tool to constrain the distribution of the molecular gas content of the CSEs of this kind of sources. JVLA, ALMA, and APEX observations towards late-type stars could lead to detailed studies aimed to unveil the dynamics of the molecular gas component of the CSEs within different spatial scales. My thesis work naturally leads into for example the following research topics

- *Observation of radio continuum emission towards post-AGB sources: Water fountains.* We will continue our study of radio continuum emission towards bipolar post-AGB sources. This project will be part of a survey of radio and millimeter continuum emission using interferometric observations using JVLA and ATCA. Our detection of highly collimate synchrotron emission towards the post-AGB source IRAS 15445-5449 has raised the question about the kind of sources that could produce non-thermal continuum emission. Our first group of candidates to be tested will be the Water fountain sources. The outstanding sensitivity provided by the JVLA from band L up to band Q will allows to detect radio-continuum emission from the water fountain sources at the northern hemisphere, generating a data set which will be complemented with ATCA observations towards those sources at the southern sky. This will allow us to measure the spectral index of the spectral energy distribution covering the frequency range $[1, 40]$ GHz

- *Interferometric observations of CO emission towards bipolar and multipolar post-AGB stars.* The results of the models in this thesis are also a strong basis for ALMA observations of ^{12}CO (1-0), (2-1) and (3-2) rotational transitions towards bipolar and multipolar post-AGB stars. Imaging with the high spatial resolution that can be achieved by ALMA will allow us to trace the molecular gas content of the bipolar structures. If the axisymmetric structures observed are due to the action of high-velocity outflows, then the molecular gas emission can be used to infer the strength and momentum of the outflow at different regions along the axis that it defines, as well as the nature of the shocks involved during the formation of such bipolar or multipolar structures. Combining these with mid-infrared observations performed with VISIR, MIDI and AMBER, will allow us to correlate the molecular gas distribution with the dust distribution along the outflows, as well as to probe the outflow launching region at the near- and mid-IR. Furthermore, once ALMA starts working with full polarization capabilities, observations of polarized CO emission lines produced by the Goldreich-Kylafis effect will allow us to probe the influence of the stellar magnetic field on the collimation of the outflows.

- *Observation of submillimeter maser emission towards AGB stars.* We will create a large data set of submillimeter and millimeter observations of SiO, H_2O and HCN polarized maser emission towards late-type stars. The high spatial resolution that can be achieved with ALMA observations will allow us to study the polarization properties of a number of rotational transitions of SiO, H_2O and HCN within a frequency range which has been little explored. This data set will allow us to complement the theoretical study of the levels of fractional linear polarization that could be detected towards AGB stars, presented in Chapter 4. The results from the observations will lead us to settle a complete research work that could eventually be used in order to prepare ALMA observation programs including polarized maser emission.

Bibliography

Alcolea, J. and K. M. Menten (1993), "The excitation of vibrationally excited H2O masers", *Astrophysical Masers*, ed. by A. W. Clegg and G. E. Nedoluha, vol. 412, Lecture Notes in Physics, Berlin Springer Verlag 399–402, DOI: 10.1007/3-540-56343-1_288.

Alves, F. O. et al. (June 2012), "The magnetic field of IRAS 16293-2422 as traced by shock-induced H_2O masers", *A&A* 542, A14 A14, DOI: 10.1051/0004-6361/201118710, arXiv:1204.0004 [astro-ph.GA].

Amiri, N., W. Vlemmings and H. J. van Langevelde (Jan. 2010), "The magnetic field of the evolved star W43A", *A&A* 509, A26 A26, DOI: 10.1051/0004-6361/200913194, arXiv:0910.5421 [astro-ph.SR].

Amiri, N. et al. (Feb. 2012), "VLBA SiO maser observations of the OH/IR star OH 44.8-2.3: magnetic field and morphology", *A&A* 538, A136 A136, DOI: 10.1051/0004-6361/201117452, arXiv:1110.4071 [astro-ph.SR].

Bains, I. et al. (Aug. 2009), "Revealing the transition from post-AGB stars to planetary nebulae: non-thermal and thermal radio continuum observations", *MNRAS* 397 1386–1401, DOI: 10.1111/j.1365-2966.2009.14845.x.

Balick, B. and A. Frank (2002), "Shapes and Shaping of Planetary Nebulae", *ARA&A* 40 439–486, DOI: 10.1146/annurev.astro.40.060401.093849.

Barvainis, R. and C. R. Predmore (Jan. 1985), "A multitransitional study of linear polarization in SiO maser emission", *ApJ* 288 694–702, DOI: 10.1086/162835.

Beck, R. and M. Krause (July 2005), "Revised equipartition and minimum energy formula for magnetic field strength estimates from radio synchrotron observations", *Astronomische Nachrichten* 326 414–427, DOI: 10.1002/asna.200510366, eprint: astro-ph/0507367.

Bieging, J. H. (Mar. 2001), "Discovery of Two New HCN Maser Lines in Five Carbon Stars", *ApJ* 549 L125–L129, DOI: 10.1086/319130.

Blandford, R. D. and D. G. Payne (June 1982),
"Hydromagnetic flows from accretion discs and the production of radio jets", *MNRAS* 199 883–903.

Boboltz, D. A. and P. J. Diamond (June 2005),
"Axial Symmetry and Rotation in the SiO Maser Shell of IK Tauri", *ApJ* 625 978–984,
DOI: 10.1086/429656, eprint: astro-ph/0503182.

Boboltz, D. A. and K. B. Marvel (July 2005), "OH 12.8-0.9: A New Water-Fountain Source", *ApJ* 627 L45–L48, DOI: 10.1086/431931, eprint: astro-ph/0505629.

Brinch, C. and M. R. Hogerheijde (Nov. 2010), "LIME - a flexible, non-LTE line excitation and radiation transfer method for millimeter and far-infrared wavelengths", *A&A* 523, A25 A25,
DOI: 10.1051/0004-6361/201015333, arXiv:1008.1492 [astro-ph.SR].

Bujarrabal, V. et al. (Oct. 2001),
"Mass, linear momentum and kinetic energy of bipolar flows in protoplanetary nebulae",
A&A 377 868–897, DOI: 10.1051/0004-6361:20011090.

Burns, J. O., F. N. Owen and L. Rudnick (Nov. 1979),
"The wide-angle tailed radio galaxy 1159 + 583 - Observations and models", *AJ* 84 1683–1693,
DOI: 10.1086/112594.

Carrasco-González, C. et al. (Nov. 2010), "A Magnetized Jet from a Massive Protostar",
Science 330 1209–, DOI: 10.1126/science.1195589, arXiv:1011.6254 [astro-ph.GA].

Chapman, J. M. et al. (June 1999), "Radio Continuum Measurements of Southern Early-Type Stars. III. Nonthermal Emission from Wolf-Rayet Stars", *ApJ* 518 890–900, DOI: 10.1086/307314.

Cohen, M. et al. (June 2006),
"Radio observations of the planetary nebula around the OH/IR star OH354.88-0.54 (V1018 Sco)",
MNRAS 369 189–196, DOI: 10.1111/j.1365-2966.2006.10279.x, eprint: astro-ph/0603321.

Cohen, R. J. (Aug. 1989), "Compact maser sources", *Reports on Progress in Physics* 52 881–943,
DOI: 10.1088/0034-4885/52/8/001.

Deacon, R. M., J. M. Chapman and A. J. Green (Dec. 2004),
"OH Maser Observations of Likely Planetary Nebulae Precursors", *ApJS* 155 595–622,
DOI: 10.1086/425329, eprint: astro-ph/0406198.

Deacon, R. M. et al. (Apr. 2007), "H_2O Maser Observations of Candidate Post-AGB Stars and Discovery of Three High-Velocity Water Sources", *ApJ* 658 1096–1113, DOI: 10.1086/511383,
eprint: astro-ph/0702086.

Decin, L. et al. (Nov. 2007), "The variable mass loss of the AGB star <ASTROBJ>WX Piscium</ASTROBJ> as traced by the CO J = 1-0 through 7-6 lines and the dust emission",
A&A 475 233–242, DOI: 10.1051/0004-6361:20077737, arXiv:0708.4107.

Deguchi, S. and W. D. Watson (May 1990), "Linearly polarized radiation from astrophysical masers due to magnetic fields when the rate for stimulated emission exceeds the Zeeman frequency",
ApJ 354 649–659, DOI: 10.1086/168722.

Diamond, P. J. et al. (July 1994),
"Observation of a ring structure in SiO maser emission from late-type stars", *ApJ* 430 L61–L64,
DOI: 10.1086/187438.

Dinh-v-Trung (Nov. 2009),
"On the theory of astronomical masers - II. Polarization of maser radiation",
MNRAS 399 1495–1505, DOI: 10.1111/j.1365-2966.2009.15369.x,
arXiv:0907.1327 [astro-ph.GA].

Dorschner, J. et al. (Aug. 1995), "Steps toward interstellar silicate mineralogy. II. Study of Mg-Fe-silicate glasses of variable composition.", *A&A* 300 503.

Dullemond, C. P. (Feb. 2012), *RADMC-3D: A multi-purpose radiative transfer tool*, Astrophysics Source Code Library, ascl: 1202.015.

Elitzur, M., ed. (1992), *Astronomical masers*, vol. 170, Astrophysics and Space Science Library.

Fish, V. L. and M. J. Reid (Feb. 2007a), "Large Magnetic Fields and Motions of OH Masers in W75N", *ApJ* 656 952–958, DOI: 10.1086/510578, eprint: arXiv:astro-ph/0611097.

– (Dec. 2007b),
"Proper Motions of OH Masers and Magnetic Fields in Massive Star-forming Regions",
ApJ 670 1159–1172, DOI: 10.1086/522329, arXiv:0708.1186.

García-Segura, G. et al. (June 1999), "Shaping Bipolar and Elliptical Planetary Nebulae: Effects of Stellar Rotation, Photoionization Heating, and Magnetic Fields", *ApJ* 517 767–781,
DOI: 10.1086/307205.

Goldreich, P., D. A. Keeley and J. Y. Kwan (Jan. 1973),
"Astrophysical Masers. 11. Polarization Properties", *ApJ* 179 111–134, DOI: 10.1086/151852.

Goldreich, P. and J. Kwan (May 1974), "Astrophysical Masers.IV. Line Widths", *ApJ* 190 27–34,
DOI: 10.1086/152843.

Goldsmith, P. F. et al. (Oct. 1988), "Linear polarization of HCN maser emission in CIT 6",
ApJ 333 873–879, DOI: 10.1086/166796.

Gómez, J. F. et al. (Sept. 2011), "IRAS 18113-2503: The Water Fountain with the Fastest Jet?",
ApJ 739, L14 L14, DOI: 10.1088/2041-8205/739/1/L14, arXiv:1105.5202 [astro-ph.SR].

Gray, M. (Apr. 2012), *Maser Sources in Astrophysics*.

Habing, H. J. and H. Olofsson, eds. (2003), *Asymptotic giant branch stars*.

Harwit, M. et al. (Oct. 2010), "Polarisation observations of VY Canis Majoris H_2O 5_{32}-4_{41} 620.701 GHz maser emission with HIFI", *A&A* 521, L51 L51, DOI: 10.1051/0004-6361/201015042,
arXiv:1007.0905 [astro-ph.SR].

Herpin, F. et al. (May 2006), "Full polarization study of SiO masers at 86 GHz", *A&A* 450 667–680,
DOI: 10.1051/0004-6361:20054255, eprint: arXiv:astro-ph/0601098.

Herwig, F. (Sept. 2005), "Evolution of Asymptotic Giant Branch Stars", *ARA&A* 43 435–479,
DOI: 10.1146/annurev.astro.43.072103.150600.

Hony, S., L. B. F. M. Waters and A. G. G. M. Tielens (Aug. 2002), "The carrier of the "30" mu m emission feature in evolved stars. A simple model using magnesium sulfide", *A&A* 390 533–553, DOI: 10.1051/0004-6361:20020603, eprint: astro-ph/0204330.

Huarte-Espinosa, M. et al. (Sept. 2012), "On the Structure and Stability of Magnetic Tower Jets", *ApJ* 757, 66 66, DOI: 10.1088/0004-637X/757/1/66, arXiv:1204.0800 [astro-ph.SR].

Humphreys, E. M. L. (Mar. 2007), "Submillimeter and millimeter masers", *IAU Symposium*, ed. by J. M. Chapman and W. A. Baan, vol. 242, IAU Symposium 471–480, DOI: 10.1017/S1743921307013622, arXiv:0705.4456.

Ivison, R. J., J. A. Yates and P. J. Hall (Apr. 1998), "The simultaneous detection of 22- and 321-GHz H_2O maser emission towards the symbiotic Mira R Aquarii", *MNRAS* 295 813–818, DOI: 10.1046/j.1365-8711.1998.01237.x, eprint: arXiv:astro-ph/9709281.

Jaeger, C. et al. (Dec. 1994), "Steps toward interstellar silicate mineralogy. 1: Laboratory results of a silicate glass of mean cosmic composition", *A&A* 292 641–655.

Jura, M. (Dec. 1983), "Mass loss rates and anisotropies in the outflows from late-type stars", *ApJ* 275 683–690, DOI: 10.1086/161565.

Kemball, A. J. and P. J. Diamond (June 1997), "Imaging the Magnetic Field in the Atmosphere of TX Cam", *ApJ* 481 L111, DOI: 10.1086/310664.

Kemball, A. J. et al. (June 2009), "Multi-Epoch Imaging Polarimetry of the SiO Masers in the Extended Atmosphere of the Mira Variable TX Cam", *ApJ* 698 1721–1739, DOI: 10.1088/0004-637X/698/2/1721, arXiv:0904.2621 [astro-ph.SR].

Koning, N., S. Kwok and W. Steffen (Mar. 2013), "Post Asymptotic Giant Branch Bipolar Reflection Nebulae: Result of Dynamical Ejection or Selective Illumination?", *ApJ* 765, 92 92, DOI: 10.1088/0004-637X/765/2/92.

Kukolich, S. G. (May 1969), "Measurement of the Molecular g Values in H_2O and D_2O and Hyperfine Structure in H_2O", *J. Chem. Phys* 50 3751–3755, DOI: 10.1063/1.1671623.

Lagadec, E. et al. (Oct. 2011), "A mid-infrared imaging catalogue of post-asymptotic giant branch stars", *MNRAS* 417 32–92, DOI: 10.1111/j.1365-2966.2011.18557.x, arXiv:1102.4561 [astro-ph.SR].

Lamers, H. J. G. L. M. and J. P. Cassinelli (June 1999), *Introduction to Stellar Winds*.

Landolt-Börnstein (1982), "Numerical Data and Functional Relationships in Science and Technology", Group II, 14a, ed. K.-H. Hellwege and A.M. Hellwege (Berlin:Springer) p750.

Leal-Ferreira, M. L. et al. (Apr. 2012), "Rotten Egg nebula: the magnetic field of a binary evolved star", *A&A* 540, A42 A42, DOI: 10.1051/0004-6361/201118303, arXiv:1201.3839 [astro-ph.SR].

Likkel, L. and M. Morris (June 1988),
"The circumstellar water fountains of IRAS 16342-3814 - A very high velocity bipolar outflow",
ApJ 329 914–919, DOI: `10.1086/166435`.

Lockett, P., E. Gauthier and M. Elitzur (Jan. 1999),
"OH 1720 Megahertz Masers in Supernova Remnants: C-Shock Indicators", *ApJ* 511 235–241,
DOI: `10.1086/306667`, eprint: `astro-ph/9809019`.

Lorenz-Martins, S. and J. Lefevre (Nov. 1994), "SiC grains and evolution of carbon stars",
A&A 291 831–841.

Lucas, R. and J. Cernicharo (July 1989),
"Discovery of strong maser emission from HCN in IRC+10216", *A&A* 218 L20–L22.

Maercker, M. et al. (Mar. 2008), "Circumstellar water vapour in M-type AGB stars: radiative transfer models, abundances, and predictions for HIFI", *A&A* 479 779–791,
DOI: `10.1051/0004-6361:20078680`, arXiv:`0801.0971`.

Maercker, M. et al. (Oct. 2012),
"Unexpectedly large mass loss during the thermal pulse cycle of the red giant star R Sculptoris",
NATURE 490 232–234, DOI: `10.1038/nature11511`, arXiv:`1210.3030 [astro-ph.SR]`.

Melnick, G. J. et al. (Oct. 1993), "Discovery of Interstellar Water Lines at 437, 439, and 471 GHz: Strong Case for Water Maser Formation behind C-Type Shocks", *ApJ* 416 L37,
DOI: `10.1086/187065`.

Menten, K. M., G. J. Melnick and T. G. Phillips (Feb. 1990), "Submillimeter water masers",
ApJ 350 L41–L44, DOI: `10.1086/185663`.

Menten, K. M. et al. (Nov. 1990), "A new submillimeter water maser transition at 325 GHz",
ApJ 363 L27–L31, DOI: `10.1086/185857`.

Menten, K. M. et al. (Aug. 2006), "Submillimeter vibrationally excited water emission from the peculiar red supergiant VY Canis Majoris", *A&A* 454 L107–L110,
DOI: `10.1051/0004-6361:20065458`, eprint: `arXiv:astro-ph/0606057`.

Müller, H. S. P. et al. (Apr. 2001), "The Cologne Database for Molecular Spectroscopy, CDMS",
A&A 370 L49–L52, DOI: `10.1051/0004-6361:20010367`.

Murphy, T. et al. (Nov. 2007),
"The second epoch Molonglo Galactic Plane Survey: compact source catalogue",
MNRAS 382 382–392, DOI: `10.1111/j.1365-2966.2007.12379.x`, arXiv:`0708.3092`.

Nedoluha, G. E. and W. D. Watson (May 1990a), "Linearly polarized radiation from astrophysical masers due to magnetic fields of intermediate strength", *ApJ* 354 660–675, DOI: `10.1086/168723`.

– (Oct. 1990b), "Modifications to the relationship between the magnetic field and weak Zeeman features in the spectra of astrophysical masers", *ApJ* 361 L53–L55, DOI: `10.1086/185825`.

– (Feb. 1991), "Spectral line profiles and luminosities of astrophysical water masers",
ApJ 367 L63–L67, DOI: `10.1086/185932`.

Nedoluha, G. E. and W. D. Watson (Jan. 1992), "The Zeeman effect in astrophysical water masers and the observation of strong magnetic fields in regions of star formation", *ApJ* 384 185–196, DOI: 10.1086/170862.

Neufeld, D. A. and G. J. Melnick (Feb. 1991), "Excitation of millimeter and submillimeter water masers", *ApJ* 368 215–230, DOI: 10.1086/169685.

Olofsson, H. et al. (July 1993), "A study of circumstellar envelopes around bright carbon stars. I - Structure, kinematics, and mass-loss rate.", *ApJS* 87 267–304, DOI: 10.1086/191804.

Pacholczyk, A. G. (1970), *Radio astrophysics. Nonthermal processes in galactic and extragalactic sources.*

Pérez-Sánchez, A. F. and W. H. T. Vlemmings (Mar. 2013), "Linear polarization of submillimetre masers. Tracing magnetic fields with ALMA", *A&A* 551, A15 A15, DOI: 10.1051/0004-6361/201220735, arXiv:1301.0813 [astro-ph.SR].

Pérez-Sánchez, A. F., W. H. T. Vlemmings and J. M. Chapman (Dec. 2011), "Water maser polarization of the water fountains IRAS 15445-5449 and IRAS 18043-2116", *MNRAS* 418 1402–1407, DOI: 10.1111/j.1365-2966.2011.19593.x, arXiv:1108.1911 [astro-ph.SR].

Pérez-Sánchez, A. F. et al. (Nov. 2013), "A synchrotron jet from a post-asymptotic giant branch star", *MNRAS* 436 L79–L83, DOI: 10.1093/mnrasl/slt117, arXiv:1308.5970 [astro-ph.SR].

Ramstedt, S. et al. (Aug. 2008), "On the reliability of mass-loss-rate estimates for AGB stars", *A&A* 487 645–657, DOI: 10.1051/0004-6361:20078876, arXiv:0806.0517.

Richards, A. M. S., M. Elitzur and J. A. Yates (Jan. 2011), "Observational evidence for the shrinking of bright maser spots", *A&A* 525, A56 A56, DOI: 10.1051/0004-6361/201015397, arXiv:1010.4419 [astro-ph.GA].

Sabin, L., A. A. Zijlstra and J. S. Greaves (Mar. 2007), "Magnetic fields in planetary nebulae and post-AGB nebulae", *MNRAS* 376 378–386, DOI: 10.1111/j.1365-2966.2007.11445.x, eprint: astro-ph/0701054.

Sahai, R., M. R. Morris and G. G. Villar (Apr. 2011), "Young Planetary Nebulae: Hubble Space Telescope Imaging and a New Morphological Classification System", *AJ* 141, 134 134, DOI: 10.1088/0004-6256/141/4/134, arXiv:1101.2214 [astro-ph.GA].

Sahai, R. et al. (Dec. 2007), "Preplanetary Nebulae: A Hubble Space Telescope Imaging Survey and a New Morphological Classification System", *AJ* 134 2200–2225, DOI: 10.1086/522944, arXiv:0707.4662.

Sandage, A. and M. F. Walker (Feb. 1966), "Three-color photometry of the bright stars in the globular cluster M92", *ApJ* 143 313, DOI: 10.1086/148514.

Sault, R. J., P. J. Teuben and M. C. H. Wright (1995), "A Retrospective View of MIRIAD", *Astronomical Data Analysis Software and Systems IV*,

ed. by R. A. Shaw, H. E. Payne and J. J. E. Hayes, vol. 77,
Astronomical Society of the Pacific Conference Series 433, eprint: astro-ph/0612759.

Schilke, P., D. M. Mehringer and K. M. Menten (Jan. 2000),
"A Submillimeter HCN Laser in IRC +10216", *ApJ* 528 L37–L40, DOI: 10.1086/312416.

Schilke, P. and K. M. Menten (Jan. 2003),
"Detection of a Second, Strong Submillimeter HCN Laser Line toward Carbon Stars",
ApJ 583 446–450, DOI: 10.1086/345099.

Schöier, F. L. and H. Olofsson (Mar. 2001), "Models of circumstellar molecular radio line emission. Mass loss rates for a sample of bright carbon stars", *A&A* 368 969–993,
DOI: 10.1051/0004-6361:20010072, eprint: astro-ph/0101477.

Sevenster, M. N. (May 2002),
"OH-selected AGB and Post-AGB Objects. I. Infrared and Maser Properties", *AJ* 123 2772–2787,
DOI: 10.1086/339827, eprint: astro-ph/0202182.

Sevenster, M. N. and J. M. Chapman (Jan. 2001),
"A Shock-excited OH Maser in a Post-Asymptotic Giant Branch Envelope?", *ApJ* 546 L119–L122,
DOI: 10.1086/318867, eprint: astro-ph/0011114.

Sevenster, M. N. et al. (Apr. 1997a),
"The ATCA/VLA OH 1612 MHz survey. I. Observations of the galactic bulge Region",
A&AS 122 79–93, DOI: 10.1051/aas:1997294.

– (Sept. 1997b),
"The ATCA/VLA OH 1612 MHz survey. II. Observations of the galactic Disk region",
A&AS 124 509–515, DOI: 10.1051/aas:1997365.

Shinnaga, H. et al. (Nov. 2004), "Interferometric Observation of the Highly Polarized SiO Maser Emission from the v = 1, J = 5-4 Transition Associated with VY Canis Majoris", *ApJ* 616 L47–L50,
DOI: 10.1086/425133, eprint: arXiv:astro-ph/0408298.

Shu, F. et al. (July 1994),
"Magnetocentrifugally driven flows from young stars and disks. 1: A generalized model",
ApJ 429 781–796, DOI: 10.1086/174363.

Surcis, G. et al. (Sept. 2011a),
"The properties and polarization of the H_2O and CH_3OH maser environment of NGC 7538-IRS 1",
A&A 533, A47 A47, DOI: 10.1051/0004-6361/201117108, arXiv:1107.5313 [astro-ph.SR].

Surcis, G. et al. (Mar. 2011b),
"The structure of the magnetic field in the massive star-forming region W75N", *A&A* 527, A48 A48,
DOI: 10.1051/0004-6361/201015825, arXiv:1101.1956 [astro-ph.SR].

Thompson, A. R., J. M. Moran and G. W. Swenson Jr. (2001),
Interferometry and Synthesis in Radio Astronomy, 2nd Edition.

Urquhart, J. S. et al. (Nov. 2007a),
"The RMS survey. ^{13}CO observations of candidate massive YSOs in the southern Galactic plane", *A&A* 474 891–901, DOI: 10.1051/0004-6361:20078025.

Urquhart, J. S. et al. (Jan. 2007b),
"The RMS survey. Radio observations of candidate massive YSOs in the southern hemisphere", *A&A* 461 11–23, DOI: 10.1051/0004-6361:20065837, eprint: astro-ph/0605738.

Vlemmings, W. H. T., P. J. Diamond and H. Imai (Mar. 2006),
"A magnetically collimated jet from an evolved star", *NATURE* 440 58–60, DOI: 10.1038/nature04466, eprint: astro-ph/0603003.

Vlemmings, W. H. T., E. M. L. Humphreys and R. Franco-Hernández (Feb. 2011),
"Magnetic Fields in Evolved Stars: Imaging the Polarized Emission of High-frequency SiO Masers", *ApJ* 728, 149 149, DOI: 10.1088/0004-637X/728/2/149, arXiv:1101.1960 [astro-ph.SR].

Vlemmings, W. H. T. and H. J. van Langevelde (May 2005),
"Astrophysical water masers: Line profiles analysis", *A&A* 434 1021–1028, DOI: 10.1051/0004-6361:20042430, eprint: arXiv:astro-ph/0501627.

Vlemmings, W. H. T., H. J. van Langevelde and P. J. Diamond (May 2005),
"The magnetic field around late-type stars revealed by the circumstellar H_2O masers", *A&A* 434 1029–1038, DOI: 10.1051/0004-6361:20042488, eprint: arXiv:astro-ph/0501628.

Vlemmings, W. H. T. et al. (Mar. 2006), "The magnetic field in the star-forming region Cepheus A. from H_2O maser polarization observations", *A&A* 448 597–611, DOI: 10.1051/0004-6361:20054275, eprint: arXiv:astro-ph/0510452.

Vlemmings, W. (2002), "Circumstellar maser properties through VLBI observations", PhD thesis, , Leiden University, November 2002.

Wagenhuber, J. and M. A. T. Groenewegen (Dec. 1998),
"New input data for synthetic AGB evolution", *A&A* 340 183–195, eprint: astro-ph/9809338.

Walsh, A. J. et al. (Mar. 2009),
"High-velocity H^2O maser emission from the post-asymptotic-giant-branch star OH 009.1-0.4", *MNRAS* 394 L70–L73, DOI: 10.1111/j.1745-3933.2008.00613.x.

Waters, J. W. et al. (Jan. 1980), "Observations of interstellar H2O emission at 183 gigahertz", *ApJ* 235 57–62, DOI: 10.1086/157609.

Watson, W. D. (2002), "Theory and extragalactic masers",
Cosmic Masers: From Proto-Stars to Black Holes, ed. by V. Migenes and M. J. Reid, vol. 206, IAU Symposium 464, eprint: arXiv:astro-ph/0107572.

Watson, W. (Mar. 2008), "Masers as a probe of magnetic fields in dense regions: theory", *Cosmic Agitator: Magnetic Fields in the Galaxy*.

Western, L. R. and W. D. Watson (Oct. 1984),
"Linear polarization of astronomical masers and magnetic fields", *ApJ* 285 158–173, DOI: 10.1086/162487.

Wiebe, D. S. and W. D. Watson (Aug. 1998), "A Non-Zeeman Interpretation for Polarized Maser Radiation and the Magnetic Field at the Atmospheres of Late-Type Giants", *ApJ* 503 L71, DOI: 10.1086/311526, eprint: arXiv:astro-ph/9806155.

Yates, J. A. and R. J. Cohen (Jan. 1996), "Submillimetre water masers in circumstellar envelopes - II. Variability", *MNRAS* 278 655–668.

van Kempen, T. A., D. Wilner and M. Gurwell (Nov. 2009), "183 GHz H_2O Maser Emission Around the Low-Mass Protostar Serpens SMM1", *ApJ* 706 L22–L26, DOI: 10.1088/0004-637X/706/1/L22, arXiv:0910.0831 [astro-ph.SR].

van Winckel, H. (2003), "Post-AGB Stars", *ARA&A* 41 391–427, DOI: 10.1146/annurev.astro.41.071601.170018.

List of Figures

1.1 HR Diagram 2
1.2 Nucleosynthesis sketch 4
1.3 CO ratio 6
1.4 IR AGB stars 8
1.5 Scheme: Maser spectra 11
1.6 Planetary nebulae: Shapes 14

3.1 Atmospheric opacity 30
3.2 Beam pattern 31
3.3 Interferometers 34

4.1 SiO Fractional linear polarization 49
4.2 H_2O Fractional linear polarization 50
4.3 HCN Fractional linear polarization 51

5.1 Water maser spectra 59
5.2 Maser regions 61
5.3 Spatial distribution of maser emission 62
5.4 IRAS 154450−5449 66

6.1 Spectral energy distribution 75
6.2 22 GHz radio continuum map. 77
6.3 Radio continuum overlaid on mid-IR map 78

7.1 CO modelling: Density distribution. 84
7.2 Brightness distribution $\dot{M} = 5 \times 10^{-5}$ $M_\odot$ yr^{-1} 86
7.3 Brightness distribution $\dot{M} = 5 \times 10^{-6}$ $M_\odot$ yr^{-1} 87
7.4 Features: Spherical case 89
7.5 Features $a = 0.9$ case 91
7.6 Features $a = 0.7$ case 93

7.7 Features $a = 0.5$ case 95
7.8 Integrated Intensities 98

List of Tables

4.1 SiO maser transitions in the ALMA frequency range 45
4.2 H_2O and HCN maser transitions at submillimetre wavelengths. 46
4.3 Model parameters 46
4.4 Model Results 48
4.5 Sensitivity values for SiO, H_2O and HCN within the ALMA frequency range. 52

5.1 Maser features. 60

6.1 Flux density of IRAS 15445−5449. 72

7.1 CO modelling: Parameters. 85
7.2 CO modelling: Beam sizes. 85

Acknowledgements

I would like to thank my supervisor Prof. Dr. Wouter Vlemmings for giving me the great opportunity of working in such an outstanding environment, and for helping me to get to this point of my career. Thanks for your trust, your patience, and all your support during this time. I am glad to have had the great opportunity of working under your supervision, and of being part of your working group. I am really glad and proud because in the future I can say: Yes, Wouter was my Ph.D supervisor.

Many thanks to all the group members, in particular, I would like to express all my gratitude to Dr. Sofia Ramstedt for all the support, the encouragement and the honesty of your comments and advices, and also for including me on your science projects since the beginning, specially in those which implied going to great telescopes in order to perform observations. Thanks to you and Wouter my dreams of visiting and actually performing observations with great telescopes came true.

I also would like to thank Dr. Matthias Maercker and Dr. Elvire De Beck for the nice science discussions, in particular during these last months. Thanks Matthias for being so supportive all the time. I cannot thank enough my office-mate Franz Kirsten. Thanks for your absolute friendship and unconditional help, you were always there to offer me a hand. Thanks a lot, dude. Furthermore, I would like to thank Mrs. Christina Stein for all the help and support provided since my arrival in the institute.

I will be always grateful with my family in Colombia for all the support and understanding. It has been tough being far away from you all. A mi tia infinitas gracias por enseñarme lo que es ser valiente y luchar siempre, si no fuera por ti no sé que sería de mi, gracias por siempre apoyarme en todo. I would like to thank Laura for being the best tandem of pasarla bien ever, you make special every day. Grazie preciosa, Grazie mille for your constant support and encouragement, Gone, you are the best!

Finally, I would like to thank all the friends that I met during my time in Germany, thanks for everything Andrés Balaguera, Pilar, Celeste, Juanito, Jackie, Charly, Ali, Maria del Mar, Ana Maria, Rebe, Miriam, Ancor, Caro, Luis, Lore, Monica, Norbert, Gio, Emilio… and many others with whom I had a great time. Thank you all!

Bonn, 20 March, 2014